Decay Modes of Exotic Nuclei

Hrabar, Yuliia

2024

Decay Modes of Exotic Nuclei

YULIIA HRABAR
DEPARTMENT OF PHYSICS | FACULTY OF SCIENCE | LUND UNIVERSITY

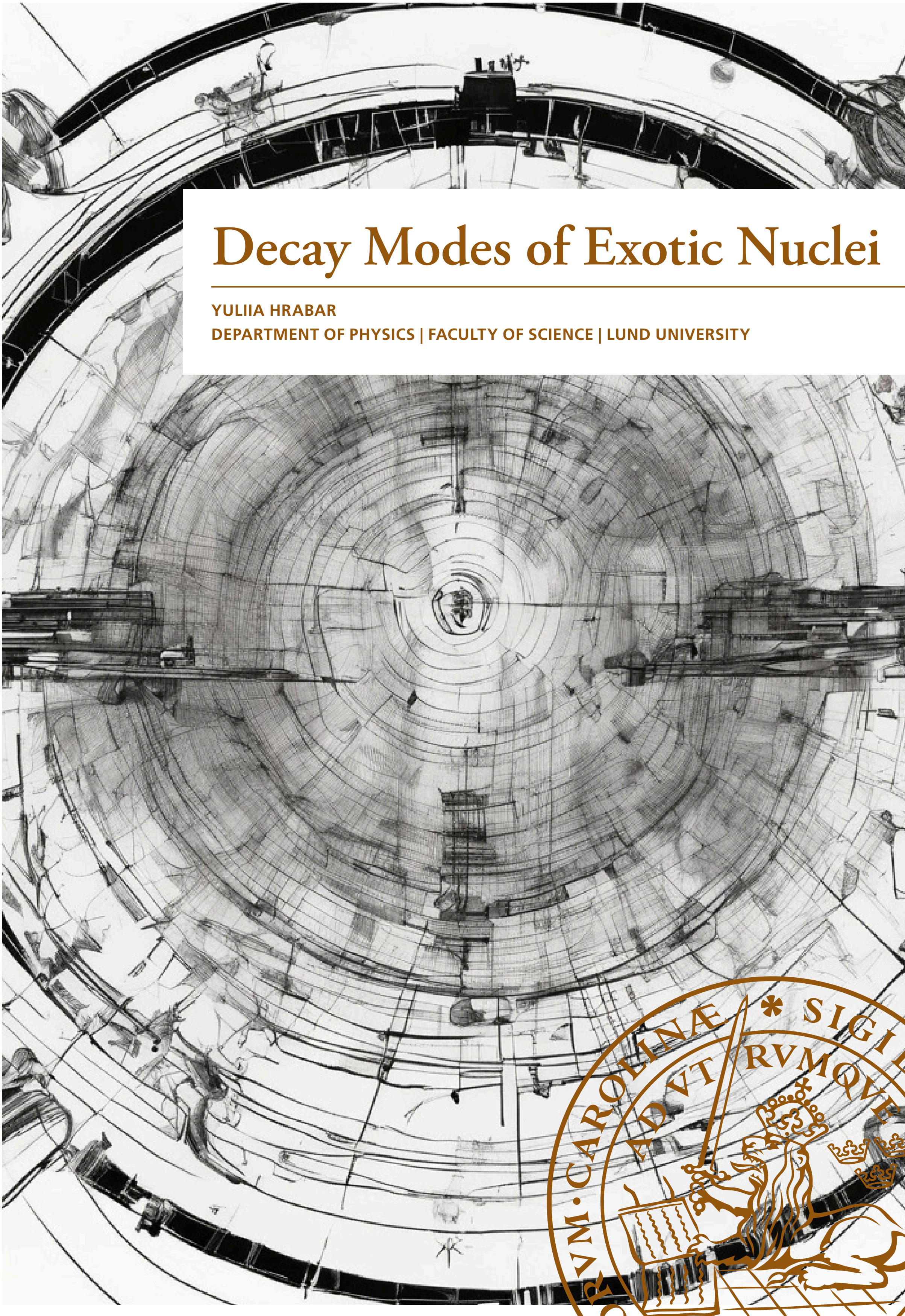

Decay Modes of Exotic Nuclei

Decay Modes of Exotic Nuclei

by Yuliia Hrabar

Thesis for the degree of Doctor of Philosophy
Thesis advisors: Dr. Pavel Golubev, Dr. Luis Sarmiento Pico
Faculty opponent: Dr. Augusto O. Macchiavelli

To be presented, with the permission of the Faculty of Science of Lund University, for public criticism in the Rydberg lecture hall at the Department of Physics on Friday, the 29th of November 2024 at 13:00.

DOKUMENTDATABLAD enl SIS 61 41 21

Organization	Document name
LUND UNIVERSITY	**DOCTORAL DISSERTATION**
Department of Physics Box 118 SE–221 00 LUND Sweden	Date of disputation 2024-11-29
	Sponsoring organization
Author(s) Yuliia Hrabar	

Title and subtitle

Decay Modes of Exotic Nuclei:

Abstract

This thesis presents advancements in studying exotic nuclei and rare decay modes through particle and γ-ray coincidence spectroscopy. The focus is on two experimental setups. First, complementing Compex Ge-detector modules with anti-Compton shields. Second, enhancing the Gammasphere-Microball setup at Argonne National Laboratory (ANL) with pixelated silicon detectors. These upgrades enable deeper insights into the structure and behavior of exotic nuclear systems through improved detection and analysis of rare decay events.

A bismuth-germanate (BGO) anti-Compton shield (ACS) for five Compex germanium detector modules was designed, built, and tested with two designs implemented to fit various Compex configurations. The ACS increased the peak-to-total performance by 70% for the ^{137}Cs 662-keV peak. These Compex detectors, equipped with ACS, are planned for diverse applications, including local environmental sample measurements, future nuclear structure studies at the GSI Helmholtz Centre for Heavy Ion Research, Germany, and the superheavy element research programme at Lawrence Berkeley National Laboratory, USA.

An experimental campaign at ANL in 2020 focused on odd-Z, neutron-deficient nuclei near ^{56}Ni. Two highly pixelated double-sided Si-strip detectors were added to the Gammasphere-Microball setup, improving in-beam proton-γ coincidence spectroscopy and enabling in-beam particle tracking for beam-spot position determination. Excited states in ^{61}Ga were populated via the fusion-evaporation reaction ^{24}Mg(^{40}Ca$, p2n)^{61}$Ga, leading to the identification of a proton-emitting state at $E_x = 2150(34)$ keV, interpreted as the $\pi g_{9/2}$ single-particle state. This discovery refined shell-model calculations through studying isospin-breaking parameters for the $A = 61$, $T_z = \pm 1/2$ mirror nuclei ^{61}Ga and ^{61}Zn.

In the same experiment, deuteron evaporation from ^{52}Fe*, ^{56}Ni*, and ^{64}Ge* was observed, based on enhanced light-charged particle sensitivity. A study was conducted for a few evaporation channels comparing relative production rates for deuteron vs. proton-neutron evaporation as a function of angular momentum and excitation energy.

Key words

Nuclear structure, scintillators, silicon detectors, γ-ray spectroscopy, particle spectroscopy, mirror nuclei, isospin symmetry, deuteron evaporation

Classification system and/or index terms (if any)

Subatomic physics

Supplementary bibliographical information		Language English
ISSN and key title		ISBN 978-91-8104-223-8 (print) 978-91-8104-224-5 (pdf)
Recipient's notes	Number of pages 158	Price
	Security classification	

Signature ________________________ Date 2024-10-14

Decay Modes of Exotic Nuclei

by Yuliia Hrabar

A doctoral thesis at a university in Sweden takes either the form of a single, cohesive research study (monograph) or a summary of research papers (compilation thesis), which the doctoral student has written alone or together with one or several other author(s).

In the latter case the thesis consists of two parts. An introductory text puts the research work into context and summarizes the main points of the papers. Then, the research publications themselves are reproduced, together with a description of the individual contributions of the authors. The research papers may either have been already published or are manuscripts at various stages (in press, submitted, or in draft).

Cover illustration front: An abstract image of a DSSD detector inside of a target chamber. The figure was generated with the assistance of OpenArt.

Cover illustration back: Photo courtesy Ilinca Porojan-Gheaja.

Funding information: The thesis work was financially supported in part by the Swedish Research Council (Vetenskapsrådet VR 2022-3828), the Crafoord Foundation in Lund (Grant 20180630), the Knut and Alice Wallenberg Foundation (KAW 2015.0021), the Royal Physiographic Society in Lund, and the Department of Physics at Lund University.

Faculty of Science, Department of Physics

ISBN: 978-91-8104-223-8 (print)
ISBN: 978-91-8104-224-5 (pdf)

Printed in Sweden by Media-Tryck, Lund University, Lund 2024

Media-Tryck is a Nordic Swan Ecolabel certified provider of printed material. Read more about our environmental work at www.mediatryck.lu.se

NORDIC SWAN ECOLABEL
Printed matter 3041 0903

MADE IN SWEDEN

Dedicated to my mom

Contents

List of Figures

List of Tables

Acronyms

ACS Anti-Compton shield

ADC Analog-to-digital converter

ANL Argonne National Laboratory

ATLAS Argonne Tandem Linac Accelerator System

BGO Bismuth germanate

DAQ Data acquisition system

DFMA Digital Fragment Mass Analyzer

DGS Digital Gammasphere

DSSD Double-sided Si-strip detector

FMA Fragment Mass Analyzer

HF Hartree Fock

HFB Hartree Fock Bogoliubov

HV High voltage

IC Ionization Chamber

LMD List-mode data

MBS Multi-Branch System

MCA Multichannel analyzer

MED Mirror energy differences

P/T Peak-to-total ratio

PCB Printed circuit board

PLA Poly-lactic acid

PMT Photomultiplier tube

PPAC Parallel Plate Avalanche Counter

R&D Research and development

SPE Single particle energy

TBME Two-body matrix element

TDC Time-to-digital converter

WuDAQ Washington University DAQ

Author's contributions

Contributions are listed according to the CRediT (Contributor Roles Taxonomy) statement.

Publications included in this thesis

Paper I

Anti-Compton shield for Compex germanium detector modules

Y. Hrabar, L.G. Sarmiento, P. Golubev, O. Bobovnikov, D.M. Cox, and D. Rudolph

Nucl. Instr. Meth. A **1056**, 16868 (2023)
DOI: 10.1016/j.nima.2023.168682

Y. Hrabar: Conceptualization (equal), Formal Analysis (lead), Funding Acquisition (supporting), Investigation (lead), Project administration (lead), Software (lead), Validation (lead), Visualization (lead), Writing - original draft (lead), Writing - review & editing (lead).

Paper II

Search for weak side branches in the electromagnetic decay of the 6526-keV 10^{+} isomer in ^{54}Fe

P. Böhm, **Y. Hrabar**, D. Rudolph, P. Golubev, L.G. Sarmiento, H.M. Albers, J.T. Anderson, M.A. Bentley, M.P. Carpenter, C.J. Chiara, P.A. Copp, U. Forsberg, T. Huang, H. Jayatissa, T. Lauritsen, C. Müller-Gatermann, X. Pereira-Lopez, W. Reviol, D. Seweryniak, S. Stolze, S. Uthayakumaar, G.L. Wilson, and J. Wu

Atoms **11**, 116 (2023)
DOI: 10.3390/atoms11090116

Y. Hrabar: Formal Analysis (supporting), Investigation (lead), Software (lead), Supervision (supporting), Validation (supporting), Writing - review & editing (supporting)

Paper III

Novel tools for in-beam proton-gamma coincidence spectroscopy near $N = Z$

Y. Hrabar, P. Golubev, D. Rudolph, L.G. Sarmiento, C. Müller-Gatermann, W. Reviol, D. Seweryniak, J. Wu, H.M. Albers, J.T. Anderson, M.A. Bentley, M.P. Carpenter, C.J. Chiara, P.A. Copp, D.M. Cox, C. Fahlander, U. Forsberg, T. Huang, H. Jayatissa, T. Lauritsen, X. Pereira-Lopez, S. Stolze, S. Uthayakumaar, and G.L. Wilson

Submitted to Acta Phys. Pol. B

Y. Hrabar: Conceptualization (equal), Formal Analysis (lead), Investigation (lead), Project administration (lead), Software (lead), Validation (lead), Visualization (lead), Writing - original draft (lead), Writing - review & editing (lead).

Paper IV

Identification of prompt-proton emission in $N = Z$–1 ^{61}Ga: isospin symmetry at the limit of nuclear binding

Y. Hrabar, P. Golubev, D. Rudolph, L. G. Sarmiento, C. Müller-Gatermann, W. Reviol, D. Seweryniak, J. Wu, H.M. Albers, J.T. Anderson, M.A. Bentley, B.G. Carlsson, M.P. Carpenter, C.J. Chiara, P.A. Copp, D.M. Cox, J. Ekman, C. Fahlander, U. Forsberg, T. Huang, A. Idini, H. Jayatissa, T. Lauritsen, X. Pereira-Lopez, S. Stolze, S. Uthayakumaar, and G.L. Wilson

Submitted to Phys. Rev. Lett.

Y. Hrabar: Conceptualization (equal), Formal Analysis (lead), Investigation (lead), Project administration (lead), Software (lead), Validation (lead), Visualization (lead), Writing - original draft (lead), Writing - review & editing (lead).

Paper V

Deuteron Evaporation from $N = Z$ Compound Nuclei

Y. Hrabar, P. Golubev, A. Idini, L.G. Sarmiento, B.G Carlsson, C. Müller-Gatermann, W. Reviol, D. Rudolph, D. Seweryniak, J. Wu, H.M. Albers, J.T. Anderson, M.A. Bentley, M.P. Carpenter, C.J. Chiara, P.A. Copp, D.M. Cox, C. Fahlander, U. Forsberg, T. Huang, H. Jayatissa, T. Lauritsen, S.F.D. McCaughley, X. Pereira-Lopez, I. Ragnarsson, S. Stolze, S. Uthayakumaar, and G.L. Wilson

Manuscript to be submitted to Phys. Rev. C in 2024.

Y. Hrabar: Formal Analysis (supporting), Investigation (supporting), Software (lead), Supervision (supporting), Validation (supporting), Visualization (supporting), Writing - original draft (lead), Writing - review & editing (lead)

Publications Not Included in This Thesis

Spectroscopy along flerovium decay chains: Discovery of ^{280}Ds and an excited state in ^{282}Cn

A. Såmark-Roth, D.M. Cox, D. Rudolph, L.G. Sarmiento, B.G. Carlsson, J.L. Egido, P. Golubev, J. Heery, A. Yakushev, S. Åberg, H.M. Albers, M. Albertsson, M. Block, H. Brand, T. Calverley, R. Cantemir, R.M. Clark, C.E. Düllmann, J. Eberth, C. Fahlander, U. Forsberg, J.M. Gates, F. Giacoppo, M. Götz, S. Götz, R-D. Herzberg, **Y. Hrabar**, E. Jäger, D. Judson, J. Khuyagbaatar, B. Kindler, I. Kojouharov, J-V. Kratz, J. Krier, N. Kurz, L. Lens, J. Ljungberg, B. Lommel, J. Louko, C-C. Meyer, A. Mistry, C. Mokry, P. Papadakis, E. Parr, J.L. Pore, I. Ragnarsson, J. Runke, M. Schädel, H. Schaffner, B. Schausten, D. A. Shaughnessy, P. Thörle-Pospiech, N. Trautmann, and J. Uusitalo

Phys. Rev. Let. **126**, 032503 (2021)
DOI: 10.1103/PhysRevLett.126.032503

Decay studies in the A∼225 Po-Fr region from the DESPEC campaign at GSI in 2021

M. Polettini, J. Pellumaj, G. Benzoni, J.J. Valiente-Dobon, G. Zhang, D. Mengoni, R.M. Perez Vidal, D. Genna, A. Bracco, G. Aggez, U. Ahmed, Ö. Aktas, M. Al Aqueel, B. Alayed, H.M. Albers, A. Algora, S. Alhomaidhi, C. Appleton, T. Arici, M. Armstrong, K. Arnswald, M. Balogh, A. Banerjee, J. Benito Garcia, A. Blazhev, S. Bottoni, P. Boutachkov, A. Bruce, C. Bruno, F. Camera, B. Cederwall, M.M.R. Chishti, M.L. Cortes, D.M. Cox, F.C.L. Crespi, B. Das, T. Davinson, G. De Angelis, T. Dickel, M. Doncel, R. Donthi, A. Ertoprak, R. Escudeiro, A. Esmaylzadeh, L.M. Fraile, L. Gaffney, E.R. Gamba, J. Gerl, M. Górska, A. Gottardo, J. Ha, E. Haettner, O. Hall, H. Heggen, **Y. Hrabar**, N. Hubbard, S. Jazrawi, P.R. John, J. Jolie, C. Jones, D. Joss, D. Judson, D. Kahl, V. Karayonchev, E. Kazantseva, R. Kern, L. Knafla, I. Kojouharov, A. Korgul, W. Korten, P. Koseoglou, G. Kosir, D. Kostyleva, T. Kurtukian-Nieto, N. Kurz, N. Kuzminchuk, M. Labiche, S. Lenzi, S. Leoni, M. Llanos Exposito, R. Lozeva, T.J. Mertzimekis, M. Mikolajczuk, B. Million, A.K. Mistry, A. Morales, I. Mukha, J.R. Murias, D. Napoli, B.S. Nara Singh, D. O'Donnell, S.E.A. Orrigo, R. Page, S. Pelonis, J. Petrovic, N. Pietralla, S. Pietri, S. Pigliapoco, Zs. Podolyak, C. Porzio, B. Quintana Arnes, F. Recchia, P.H.
Regan, J.-M. Regis, P. Reiter, K. Rezynkina, P. Roy, M. Rudigier, P. Ruotsalainen, E. Sahin, L.G. Sarmiento, M.-M. Satrazani, H. Schaffner, C. Scheiden-

berger, L. Sexton, A. Sharma, J. Smallcombe, P.-A. Söderström, A. Sood, P. Vasileiou, J. Vesic, J. Vilhena, L. Waring, H. Weick, V. Werner, J. Wiederhold, O. Wieland, K. Wimmer, H.J. Wollersheim, P. Woods, A. Yaneva, I. Zanon, J. Zhao, R. Zidarova, S. Ziliani, G. Zimba, and A. Zyriliou

Il Nuovo Cimento C **45**, 125 (2022)
DOI: 10.1393/ncc/i2022-22125-5

Spectroscopy along flerovium decay chains. II. Fine structure in odd-*A* ^{289}Fl

D.M. Cox, A. Såmark-Roth, D. Rudolph, L.G. Sarmiento, R.M. Clark, J.L. Egido, P. Golubev, J. Heery, A. Yakushev, S. Åberg, H.M. Albers, M. Albertsson, M. Block, H. Brand, T. Calverley, R. Cantemir, B.G. Carlsson, Ch.E. Düllmann, J. Eberth, C. Fahlander, U. Forsberg, J.M. Gates, F. Giacoppo, M. Götz, S. Götz, R.-D. Herzberg, **Y. Hrabar**, E. Jäger, D. Judson, J. Khuyagbaatar, B. Kindler, I. Kojouharov, J.V. Kratz, J. Krier, N. Kurz, L. Lens, J. Ljungberg, B. Lommel, J. Louko, C.-C. Meyer, A. Mistry, C. Mokry, P. Papadakis, E. Parr, J.L. Pore, I. Ragnarsson, J. Runke, M. Schädel, H. Schaffner, B. Schausten, D.A. Shaughnessy, P. Thörle-Pospiech, N. Trautmann, and J. Uusitalo

Phys. Rev. C **107**, L021301 (2023)
DOI: 10.1103/PhysRevC.107.L021301

Spectroscopy along flerovium decay chains. III. Details on experiment, analysis, ^{282}Cn, and spontaneous fission branches

A. Såmark-Roth, D.M. Cox, D. Rudolph, L.G. Sarmiento, M. Albertsson, B.G. Carlsson, J.L. Egido, P. Golubev, J. Heery, A. Yakushev, S. Åberg, H.M. Albers, M. Block, H. Brand, T. Calverley, R. Cantemir, R.M. Clark, Ch.E. Düllmann, J. Eberth, C. Fahlander,U. Forsberg, J.M. Gates, F. Giacoppo, M. Götz, S. Götz, R.-D. Herzberg, **Y. Hrabar**, E. Jäger, D. Judson, J. Khuyagbaatar, B. Kindler, I. Kojouharov, J.V. Kratz, J. Krier, N. Kurz, L. Lens, J. Ljungberg, B. Lommel, J. Louko, C.-C. Meyer, A. Mistry, C. Mokry, P. Papadakis, E. Parr, J.L. Pore, I. Ragnarsson, J. Runke, M. Schädel, H. Schaffner, B. Schausten, D.A. Shaughnessy, P. Thörle-Pospiech, N. Trautmann, and J. Uusitalo

Phys. Rev. C **107**, 024301 (2023)
DOI: 10.1103/PhysRevC.107.024301

α decay of the neutron-deficient isotope ^{190}At

A.N. Andreyev, D. Seweryniak, B. Andel, S. Antalic, D.T. Doherty, A. Korichi, C. Barton, L. Canete, M.P. Carpenter, R.M. Clark, P.A. Copp, J.G. Cubiss, J. Heery, **Y. Hrabar**, H. Huang, T. Huang, V. Karayonchev, F.G. Kondev, T. Lauritsen, G. Lotay, C. Müller-Gatermann, C. Page, D.H. Potterveld, P.H. Regan, W. Reviol, D. Rudolph, M. Siciliano, R.S. Sidhu, A. Sitarčík, P.J. Woods, Z. Yue, and W. Zhang

Phys. Rev. C **108**, 034303 (2023)
DOI: 10.1103/PhysRevC.108.034303

Manifestation of relativistic effects in the chemical properties of nihonium and moscovium revealed by gas chromatography studies

A. Yakushev, J. Khuyagbaatar, Ch.E. Düllmann, M. Block, R.A. Cantemir, D.M. Cox, D. Dietzel, F. Giacoppo, **Y. Hrabar**, M. Iliaš, E. Jäger, J. Krier, D. Krupp, N. Kurz, L. Lens, S. Löchner, Ch. Mokry, P. Mošať, V. Pershina, S. Raeder, D. Rudolph, J. Runke, L.G. Sarmiento, B. Schausten, U. Scherer, P. Thörle-Pospiech, N. Trautmann, M. Wegrzecki, and P. Wieczorek

Front. Chem. **12**, 1474820 (2024)
DOI: 10.3389/fchem.2024.1474820

Towards the discovery of new elements: Production of livermorium (Z=116) with ^{50}Ti

J.M. Gates, R. Orford, D. Rudolph, C. Appleton, B.M. Barrios, J.Y. Benitez, M. Bordeau, W. Botha, C.M. Campbell, J. Chadderton, A.T. Chemey, R.M. Clark, H.L. Crawford, J.D. Despotopulos, O. Dorvaux, N.E. Esker, P. Fallon, C.M. Folden III, B.J.P. Gall, F.H. Garcia, P. Golubev, J.A. Gooding, M. Grebo, K.E. Gregorich, M. Guerrero, R.A. Henderson, R.-D. Herzberg, **Y. Hrabar**, T.T. King, M. Kireeff Covo, A.S. Kirkland, R. Krücken, E. Leistenschneider, E.M. Lykiardopoulou, M. McCarthy, J.A. Mildon, C. Müller-Gatermann, L. Phair, J.L. Pore, 1 E. Rice, K.P. Rykaczewski, B.N. Sammis, L.G. Sarmiento, D. Seweryniak, D.K. Sharp, A. Sinjari, P. Steinegger, M.A. Stoyer, J.M. Szornel, K. Thomas, D.S. Todd, P. Vo, V. Watson, and P.T. Wooddy

Phys. Rev. Lett. **133**, in press (2024)

Source characterization of a detector for heavy and superheavy nuclei

P. Golubev, R. Orford, F. Garcia, D. Rudolph, L.G. Sarmiento, R. Clark, J.M. Gates, J. Gooding, M. Grebo, **Y. Hrabar**, T.D. Kramasz, M. McCarthy, M.A. Mohamed, J.L. Pore, and D.M. Cox

Submitted to Nucl. Inst. Meth. A (2024)

Acknowledgements

As I reach the end of my PhD journey, putting my emotions into words is not an easy task, but I will try my best. This journey would not have been possible without the people listed here.

First of all, I would like to thank Pavel, my main supervisor. I have learned so much from you and have truly come to share your passion for detectors. I hope I have begun to understand a bit of this art. The lab has become one of my favorite places. From chasing noise to talking philosophy, my PhD experience would not have been the same without you. Our discussions of nuclear physics always opened up more exciting questions to explore. Thank you for your endless support - every time I came to your office, I knew that you would provide me with the support and solutions I needed.

To Pico, I would like to thank you for sharing your expertise on DAQs and Geant4, both being equally complicated and fascinating at times. Thank you for providing insights into the realms of digital electronics and simulated events, and for sharing your sour goodies with me. All beam times and all meals shared, from giant schnitzels to tacos with rice, are fondly remembered.

To Dirk, I would like to thank you for being an exemplary scientist. I have always been able to trust your attention to detail, which has greatly reduced my anxiety. Your work ethic and dedication to supporting students are truly admirable. Thank you for your guidance. I would not have been able to navigate the complexities of experimental work without you.

To Claes, for always being cheerful and excited about the research in the group.

I would also like to thank former members of the research group who were part of my journey. I attribute my great knowledge of Fusion 360, Inkscape, and vacuum pumps to Danny. The trips to GSI and a suspicious van are well remembered. Thank you, Anton, for introducing me to your superheavy research and for sharing your positive outlook on life. Thank you, Ulrika, for all the hard work you put into preparing the ANL campaign. Also thanks to all the students who did their bachelor's and master's projects with us for their enthusiasm.

For the scientists in Argonne's Physics division, thank you for your incredible efforts in making the experimental campaign possible during COVID-19.

Thank you also to the local theoreticians, Andrea and Gillis, for shedding some light on theoretical nuclear physics. Special thanks to Andrea for the fruitful work on the last article.

To all my office mates, Nicholai, Oscar, Belikse, Sten, Einar, and, for a short time, Antonio and Lovisa. Thank you for putting up with me and sharing daily PhD life from memes boards to 1 kg of sour candy from the USA.

To all members of the former Division of Nuclear Physics, thank you for many laughs and nice conversations during the majority of my PhD time. Thank you to Kristina for always setting an example of professionalism and for helping out during these years. To Joakim, thank you for the interesting discussions and conversation topics. To the aerosol group, for making the former Division a lively and animated environment.

Thank you to all members of the Division of Particle and Nuclear Physics for your efforts at making it a unified division. I am happy that I have met other PhD students through the new Division. Special thanks to Sten, Einar, Belikse, Erik, Anca, Chiara, and Antonio for brightening my days.

Thank you to my friends, especially Nathaly, Julia, Ilinca, Sahel, Lila, Marius, and Sabrina, for all the love and support I received during my PhD years. Thank you, Hirepan, for all the bright moments together.

Finally, I would like to express my gratitude to my family for their unwavering support and strength, especially to my mom and sister. I also want to thank my nephew and niece for always bringing a smile to my face, especially when I try to count how many teeth they have.

Popular summary in English

We and everything around us are made of atoms. Atoms consist of a core, called the atomic nucleus, which is made up of protons and neutrons, with electrons orbiting around. There are about 3,000 known combinations of protons and neutrons in these atomic nuclei, which we also call isotopes. Only about 250 of these isotopes are stable and do not change over time. The others are unstable and decay, releasing radiation and particles until they eventually become stable matter. The more unbalanced the ratio of neutrons to protons in a nucleus is, the more unstable it becomes. The extreme cases are called exotic nuclei. One of the ways an exotic nucleus can decay is by sending out a proton. This process can easily be 1 000 000 000 times faster than a blink of the eye. Capturing such fleeting events is thus extremely challenging.

This thesis focuses on developing better tools to study decays of rare and exotic atomic nuclei. Detectors for nuclear radiation are the tools experimentalists use to capture nuclear decays. Significant efforts are made in upgrading detectors and using multiple combinations of detectors that can catch both particles and γ rays emitted so that exotic nuclei can be studied through their decays. The more precise the measurements are, the more ability to explore their structure and behavior we have at hand.

This thesis deals with the upgrade of two such detector systems: a local setup for γ detection with new specialized shields that improve detection accuracy and a more advanced system combining detectors for both particles and γ rays, used at Argonne National Lab, USA, with advanced local detectors. The development work with the first system pushes the limits of sensitivity of our tools and is aimed in the future to be used for the study of superheavy elements. These have extreme proton numbers, so we can add them at the end of our Periodic Table of the Elements. With the second setup, several experiments worth months-long time were conducted giving access to many exotic atomic nuclei. Thanks to the setup and advanced analysis tools developed in this thesis, a new release of a proton from a rare form of the element gallium, ^{61}Ga, was captured. This experimental discovery helps to improve our theoretical models, and thus understanding of how nuclear forces work and how certain atomic nuclei decay.

The work in this thesis provides additional tools for studying many more rare elements. The elements are like tiny pieces of a complex puzzle. Detectors are like magnifying glasses to help us to find those puzzle pieces. Each discovery fills in a small part of the grand puzzle that helps us understand the history and evolution of the universe.

Populärvetenskaplig sammanfattning på svenska

Vi och allt omkring oss är uppbyggda av atomer. Atomer består av en kärna, kallad atomkärnan, som är uppbyggd av protoner och neutroner, och av elektroner som kretsar runt kärnan. Det finns ungefär 3 000 kända kombinationer av protoner och neutroner i dessa atomkärnor, som vi också kallar nuklider. Endast omkring 250 av dessa nuklider är stabila och förändras inte över tid. De andra är instabila och sönderfaller, vilket frigör strålning och partiklar tills de slutligen blir stabil materia. Ju mer obalanserat förhållandet mellan neutroner och protoner i en kärna är, desto mer instabil blir den. De extrema fallen kallas exotiska kärnor. Ett av sätten som en exotisk kärna kan sönderfalla på är genom att skicka ut en proton. Denna process kan vara upp till 1 000 000 000 gånger snabbare än ett ögonblick. Att fånga sådana flyktiga händelser är därför extremt utmanande.

Denna avhandling fokuserar på att utveckla bättre och mer sofistikerade verktyg, så kallade detektorer, för att studera sönderfall av sällsynta och exotiska atomkärnor. Betydande insatser behövs för att uppgradera detektorer och använda olika kombinationer av detektorer som kan fånga både partiklar och γ-strålar som avges när exotiska kärnor sönderfaller. Ju mer exakta mätningarna är, desto bättre förutsättningar har vi att utforska de exotiska atomkärnornas struktur och beteende. Denna avhandling fokuserar på att utveckla bättre och mer sofistikerade verktyg, så kallade detektorer, för att studera sönderfall av sällsynta och exotiska atomkärnor. Betydande insatser behövs för att uppgradera detektorer och använda olika kombinationer av detektorer som kan fånga både partiklar och γ-strålar som avges när exotiska kärnor sönderfaller. Ju mer exakta mätningarna är, desto bättre förutsättningar har vi att utforska de exotiska atomkärnornas struktur och beteende.

Denna avhandling handlar om uppgraderingen av två sådana detektorsystem. Det ena systemet är en lokal anordning för γ-detektion med nya specialiserade sköldar som förbättrar detektionsnoggrannheten. Det andra mer avancerade systemet, använt vid Argonne National Laboratory i USA, kombinerar detektorer för både partiklar och γ-strålar med avancerade lokala detektorer. Utvecklingsarbetet med det första systemet pressar gränserna för känsligheten hos våra verktyg och syftar till att i framtiden användas för studier av supertunga grundämnen. Dessa har extrema protonnummer, som kan komma att läggas till i slutet av vårt periodiska system. Med den andra uppställningen genomfördes flera tidskrävande experiment, som gav tillgång till flertalet exotiska atomkärnor. Tack vare uppställningen och de avancerade analysverktygen som utvecklats i denna avhandling, detekterades för första gången utsändandet av en proton från en sällsynt form av grundämnet gallium, ^{61}Ga. Denna experimentella upptäckt hjälper till att förbättra våra teoretiska modeller och därigenom förståelsen av hur krafter verkar inom atomkärnan och hur vissa atomkärnor sönderfaller.

Arbetet i denna avhandling ger ytterligare verktyg för att studera fler sällsynta grundämnen. Dessa grundämnen är som små bitar av ett komplext pussel. Detektorer är som förstoringsglas som hjälper oss att hitta dessa pusselbitar. Varje upptäckt hjälper till att fylla i en liten del av det stora pusslet som hjälper oss att förstå universums historia och utveckling.

Introduction

Since the formation of the field of nuclear physics at the beginning of the twentieth century, physicists have been striving for a deeper understanding of the intrinsic structure of atomic nuclei. Over the decades, detailed investigations of stable and near-stable isotopes have yielded a broad understanding of nuclear forces, shell structures, and decay mechanisms. As these well-characterized regions of the nuclear landscape have been extensively studied, the focus has shifted toward more exotic nuclei, which often lie far from the line of stability and exhibit extreme neutron-to-proton ratios. These exotic nuclei, with unique structural and reaction properties, offer critical insights into nuclear matter under extreme conditions, validating and challenging existing theoretical models. Experimentally, probing such nuclei requires increasingly sophisticated techniques, including advanced detector systems with higher resolution and sensitivity, and large-scale accelerator facilities capable of producing and isolating these short-lived isotopes. These innovations are essential for addressing the complex physics questions posed by these elusive systems, which hold key information about nuclear structure, astrophysical processes, and the limits of nuclear stability.

The nuclear structure group at Lund University specializes primarily in neutron-deficient nuclei close to proton dripline and superheavy elements, both representing extremes of the nuclide chart. The group conducts experiments at various international accelerator facilities such as Argonne National Laboratory, USA, Lawrence Berkeley National Laboratory, USA, GSI Helmholtz Centre for Heavy Ion Research, Germany, University of Cologne, Germany, and others. The group's expertise extends from advanced data analysis to detector technologies, with a focus on particle-γ in beam coincidence spectroscopy and decay spectroscopy. In addition to conducting experiments, the group actively contributes to the development and deployment of advanced detector setups, with significant efforts at enhancing the precision and sensitivity of experimental spectroscopic measurements. This means that the detectors and data acquisition systems comprising the experimental setups are typically developed in-house and then deployed to experimental facilities. The group also possesses expertise in the Geant4 Monte Carlo toolkit used for state-of-the-art detector setup simulations for verification of experimental findings. Finally, long-lasting close collaboration with nuclear structure theorists within the same Department ensures strong theoretical and experimental synergy.

In line with the group's tradition, the research presented in this thesis is divided into two main parts:

I. **Detector-focused work** with the aim of improving detection sensitivity, which includes:

   i. Construction and commissioning of an anti-Compton shield built out of BGO scintillation detectors for Compex Ge detectors resulting in Paper I.

   ii. Development of novel analysis tools for double-sided silicon strip detectors focused on light-charged particle spectroscopy leading to Paper III.

II. **Experimental studies** by conducting and analyzing a series of experiments with focus on particle-γ spectroscopy in the upper fp shell, more specifically:

   i. In-depth study of the decay of the 6526-keV 10^+ isomer in ^{54}Fe, detailed in Paper II.

   ii. Identification of a proton-emitting state in the odd-proton nucleus ^{61}Ga, described in Paper IV.

   iii. Unprecedented study of experimentally identified evaporated deuterons from $N = Z$ compound nuclei, presented in Paper V.

A general background to the thesis introducing and describing decay modes of exotic nuclei is presented in Chapter 1.

My research journey started with a project of developing an anti-Compton shield for the Compex Ge detectors in possession of the research group. Compex detectors are five novel electrically-cooled Ge detectors designed specifically for high-resolution X- and γ-ray spectroscopy of superheavy nuclei. Given the detectors' versatility, their application can be extended to other projects, for example, measurements of environmental samples. For all studies, the shield helps to reduce background in Compex γ-ray spectra and improve the peak-to-total ratio. Commissioning of the anti-Compton shield is published in Paper I and the details of the detector-development project from start to finish are presented in Chapter 2.

In parallel, since the start of my PhD work, I have been involved in the preparation, execution, and analysis of experiments conducted at the ATLAS facility at Argonne National Laboratory, USA in the summer of 2020. The experimental campaign focused on in-beam proton-γ coincidence spectroscopy of exotic odd-Z nuclei close to the proton dripline, heavier than ^{56}Ni, in the mass number $A \approx 60$ region. The details of the scientific motivation and analysis are presented in Chapter 3.

The development of new analysis tools for proton spectroscopy of silicon detectors that were at the core of the experimental setup resulted in Paper III. The silicon detectors employed represented a high granularity system that made it possible to experimentally distinguish in-beam evaporated deuterons from protons, which previously was hardly possible for this type of experiments. This opened up the possibility for a comparative study of deuteron vs. proton-neutron evaporation from $N = Z$ compound nuclei by means of high-resolution particle-γ spectroscopy. Chapter 6 provides additional insights into that study, which led to Paper V.

The second experiment of the campaign focused on the identification of a proton-emitting state in ^{61}Ga. This was successful with some 40 counts identified in 7 TBytes of recorded experimental data through a challenging multi-variable analysis. This work resulted in Paper IV with supplementary details presented in Chapter 4. The experimental identification of the state opens up the possibility for theoretical investigations concerning isospin symmetry of the mirror nucleus pair ^{61}Ga and ^{61}Zn especially given the fact that the former has a proton-unbound state. Background to the theoretical calculations included in the Paper is presented in Chapter 5.

Throughout my PhD project, I participated in experiments not only led by our research group in Lund but also in collaborations with colleagues from various universities and nuclear physics research centers across Europe and the US. My contributions span a wide range of activities, from hands-on tasks such as preparing and setting up detectors and electronics at major large-scale research accelerator facilities to data acquisition and analysis, culminating in the publication of results in peer-reviewed journals. The efforts of participating in other experiments are reflected in the list of publications that are not included in this thesis.

Finally, Chapter 7 provides concluding remarks on the thesis work and offers a perspective on future research directions.

Chapter 1

On exotic nuclei

Out of more than 3000 known nuclei, only 251 are stable. These stable nuclei achieve an ideal balance between the nuclear forces acting within the nucleus, primarily the strong nuclear force, which binds protons and neutrons together, and the repulsive electromagnetic force between protons. A stable neutron-to-proton ratio varies depending on the mass of the nucleus, for lighter systems stability commonly occurs when the neutron number equals the proton one ($N = Z$). However, for heavier systems, the growing Coulomb repulsion between more and more protons necessitates additional neutrons for stability, causing the line of stability to deviate from $N = Z$ towards $N > Z$.

While stable nuclei have been thoroughly studied, advancing our understanding of nuclear forces and structure, modern nuclear physics research focuses on the far reaches of the nuclide chart exploring exotic systems. Current research focuses on three main regions of interest:

(i) nuclei near the proton dripline, where exotic decay modes such as prompt proton emission provide insight into the limits of nuclear binding,

(ii) neutron-rich systems, which are critical for studying astrophysical processes like the rapid-neutron capture process and its role in stellar nucleosynthesis, and

(iii) superheavy elements (SHE), where scientists are searching for the "island of stability". These atomic nuclei are expected to exhibit increased stability, defying their rapid decay.

The chart of nuclides with several nuclei of interest highlighted is presented in

Fig. 1.1. One example is the odd-Z nucleus ^{61}Ga close to the proton dripline. The study of proton emission from this nucleus is one of the central topics of this thesis. Another focus is on $N = Z$ nuclei formed through fusion-evaporation reactions, such as ^{64}Ge, ^{56}Ni, and ^{52}Fe. The particle evaporation paths from those nuclei are explored. Moreover, the thesis presents detector development work intended to support future SHE studies. The upgrade presented here is for the detectors that have been already used for studying decays superheavy nuclei, for instance, $Z = 114$ ^{289}Fl [2, 3].

For experimental studies of these systems, several key aspects could be defined, such as understanding mechanisms of nuclear reactions for preparation of experiments, developing advanced detector technologies, and employing sophisticated multi-parameter analysis techniques for rare-events search. The resulting experimental data on these unstable nuclei are crucial for testing and refining current models of atomic nuclei.

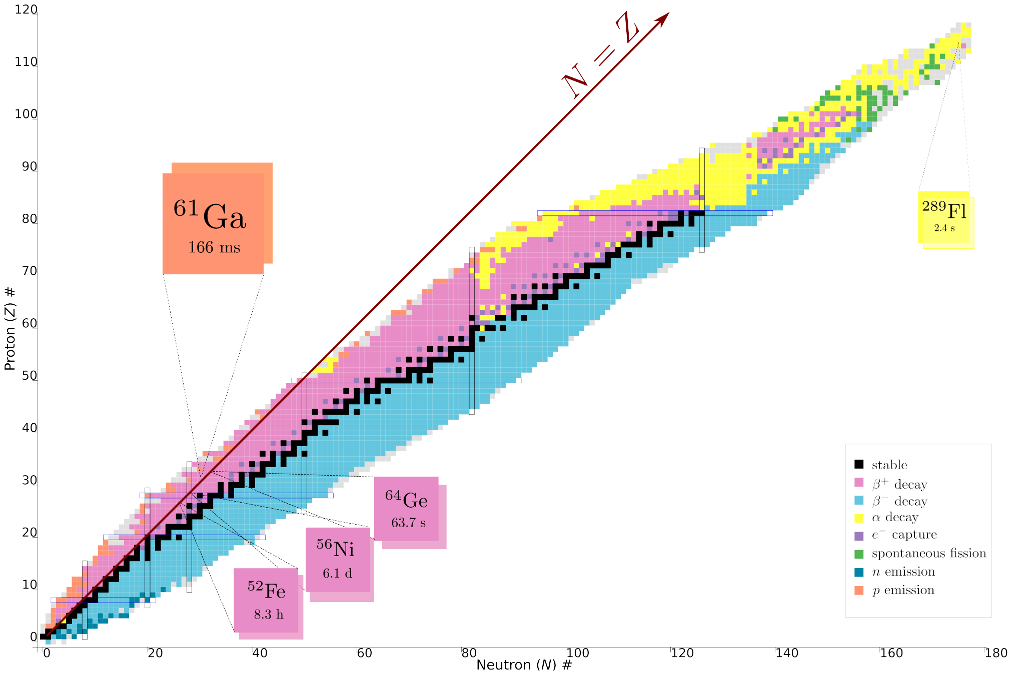

Figure 1.1: The chart of nuclides where all known isotopes are ordered with respect to their proton number, Z, and neutron number N. Black squares correspond to stable nuclei. Nuclei undergoing $\beta+$ decay are shown in pink, while $\beta-$ decay is indicated in blue. α decay and spontaneous fission are shown in yellow and green, respectively. Deexcitation through proton emission is indicated in orange. Nuclei with proton or neutron magic numbers are highlighted with rectangles. The $N = Z$ line is portrayed in dark red. The locations of the proton-emitting nucleus ^{61}Ga, and several other nuclei of interest in this thesis, for instance, $N = Z$ ^{64}Ge, ^{56}Ni, and ^{52}Fe are indicated. The position of the superheavy element ^{289}Fl is also specified. For further details see text. The figure is adapted from [1].

1.1 Nuclear reactions

Advancements in ion-beam techniques including the use of secondary radioactive ion beams have enabled researchers to produce and study exotic nuclei in greater detail, providing invaluable data on nuclear properties and reactions in regions that were previously unexplored. These nuclei can be produced through fission, fragmentation, or fusion reactions or studies using Coulomb excitation. Fragmentation reactions utilize high-energy beams of heavy ions to produce a variety of neutron-rich and proton-rich nuclei by typically breaking apart a beam nucleus into lighter fragments with subsequent separation of reaction products and extraction of nuclei of interest. Fission involves the splitting of a heavy nucleus, such as uranium or plutonium, into typically two lighter nuclei, predominantly generating neutron-rich isotopes while also releasing additional neutrons. In contrast, fusion reactions combine lighter nuclei to form heavier ones, primarily producing neutron-deficient isotopes.

Since the focus of this thesis is on neutron-deficient nuclei in the mass $A \approx 60$ region, fusion-evaporation reactions were employed. In particular, the evaporation of deuterons in coincidence with γ rays was studied experimentally for the first time, providing valuable insights into the reaction mechanisms involved. This novel approach has led to a deeper understanding of these processes, contributing to Paper V and forming the basis of Chapter 6 in this thesis.

1.2 Advanced detector technologies

Modern experimental studies of exotic nuclei and their decays require more advanced detector technologies while maintaining data integrity, along with new analysis methods suitable to reproduce the complex phenomena involved. These technologies are essential for researchers to detect rare decay events, measure energy levels, and investigate the properties of unstable isotopes within sub-second time frames and with high precision. Enhanced detection sensitivity is essential for exploring the subtle features of nuclear reactions and understanding the dynamics of nuclear forces, particularly in systems that are far from the region of nuclear stability.

An upgrade of a detection system that has been implemented for superheavy research experiments is detailed in Chapter 2. Chapter 3 provides more information on improved analysis tools for prompt proton spectroscopy.

1.3 Exotic decay modes

Nuclei far from the line of stability could be especially intriguing and thus interesting to study as they exhibit exotic decay modes. These include spontaneous fission, where a heavy nucleus splits without external influence, neutron and proton emission, two-proton emission, two-neutron emission, or β-delayed neutron emission, where a β decay is followed by neutron emission. Studying these modes enhances our understanding of nuclear structure and reactions, particularly for isotopes far from the line of stability, and sheds light on the fundamental forces governing nuclear stability.

For example, with thorough investigation and understanding of proton emission, direct insight can be obtained into the structure and behavior of exotic nuclei, especially those far from stability. The nuclear decay mode of discrete-energy prompt proton emission from low-lying excited states has been previously established in neutron-deficient nuclei in the mass $A \approx 60$ region. It can compete with ordinary γ decay because of the low Coulomb barrier, which places the time scale of the emission into the 10^{-12}-10^{-15} s regime and allows their study in "prompt coincidence", $\Delta t \leq 100$ ns, with preceding and subsequent γ rays emitted from the parent and daughter nuclei, respectively. Since γ rays are observed prior to proton emission, "γ-delayed proton emission" has also been used similar to, for instance, the term "β-delayed neutron emission" mentioned earlier. Chapter 5 of the thesis presents the identification of a proton-emitting state in ^{61}Ga nucleus.

Chapter 2

Detector development

Anti-Compton shield for Compex detectors

Advancements in nuclear physics have been closely linked to developments in the instrumentation techniques for modern experiments, with detectors serving as primary tools for experimentalists. Significant endeavors are directed toward pushing the boundaries of observational limits. The Nuclear Structure Group at Lund University utilizes a novel array of composite high-purity Ge Compex detectors [4]. These innovative detectors exhibit exceptional energy resolution with a low energy registration threshold, enabling us to achieve heightened levels of detection sensitivity for decay spectroscopy of rare isotopes. However, like other Ge detectors, Compex detectors suffer from a relatively low peak-to-total ratio. To address this challenge, renowned γ-rays spectrometers such as Gammasphere, Euroball, and Miniball utilize bismuth germanate (BGO) scintillation detectors for Compton suppression [5, 6, 7]. This chapter delineates an anti-Compton shield (ACS) system composed of BGO scintillation crystals designed to encase the Compex detectors and serve as active shielding. Its primary function is to eliminate incomplete detection from Compton-scattered γ-rays. Moreover, the ACS offers passive shielding for Compex detectors against background radiation, such as ^{40}K decay, commonly encountered at experimental facilities. Readers are referred to Paper I for the performance testing results of the ACS with a Compex detector. The chapter provides more comprehensive insights into the research and development of the ACS, along with results from measurements conducted at various development stages and with different data acquisition systems.

2.1 Compton suppression

Ge detectors, due to their high energy resolution, are an excellent tool for γ-ray spectroscopy, however, they are known to suffer from low detection efficiency and low peak-to-total ratio (P/T). The majority of γ rays do not deposit their full energy in the Ge crystals, which results in a large Compton continuum in their energy spectrum. The latter complicates the identification of X rays and low-energy γ rays, which are often of prime physics interest. The situation can be improved with the use of so-called anti-Compton shields or Compton suppressors. The idea behind any ACS is to surround a Ge detector with high charge and volume density material in order to increase the probability of registering γ rays that may scatter out of the Ge detector. Scintillator detectors are ideal candidates for this purpose due to their high charge density and, therefore, high detection efficiency. For the Compex detectors, it was decided to construct an ACS using BGO scintillation detector elements. BGO crystals were chosen for several reasons: (1) high charge and volume density, (2) excellent detection efficiency, (3) relatively high light output per unit of deposited energy, (4) emission wavelength compatible with commercially available PMTs, (5) non-hygroscopic nature, (6) ease of mechanical processing and favorable crystal properties, (7) cost-effectiveness, and (8) high stopping power. Due to BGO's density, it provides excellent passive shielding on its own. The fact that the BGO crystals were assembled into detectors makes the shielding also active.

A simplified view of a Compex detector surrounded with BGO crystals is shown in Fig. 2.1. Ideally, a γ ray would deposit all of its energy to a Ge crystal resulting in a full energy deposition as marked with number 1. Number 2 shows a Compton scattering event, where the secondary γ ray scatters out from one Ge crystal into a neighboring one. In case the scattered γ ray deposits all of its energy in the neighboring crystal (number 3), there is a possibility to sum those energies in order to reconstruct the full energy of the γ ray. This procedure is called "add-back". Another scenario of a Compton-scattering event is shown with number 4. In case a γ ray scatters out of a Ge crystal into a BGO crystal and interacts there (number 5) then we can use this information in the analysis and remove the event from the Ge-detector energy spectrum. The add-back procedure together with the use of an active shield should result in an improved P/T and general spectroscopic quality.

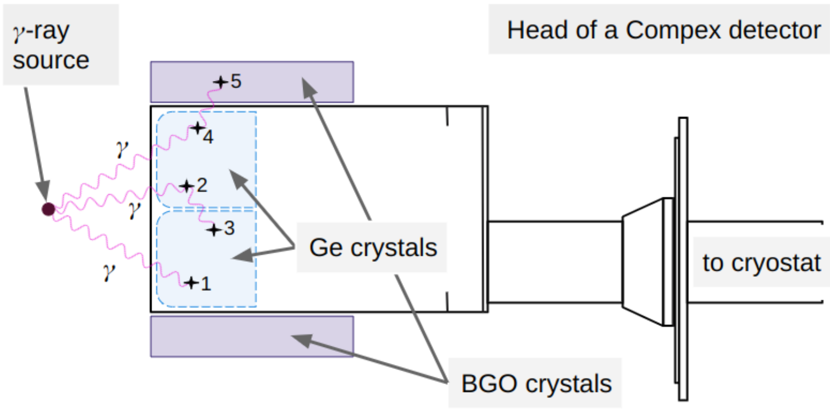

Figure 2.1: Two-dimensional schematic view of a head of a Compex detector with BGO detectors as part of an ACS indicated on top and bottom. The γ-interaction points are marked with numbers. Number 1 represents full γ-ray absorption in one of the Ge crystals of a Compex detector. A Compton-scattering event where a γ ray scatters from one Ge crystal into a neighboring one is shown with number 2. The scattered γ ray then deposits all of its remaining energy in the neighboring crystal (number 3). Number 4 shows a point of Compton scattering with a scattered γ ray depositing all of its remaining energy in a BGO crystal at interaction point 5.

2.2 Research and development (R&D) phase

This section covers the R&D phase of the ACS starting from bare BGO crystals and finishing with detector modules ready to be used with the Compex detectors.

2.2.1 Single detector development and testing

Development of an ACS for Compex detectors started from bare BGO crystals that had to be transformed into detectors. Bare BGO crystals of dimensions of $19.1 \times 19.1 \times 100.0\,\mathrm{mm}^3$ were ordered to be manufactured by Amcrys [8], a Ukraine-based company, one of a few in the world with the competence of growing BGO crystals of the desired cuboid shape and quality in large commercial quantity. The crystals for the project were delivered over the course of two years in batches of 15 crystals at a time. Each crystal came with factory specifications such as energy resolution, light output, and light linearity.

The first batches of crystals were subjected to various tests in order to study their response for an optimal ACS design. Each crystal was visually inspected for scratches and possible noticeable impurities. The crystals were wrapped with a reflective material, namely 3M$^{\mathrm{TM}}$ enhanced specular reflective foil [9], with circular openings for the optical coupling to the photomultiplier tubes (PMTs).

A photo of a batch of 15 wrapped crystals is shown in Fig. 2.2. The following tests were performed for site acceptance of the crystals: (1) absolute light output as a response to the standard gamma sources irradiating whole BGO sensitive volume, (2) light output linearity along crystal axis using collimate γ source, and (3) energy resolution.

The performance of single crystals was subsequently tested with a large spectroscopic Philips PMT and full BGO volume irradiation. For this, a wrapped BGO with one open side was optically coupled on the PMT with optic grease. The test with a standard ^{137}Cs source resulted in an average resolution of 14% at 662 keV for all detectors. This is in agreement with the specifications provided by the manufacturer. Light linearity tests of each crystal also showed satisfactory results.

Once the crystals passed the site acceptance, the next step was to attach a smaller PMT to the wrapped crystals that would fit the design specification, i.e., the compactness of a final pocket to be constructed. Hamamatsu PMTs from the H1317U-110 series [10] with a diameter of 17.5 mm and a length of 19.5 mm were chosen for the ACS. Fast response as well as compact size makes this PMT a very suitable choice for the application. The optic coupler Permacol® RTV615 AB [11] was used between a BGO crystal and its PMT to create an optical interface making it a single detection unit. The energy resolution test repeated this time with a Hamamatsu PMT gave an average result of 22% at 662 keV for a single BGO detection unit with 800 V applied.

Given the small differences of each crystal in (e.g., impurity level) and PMTs,

Figure 2.2: A batch of 15 BGO crystals wrapped with reflective material and prepared for connecting photomultiplier tubes.

each BGO detection unit is unique. Therefore, tests of light output as a function of voltage applied were made for voltages between 800 and 1000 V with 50 V-steps. This allowed to group detection units with similar light output into batches to be installed into the same pocket feed with the same HV source.

To complete the design of a single BGO detection unit, a pocket was designed in Fusion 360 software [12] and 3D printed from a black poly-lactic acid (PLA) material. Besides mechanical support, the pocket is needed to protect BGO detectors from external light during measurements as well as be vacuum compatible assembly. The pocket has openings for voltage and signal cables.

2.2.2 Pocket designs

After the individual BGO detectors were thoroughly tested, the next step was to assemble them around a Compex detector. A single-crystal pocket had to be expanded into a design that would solve the following challenges: (i) a design that would cover a significant part of a Compex detector without putting mechanical stress on the detector head of a Compex module (see Fig. 2.1), and (ii) at the same time packs all crystals closely together. The design needed to be vacuum-compatible, provide effective shielding for BGO PMTs against external light, and protect against potentially strong external magnetic fields, achieved by installing mu-metal shielding around each individual PMT, as is often required in experimental halls of accelerator facilities.

Another aspect to take into account is that five Compex detectors together with their ACS shields in a special configuration are envisioned to be a part of a Lundium decay chamber [13]. In fact, the Ge detectors were tailor-made for backing up a very compact, cubic-shaped arrangement of double-sided Si-strip detectors (DSSDs). The latter are used to detect the implantation of rare isotopes as well as their charged-particle decays. Thus, an additional design challenge for an ACS pocket was to fit four ACS pockets on sides of four Compex detectors inside the vacuum chamber without moving the Ge detectors away from the Si box (Fig. 2.4 and cf. Fig. 1(a) in Paper I).

The practical implementation of the ACS included two designs, referred to as a “full pocket” and “corner pocket”.

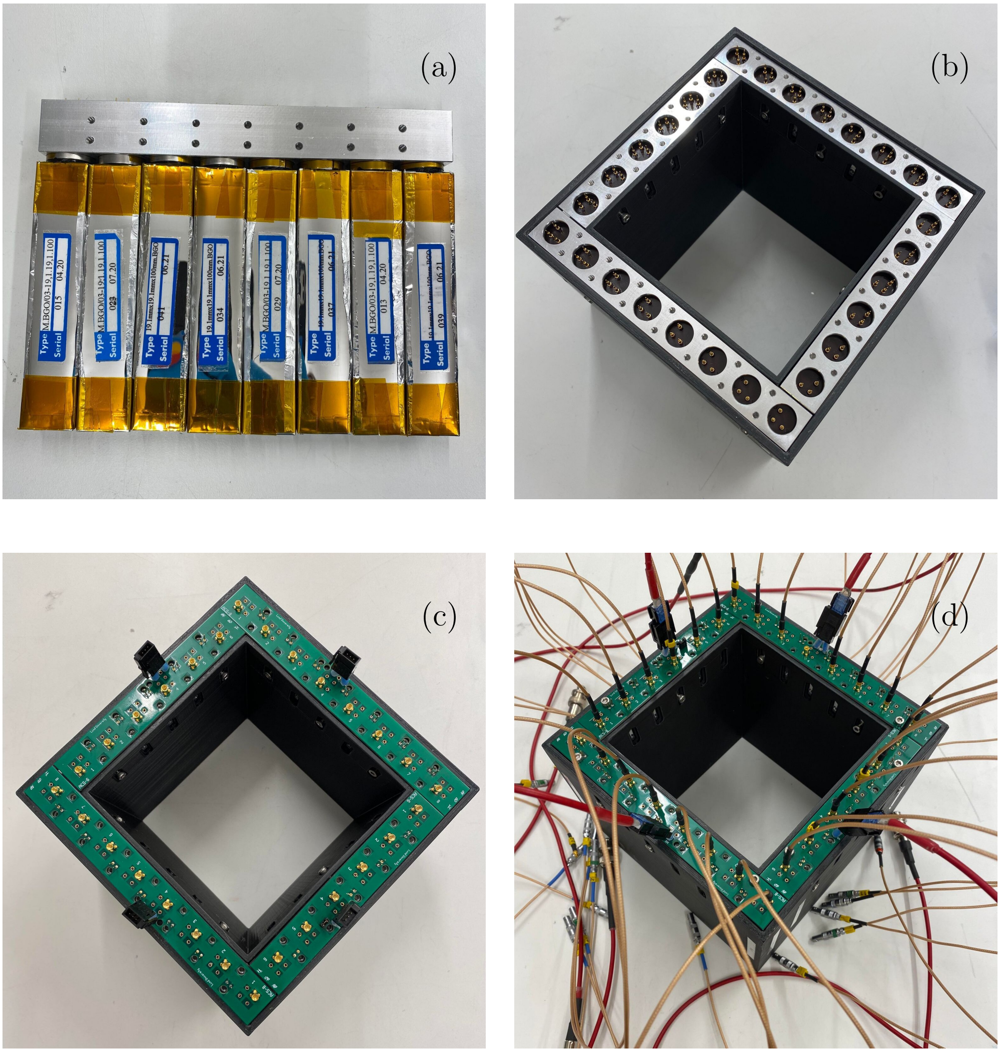

Figure 2.3: Construction phases of an ACS full shield. Panel (a) shows a batch of eight BGO detectors with a mu-metal shield. Panel (b) shows 28 BGO detectors placed inside of the 3D-printed pocket. For panel (c), the custom-made printed circuit boards (PCBs) and high voltage connectors are added. Panel (d) shows the completed ACS full pocket with signal cables and special high-voltage cables.

Full pocket design

The *single-crystal pocket* was expanded into a design that would allow to cover a Compex detector from all four sides. This is the so-called "full pocket" design illustrated in Fig. 2.3. This design of the ACS incorporates 28 BGO detectors. The pocket is used as a mechanical structure that holds separate BGO detectors together. At the same time, it also protects PMTs of BGO detectors from external light. The pocket was printed from the PLA material. PLA is one of the most popular 3D printing materials available and due to its density and thickness it does not interfere with γ rays and hence, is an excellent choice for the BGO housing. Other PLA key characteristics such as high structural hardness, very good flexural strength, and good impact strength make it acceptable from a mechanical point of view as well. The pocket was designed using software Fusion 360® and printed by the 3D printer Ultimaker 3®.

Different construction phases of the full ACS pocket are shown in Fig. 2.3. The design of the full pocket relies on a block concept. Two kinds of specially designed PCBs to fit the ACS pocket were custom-produced for batches of eight and six detectors, respectively. Therefore, the crystals were grouped into batches based on their light output and operational HV. Mu-metal shields with tailored openings for the PMTs were put in order to protect them from strong electromagnetic fields which can be present at experimental facilities. A picture of a batch of eight BGO detectors with a mu-metal shield placed on top of their PMTs is shown in panel (a). Panel (b) shows a 3D-printed pocket that holds four batches. The block design permits partial disassembly of the pocket for maintenance. To facilitate the replacement or servicing of the photomultiplier tubes (PMTs), the PMTs are mounted using gold-plated pluggable pins, which are permanently soldered to the PCB board. Panel (c) shows the pocket with PCB assembled on top. Special high-voltage connectors (3M Mini-Clamp Latching Socket), designed for secure and convenient handling, were soldered onto the PCB to facilitate the management of high-voltage supply cables. MMCX connectors with a 50-Ω impedance and a passband of up to 6 GHz were employed for the anode signal transportation. The PCB design also includes the capability to multiplex signals from multiple adjacent crystals from one detector pocket. Finally, panel (d) shows the completed full pocket including signal cables (regular LEMO connectors on the other end) and high voltage (HV) cables.

The full pocket design could be used for any kind of measurement with a Compex detector. As a part of the Lundium decay station, the full pocket will be placed to shield the Compex detector that is placed behind the implantation and veto DSSDs.

Corner pocket design

A second type of ACS design, the so-called *corner design*, was developed to meet the requirements of the Lundium decay station. Limited space inside of the Lundium vacuum chamber together with a requirement of the four Compex

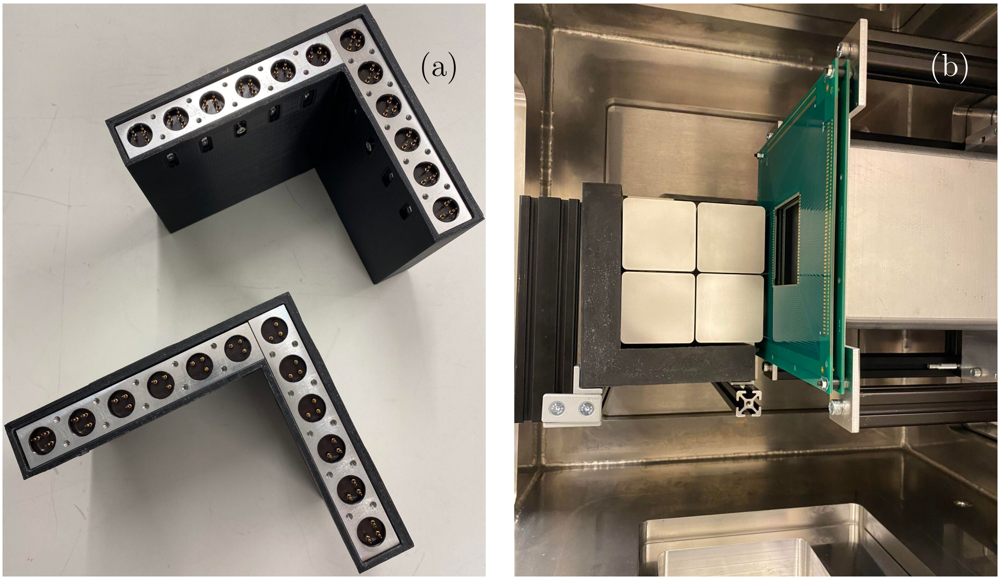

Figure 2.4: Panel (a) shows two ACS corner pockets comprising 12 BGO detectors each. Panel (b) exemplifies how such a corner pocket surrounds a Compex detector when placed inside the Lundium vacuum chamber.

detectors being close to the Si box detectors for optimal solid angle coverage called for a versatile pocket design in order to be used with the side Compex detectors. Detailed 3D modeling of the BGO detectors, the full pocket, and the Lundium setup allowed the optimization of the positioning of the different elements. As a consequence of this the corner pocket was established comprising 12 BGO detectors. Two uncabled corner pockets are shown in Fig. 2.4(a).

Four corner pockets are to be used when the Compex detector array is employed for measurements in different configurations. The standard configuration behind the Si detector box as a part of the Lundium decay station is illustrated in Fig. 2.4(b). A wall configuration, i.e., when Compex detectors are arranged into a 2D array and the corner shields surround them from outer sides is displayed in Fig. 2 of Paper I.

2.3 Measurements with a Compex detector

The full ACS pocket was installed around a Compex detector for a characterization and performance test with standard γ-ray sources: ^{137}Cs, ^{60}Co, and ^{133}Ba. Experimental data was taken simultaneously from four Ge crystals inside of the Compex detector and from 28 BGO detectors comprising the ACS. Experimental measurements were done with two different data acquisition systems (DAQs), one utilizing GSI-developed FEBEX3b digitizer cards and the other one using VME off-the-shelf components. The experimental measurements were cross-checked with state-of-the-art Geant4 Monte-Carlo simulations. The results of the measurements with the VME DAQ and their detailed comparison with Geant4 simulations are presented in Paper I. This section focuses on the comparison of measurements taken with the two DAQs vs. the simulation, and further details of the Compton suppression performance of the ACS shield not discussed in Paper I.

2.3.1 Measurement with FEBEX3b digitizer cards

For the measurements of a Compex detector with the full ACS installed, a Multi-Branch System (MBS) data acquisition system [14] was set up. The system used 16-channel, 14-bit, 50 MHz sampling analog-to-digital converter (ADC) FEBEX3b cards [15] for signals coming from both Compex and the ACS [Fig. 2.5(b)]. The idea was to have a general purpose DAQ using FEBEX3b cards for digitizing both Ge and BGO signals in coincidence as an isomorphic system, i.e., sharing the same structure of recorded data from both Compex and BGO detectors, for easier data analysis.

Within the data acquisition described above, FEBEX3b cards were used to digitize the preamplified signals of the four Compex Ge crystals. Because of the differential analog inputs of the standard FEBEX3b card (FEBEX-AD4), a GSI-developed daughter board FEBEX-AD4-NIM1 [16] was employed to handle the unipolar signals by the FEBEX3b card.

Signals from the ACS, which was in its prototype stage at the time, were also digitized using a FEBEX3b card. The PMT signals from the BGO detector units produce a pulse in the form of current, which required impedance matching to ensure compatibility with the FEBEX input as a necessary intermediate step. During the experiment, only 16 channels were available for use. For the investigation of the full ACS pocket, PMT output signals of two neighboring BGO units were combined for a total of 14 electronic channels. This impedance matching is required for an appropriate signal transmission from the high-resistance PMT output to the input impedance of the FEBEX daughter board [17]. The ACS pocket together with the impedance matching box is shown in Fig. 2.5(a). All tests were conducted applying -800 V to all PMTs individually.

Fig. 2.6(a) presents a simplified electronic schematic summarizing the signal processing for the Compex and ACS detectors. The acquisition system was triggered by any Ge crystal above a threshold corresponding to ≈ 15 keV photon energy. Dead-time locking was done using the GSI-developed EXPLODER card [18]. The BGO signals were digitized in coincidence though not included in the trigger scheme.

There were two major flaws in this first experiment conducted mid 2021: (i) lack of proper long-term background measurement with the Compex detector, (ii) use of vanilla firmware FEBEX3b to digitize Ge signals. FEBEX3b has been previously used in the group for the read-out of Si detectors, and the cards' firmware are not really tailored to process Ge signals. The flaws were realized at the stage of analysis and detailed comparison of measured data with simulated data. The results are discussed in Sec. 2.3.5.

2.3.2 VME measurement

As a way to tackle the issues mentioned above, a dedicated DAQ system using more Ge-specific electronic modules was set up. This time, commercially available CAEN VME ADC V785 [19] and time-to-digital converter (TDC) V775 [20] modules were used within the MBS framework to process Compex and BGO energy and time signals as depicted in Fig. 2.6(b). Measurements with Struck SIS3302 digitizer modules [21] for Ge detectors have proven to be reliable as they were used in many previous large-scale experiments [22].

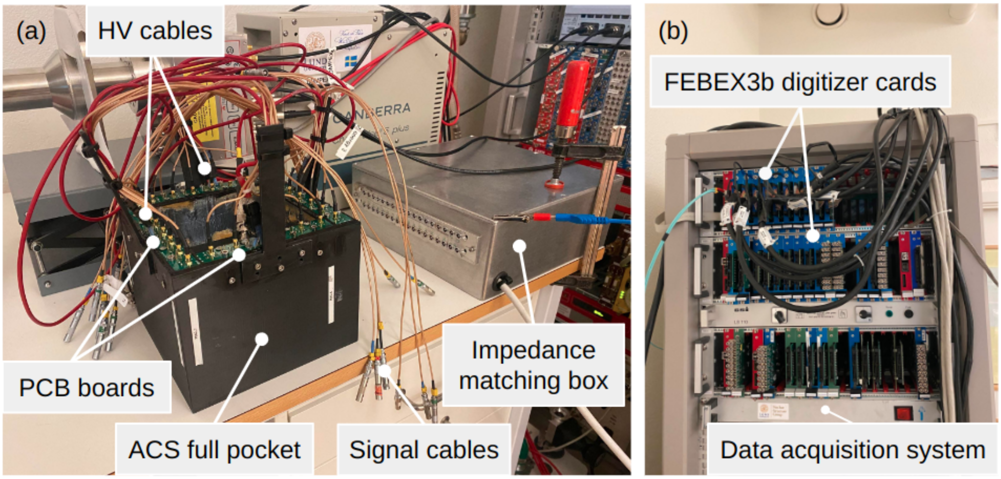

Figure 2.5: (a) Photo of the completed ACS pocket containing 28 BGO detector units with further components: PCB electronics boards, HV and signal cables. The impedance matching box was designed for BGO signal pre-processing. (b) Photo of the data acquisition system used for Ge and BGO signal processing with FEBEX3b digitizer cards.

Signals from ACS detectors also underwent enhanced signal processing focused on more advanced BGO information processing. By the time of the second measurement in the first half of 2023, the ACS pocket, along with the finalized PCB and high-voltage cables, had been fully completed. The signals from the BGO detectors were combined into 20 to match the number of impedance-matching box channels available for the measurements. The BGO signals, processed through the impedance matching box, were fed into two MESYTEC MSCF-16 shaping and timing amplifiers. The amplified energy and time signals were digitized by one MESYTEC MADC32 [23] ADC and one CAEN V775 TDC, respectively.

The acquisition system was triggered by any Ge detector crystal registering a signal above a set threshold corresponding to $\approx 15\,\mathrm{keV}$ photon energy. A validated trigger request generates a 5-μs wide gate, which is sent to the peak-sensing ADC module, while a delayed common stop signal is fed to the TDC modules. The trigger validation and dead-time locking [see Fig. 2.6(b)] is performed by a GSI-developed VULOM1 [24] VME module. The BGO signals were were not included into the trigger scheme and therefore were digitized passively except for the case related to their own energy calibration.

Measurements with this DAQ system were presented in Paper I.

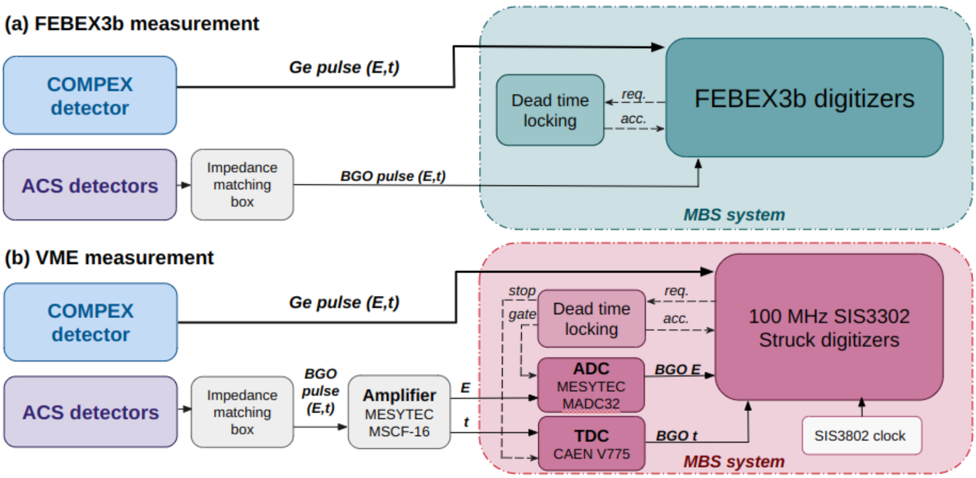

Figure 2.6: Simplified electronics scheme for the DAQ system of a Compex detector with ACS measurements. Panel (a) shows the signal processing scheme for the FEBEX3b measurement. Panel (b) shows the scheme for the VME measurement. For triggering the DAQs, see text.

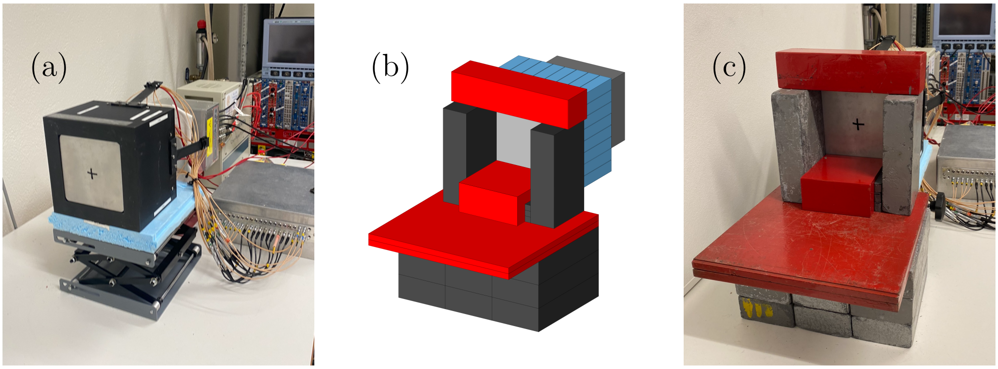

Figure 2.7: Comparison of experimental and simulated setups of a Compex detector surrounded by a full ACS shield. Panel (a) shows the experimental setup (black) and panel (b) the setup render produced in Geant4 including the lead shielding. Panel (c) shows the experimental setup with lead shielding in front.

2.3.3 The detector response simulations

The experimental measurements were cross-checked with state-of-the-art simulations in Geant4 Monte Carlo toolkit [25, 26, 27]. A detailed model of a Compex Ge detector has been previously implemented in Geant4 [28]. An early version of the ACS shield with 28 BGO crystals was implemented in Geant4 for early studies to motivate the construction of the shield [29]. Once the full ACS pocket construction was accomplished, the simulation model was revisited and updated to match the experimental setup as closely as possible. Final refinements, such as incorporating a lead shield in front of the setup, were introduced to better reproduce the experimental spectra. This inclusion allowed for matching features like the lead X rays observed in the experimental data. The experimental setup, both as realized in the laboratory and implemented in Geant4, is illustrated in Fig. 2.7. For further details on the simulation, see Sec. 4.2 in Paper I.

2.3.4 The data analysis

Experimental data collected from the standard γ sources was stored in the form of list-mode data (LMD) files generated by the MBS system. The binary data acquired by the DAQ with FEBEX3b digitizers and other front-end modules included both energy and timing information for hits detected in both Ge and BGO detectors. The isomorphic design of the system allowed the timing information from BGO hits to be aligned with Ge detector data, enabling direct comparison with timing information of Ge hits for prompt coincidences. In the case of measurements with the VME DAQ, only BGO hits occurring within the coincidence window set by the hardware trigger were recorded, so no additional software conditions were required. In the case of Geant4 simulations, a simulated event represents the full decay of one nucleus of a given isotope. Data generated by Geant4, i.e. the energy deposition recorded in the detectors on an event-by-event basis, was stored in a ROOT Tree. Simulated data does not include pileups and represents idealized conditions.

The analysis of the experimental and simulated data was performed using the GSI Object Oriented On-line Off-line (Go4) framework [30]. The implementation of the Go4 analysis code included three main steps: unpacking, mapping, and analysis. The unpacking step for the measured data meant simple reading in binary files and creating experimental events. The mapping step included calibration of the Ge and BGO detectors. Separate calibration procedure for each crystal and each measurement was performed to ensure optimal alignment. For measurements conducted using the VME DAQ, baseline correction was applied individually to each Ge crystal. The BGO detectors were calibrated through measurements with a ^{137}Cs source, using DAQ systems that triggered exclusively from the BGOs signals. Regarding the Geant4 generated data, during the unpacking step, simulated hits were treated to construct virtual events resembling those from laboratory measurements. This was followed by the mapping stage, where simulated events were further matched identical to the experimental events, including mapping detector IDs, marking neighboring BGO crystals to Ge crystals, etc. This enabled the application of identical analysis procedures to both experimental and simulated events.

At the beginning of the analysis step, the final matching of the experimental and simulated events was implemented. Simulated Ge hits below 10 keV were removed to match the lower experimental thresholds of the Ge crystals. Simulated and experimental ACS spectra for ^{137}Cs source measurement are presented

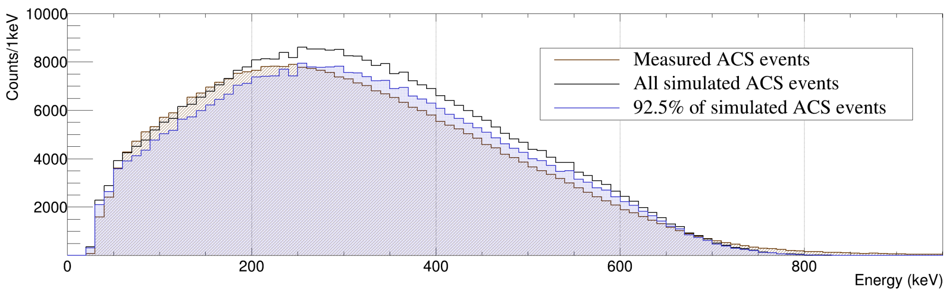

Figure 2.8: Measured (brown) and simulated (blue) ACS energy spectra for the measurement with a ^{137}Cs source placed at 200 mm in front of a Compex detector with the full ACS pocket. Note that the ACS is not the triggering system. The simulated ACS spectrum with 8.5 % of simulated BGO events removed is shown in light blue.

in Fig. 2.8. Presented ACS data contains the sum of all spectra of BGO detectors. The normalization factor used to align the statistics for the Compex singles spectrum is also applied to the measured ACS spectrum. The overall number of counts in the simulated BGO spectra exceeded those in the experimental BGO spectra by 8.5 %, i.e., the simulation is seemingly too ideal. The difference can be attributed to the lack of tracking optical photons in the present Geant4 simulations, which is beyond the scope of the present work. A simple, random removal of 8.5 % of simulated BGO events leads to a reasonable agreement between the simulated BGO spectra with the experimental ones.

Finally, with the aim of achieving P/T improvement, the Go4 analysis step included three main possibilities: (i) applying the Compton suppression procedure, (ii) summing hits in the Ge crystals, namely the add-back procedure, and, (iii) a combination of the add-back and Compton suppression procedures based on different γ-ray interaction possibilities as depicted on Fig. 2.1. The first analysis option included looking for prompt geometrically possible coincidences between a Ge crystal and any of the neighboring BGO detectors. Such coincidences were presumed to be γ rays which Compton scattered out of the Ge crystal into the ACS. The corresponding counts were excluded from the resulting Compex spectra. The second analysis option was implemented for events with multiplicity $N_{Ge} = 2$, i.e., two γ-ray hits inside of the composite Compex detector. If those hits occurred within a prompt time window ($\Delta t = 400\,\mathrm{ns}$), the energies were summed. Finally, the third option included the combination of the previous two, the Compton suppression procedure followed by the add-back procedure for the $N_{Ge} = 2$ events. For further details on the data analysis, the reader is referred to Sec. 4.3 in Paper I.

2.3.5 The results

Comparisons of different DAQ systems

Fig. 2.9 displays energy spectra of a standard ^{137}Cs source placed at a distance of 200 mm in front of a Compex detector cup obtained during measurements with three different DAQs: (a) MBS DAQ with FEBEX3b digitizers, (b) MBS DAQ with VME digitizers, and (c) a measurement with standard analog readout electronics. Measured energy spectra are normalized and compared to two versions of the Geant4 simulation. The spectra are shown for the region starting from the Compton edge and including the full energy peak to highlight the main discrepancies between the experimental data and simulations.

Panel (a) shows a comparison of the Ge spectrum (dark brown) with Geant4 simulation version one (v1) (light blue). This version of the simulation includes an additional ^{40}K background added alongside the ^{137}Cs source in order to mimic the background levels present for the first measurements for which there is a lack of background subtraction. There are two major aspects to highlight. First, the asymmetric shape of the full energy peak present in the measured data with a significant left tailing (circled and marked as ROI). Second, there is a higher number of counts between around 620 keV to the full energy peak, so-called "triangle", present only for experimental data. Therefore, a re-measurement with a more Ge-specific DAQ system, including VME modules dedicated to Ge-detector processing, was carried out in an effort to address the issues.

Measured with the VME DAQ (light brown) and simulated v2 (dark blue) energy spectra of the ^{137}Cs source are shown in Fig. 2.9(b). Note that background is removed from the measured spectrum and version two (v2) of the simulation does not include any additional ^{40}K. It is important to compare the new spectrum taken with the VME digitizers (b) to the previously discussed FEBEX3b measurement (a). It is noticeable that both the FWHM and overall shape of the full energy peak have been significantly improved. This is a consequence of the baseline restoration routine applied through the use of VME modules, which was not feasible with the FEBEX3b card firmware. However, a noticeable "triangle" feature remains evident still present even in the spectrum from the VME measurement. In order to further investigate if the "triangle" issue relates to experimental flaws, or rather is related to the simulation itself, measurements with a classic analog system were performed. A signal from a single Ge preamplifier was fed into the Ge-specific shaping Ortec 672 amplifier module [31], digitized with a multichannel analyzer (MCA) [32], and recorded

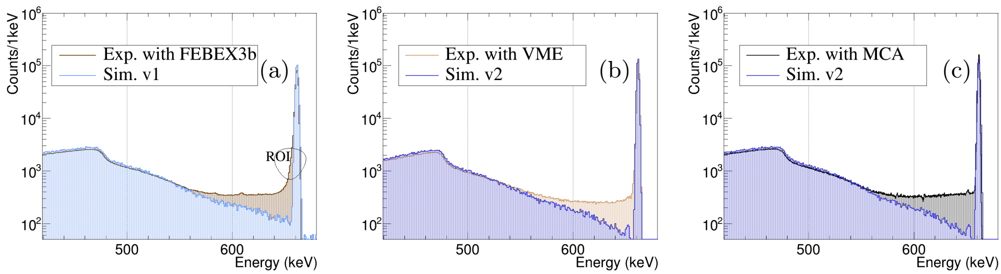

Figure 2.9: Comparison of part of ^{137}Cs spectrum from a Compton edge to end of the full-energy peak taken with a Compex detector using digital electronics - measurement with (a) the FEBEX3b DAQ, (b) the VME modules DAQ, and classical analog electronics (c) vs. simulated spectra. Simulation v1 includes ^{40}K to mimic the background present for the FEBEX3b measurement. The background is removed for experimental measurements shown in panels (b) and (c). Each experimental measurement is normalized to simulated data at a region from 200 to 400 keV.

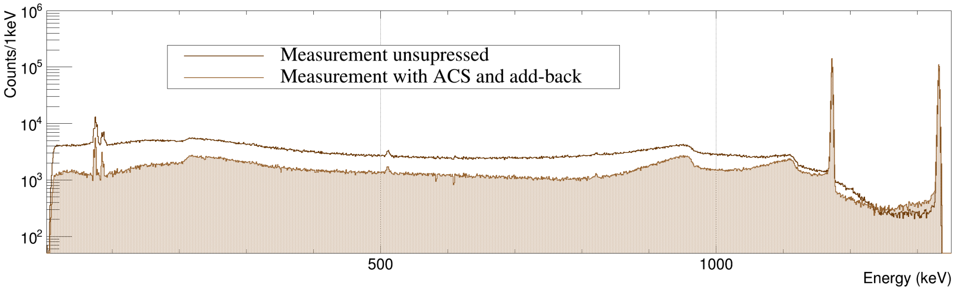

Figure 2.10: ^{60}Co γ-ray energy spectra from the Compex detector surrounded by the ACS full pocket. The unsuppressed spectrum is presented in dark brown. The γ-ray spectrum after applying the add-back and Compton suppression procedures is depicted in light brown.

with Maestro software [33]. The spectrum is presented in (c). It is apparent that the "triangle" structure is present even for the measurement with classical electronics. It is thus concluded and also mentioned as one of the highlights in Paper I, that this relates to charge-collection effects not being accounted for in our Geant4 simulations, which are noticeable in log scale at this level of attention to detail. Performing a comprehensive and detailed simulation of the Ge detector is a highly ambitious challenge, and therefore requires more verification. A more detailed study is considered to be beyond the scope of the present thesis work.

Anti-Compton shield performance

Energy spectra of a standard ^{60}Co source measured by a Compex detector in combination with the ACS full pocket are presented in Fig. 2.10. A spectrum with applied Compton-suppressed and the add-back procedure is displayed in light brown. A significant reduction in the Compton scattering region is observed when comparing the spectra before and after suppression. Another notable aspect worth mentioning is the presence of additional counts before the full energy peaks in the spectrum with the ACS and add-back procedures applied. This is a consequence of the add-back procedure, where the energy summation does not lead to the full energy peak, due to small losses of γ-ray energy or incomplete detection.

Measured and simulated relative improvements in performance for the combination of a Compex detector with the ACS for ^{60}Co, ^{137}Cs, and ^{133}Ba sources placed at 200 m distance are summarised in Table 2.1. P/T values are calculated for γ-ray energy regions indicated in the integration columns. For example, in the case of the ^{60}Co source, the P/T was computed as a ratio of 1172-keV

Table 2.1: Relative improvement in measured and simulated P/T values from the Compex detector with the ACS using standard sources placed along the central axis of the Compex detector at distance 200 mm. Integration limits for P/T are presented in columns two and three. Measured and simulated improvement, calculated as relative to singles increase in P/T ratio after the Compton-suppression procedure, add-back procedure, and both combined, is shown in columns denoted as "ACS", "add-back", and "total", respectively.

Source	Integration		Measured imp. in P/T (%)			Simulated imp. in P/T (%)		
	E_γ (keV)	total (keV)	ACS	add-back	total	ACS	add-back	total
^{60}Co	1172 1332	100 - 1350	34.5(3)	55.8(3)	112.6(4)	33.7(3)	43.1(3)	99.0(4)
^{137}Cs	662	100 - 700	26.4(2)	29.8(2)	68.1(2)	26.9(4)	35.8(4)	77.9(5)
^{133}Ba	356	100 - 500	9.9(3)	18.1(3)	30.7(4)	9.9(3)	18.3(3)	31.3(3)

and 1332-keV peak intensities, and the total number of counts in the region $E_\gamma = [100, 1350]$ keV. P/T values for each measurement are presented in Table 1 of Paper I. Regarding the Compton-suppression performance of the ACS, experimental P/T ratios are significantly improved for all three sources. While the simulated results for the suppression performance are in excellent agreement with the experimental results, simulations suggest a more pronounced improvement when using the add-back procedure. This is expected as simulation allows for ideal reconstruction of events, as discussed in Paper I. The exception to this trend is the ^{60}Co measurement, where the relative improvement after the add-back procedure is larger in measured data rather than in the simulation. This discrepancy could be potentially explained by the observed difference in P/T ratios for singles spectra, namely a larger number of counts observed in simulated full-energy peaks when compared to the measured ones before applying any of the P/T improvement procedures. The calculated integral of the experimental peaks in the case of the ^{60}Co source is 85 % of the simulated result for raw data normalized in the 300 to 900 keV region. This implies an overestimation of the photopeak efficiency in the present Geant4 simulation, potentially linked to the charge collection effect mentioned in the discussion of different DAQ systems. Despite the discrepancies, the experimental results show a reasonable agreement with the expected values obtained by the Geant4 simulations.

2.4 Summary and Outlook

An anti-Compton shield for the five Compex detectors in Lundium setup was designed and completed. Two different pocket models were created. All five pockets for five Compex detectors were constructed and are ready to be used in experiments. The characterization of the full shield performance together with a Compex detector is completed and presented in Paper I. The experimental performance of the shield is in good agreement with the Geant4 simulations, although the matching of Geant4 spectra in greater detail to experimental data could be improved in future studies.

Comparing measurements taken with different data acquisition systems prove the reliability of the VME-based DAQ when it comes to Ge-detector measurements. Nonetheless, it would be interesting to compare Ge spectra taken with VME modules to new FEBEX4 cards, together with firmware tailored for Ge detectors. These were not available at the time of the measurements. In the future, measurements of Compex detectors with FEBEX4 modules, with their dedicated FPGA firmware, are planned.

The mechanical assembly of all five pockets on top of all Compex detectors was tested during a beam time at the GSI Helmholtz Centre for Heavy Ion Research in 2022 for an experiment on neutron-deficient Pu isotopes. The experiment was a successful test to mechanically integrate the ACS as a part of TASISpec setup [34].

A combination of a Compex detector together with the full ACS and one DSSD has been put in place for environmental samples measurements.

In the future, the five ACS pockets are ready to use as with their respective five Compex detectors as a part of the Lundium decay station and other setups.

Chapter 3

Experimental campaign

Particle-γ spectroscopy in the upper *fp* shell

Studying nuclear structure is often done for nuclei close to the N=Z line. In heavier $T_z = \pm 1/2$ mirror systems, a good understanding of those nuclei defines its significance not only for continuum shell-model descriptions and the understanding of isospin-breaking interactions, but also for the astrophysical rapid proton capture, *rp*, process. The intrinsic structure of the nuclei can be revealed by conducting in-beam high-resolution particle- and γ-ray coincidence spectroscopy. An experimental campaign focusing on isospin symmetry and proton emission in the upper *fp* shell was conducted at Argonne Tandem Linac Accelerator System (ATLAS) facility, Argonne National Laboratory (ANL), Illinois, USA, in the summer of 2020. The experiments at ANL used Gammasphere [35], the Neutron Shell [36], the Fragment Mass Analyzer (FMA) [37], and a novel combination of charged particle detectors composed of the Microball CsI(Tl) array [38] and two CD-type double-sided Si-strip detectors (DSSDs) provided by Lund University. This chapter provides background as well as some general data handling methods enabling studying two main projects of the thesis: deexcitation of excited states of ^{61}Ga by discrete-energy proton emission presented in Chapter 4, and deuteron evaporation close to the N=Z line, Chapter 6. In the following sections, details of the analysis of the experimental data are elaborated on in-depth with a focus on charged-particle detectors and particle-γ coincidence techniques. This work resulted in Papers II and III.

3.1 Introduction

The experimental campaign consisted of five experiments with the Nuclear Structure Group from Lund University leading three of them. The first experiment (exp1239) aimed at exploring proton-emitting states in ^{57}Cu. The second experiment (exp1582) intended to study isobaric analog states in mass $A = 61, 62$ nuclei, and in particular proton emission from low-lying states in ^{61}Ga. The third experiment (exp1855) probed isospin symmetry at the limits of nuclear binding via proton-γ spectroscopy of ^{65}As. All three nuclei, ^{57}Cu, ^{61}Ga, and ^{65}As, are odd-Z, $T_z = -1/2$ nuclei.

The campaign was delayed three months due to the Covid-19 pandemic. Originally, it was scheduled for spring 2020, but the ATLAS facility closed for lockdown in March 2020. The official restart of the facility happened in June 2020 followed by preparations for the experiments. Restrictions due to the pandemic meant that only the local team could be present on-site and only in small groups at a time. The rest of the collaboration could only participate remotely with new tools and routines needed to be established first. Due to the limited manpower available for hardware troubleshooting during the experimental campaign, there were additional challenges in the recorded data sets. Some of these problems were revealed first during the offline analysis, with solutions outlined in Appendix B. It is important to note that the setup at ANL was non-standard and considerably more complex than usual.

The experimental results presented in this thesis originate from the first two experiments, namely exp1239 and exp1582. The scientific motivation behind each of the experiments is described in Sec. 3.1.1. The nuclei of interest were produced with fusion-evaporation reactions listed in Sec. 3.1.2. The experimental setup used in both experiments for the detection of evaporated particles, recoiling nuclei, prompt protons, and γ rays, is detailed in Sec. 3.2. Data acquisition systems used in the campaign are presented in Sec. 3.2.1. Since the focus of the campaign is on proton-γ spectroscopy, analysis of data from charged-particle detectors is elaborated in detail in Sec. 3.3. Finally, data analysis where information from all detector systems is used simultaneously is presented in Sec. 3.4.

3.1.1 Scientific motivation

The experimental campaign focused on exotic odd-Z, T_z = -1/2 nuclei close to the proton dripline starting in the near-spherical ^{56}Ni region and ultimately aiming towards the well-deformed nuclei in the vicinity of ^{76}Sr. The region corresponds to the upper fp shell, which includes the orbitals corresponding to valence protons and neutrons filling in the $2p_{3/2}$, $1f_{5/2}$, and $2p_{1/2}$ orbitals. This region is ideal for exploring isospin-breaking effects, as modern large-scale shell-model calculations allow to study their structure. Furthermore, just above ^{56}Ni, odd-Z, $N = Z - 1$ isotopes are either loosely proton-bound or unbound, with important implications for astrophysical processes like rapid proton or neutrino capture [39, 40]. The central motivation of the campaign is to incorporate information from the spectroscopy of prompt protons and use it to enhance our understanding of isospin symmetry, especially including nuclei with weakly-bound states.

Particle and γ-ray coincidence spectroscopy of ^{57}Cu (exp1239)

The first experiment of the campaign focused on ^{57}Cu, which has just one valence proton outside the doubly-magic $N = Z = 28$ nucleus ^{56}Ni. ^{57}Cu was produced by evaporating one proton and two neutrons ($p2n$ channel) following the fusion-evaporation reaction of a ^{36}Ar beam at 88 MeV with ^{24}Mg target nuclei. ^{57}Cu has a number of excited states that were found to undergo deexcitation by proton emission into the ground or the first excited state of ^{56}Ni [1, 41]. This includes a tentative proton $\pi g_{9/2}$ single-particle state at 3510(25) keV excitation energy [42]; the $I^\pi = 3/2^-$ ground state of ^{57}Cu is bound by only 690.3(4) keV [43].

During the same experiment, ^{54}Fe, which has a relatively long-lived isomeric state with spin-parity $I^\pi = 10^+$, was strongly populated through the $\alpha 2p$ channel. A study on the possibility of weak electromagnetic decay branches along the decay paths of this 6526-keV $I^\pi = 10^+$ isomer in ^{54}Fe resulted in Paper II. That study was an extension of a bachelor thesis project [44].

Isospin symmetry and proton deexcitation of ^{61}Ga in the upper *fp* shell (exp1582)

The two main scientific objectives of exp1582 were an in-beam proton-emission study of ^{61}Ga and identification of the excited states in ^{62}Ge. The experiment was a follow up for a predecessor experiment, RIB096, conducted in 2003 at Oak Ridge National Laboratory. RIB096 resulted in identification of the first excited states in the T_z = -1/2 nucleus ^{61}Ga [45], including suggesting a proton-emitting state. Excited states in the T_z = -1 nucleus ^{62}Ge could only be suggested [46]. Exp1582 employed the novel in-beam set-up tailored to proton-γ spectroscopy aiming at studying ^{61}Ga and ^{62}Ge with improved detection sensitivity.

Results from the ^{61}Ga study [45] suggested a proton-emitting $g_{9/2}$ single-particle state. Using $E_x(9/2^+;\ ^{61}\mathrm{Ga}) \approx E_x(9/2^+;\ ^{61}\mathrm{Zn}) = 2.4$ MeV together with the known binding energy, one can estimate $Q_p \approx 2150$ keV [43] for a proton emitting $9/2^+$ state in ^{61}Ga into the ground state of ^{60}Zn. This Q_p value is very similar to the energies known for $g_{9/2}$ prompt proton deexcitations from deformed to near spherical states in the mass region [47]. As a result of exp1582 and extensive data analysis presented in this thesis, a coincidence between a 957.6(5)-keV γ ray and an 1876(24)-keV proton line was observed. This identifies the earlier suggested $g_{9/2}$ single-particle state in ^{61}Ga at E_x=2150(34) keV. The clear identification of the proton line together with an isospin-symmetry study in the upper fp shell by means of mirror-energy differences resulted in Paper IV. In-beam proton spectroscopy and tracking capabilities of the experimental setup leading to the discovery are described in Paper III. Details on the experimental setup are presented in the current chapter, while Chapter 4 focuses on prompt-proton line identification. Chapter 5 provides additional insights into shell-model calculations.

Reported ion-source problems towards the end of the RIB096 experiment prevented clear identification of excited states in ^{62}Ge [46]. From RIB096 two γ-ray transitions had tentatively been assigned to ^{62}Ge for the $4^+ \rightarrow 2^+ \rightarrow 0^+$ cascade. The tentative γ-ray transition of 964 keV is expected to be the yrast $2^+ \rightarrow 0^+$ ground-state transition. A study focusing on the identification of γ rays belonging to ^{62}Ge using data from exp1582 was performed by Dalia Farghaly in the frame of a Master's thesis project [48]. A preliminary search for ^{62}Ge transitions was conducted but proven unsuccessful. For details, the reader is referred to Ref. [48]. In the meantime, excited states in ^{62}Ge were populated in direct reactions of relativistic radioactive ion beams at RIKEN, Japan, and studied independently at JYFL-ACCLAB, Finland, using the ^{24}Mg(^{40}Ca,$2n$)^{62}Ge fusion-evaporation reaction [49], i.e., same reaction as exp1582. The first excited state in ^{62}Ge was identified at 965(1) keV, which is in excellent agreement with the previously suggested RIB096 result. Additionally, several additional transitions beyond the first 2^+ state in ^{62}Ge were also identified for the first time in the new experiments [49].

Prompt proton angular distribution

The high granularity of the DSSD-Microball system aimed not only at improving the precision of the energy measurement of protons but also at the measurement of the angular distribution of prompt protons. Greater detection sensitivity of the new setup aimed at a better definition of recoil velocity vectors, which can be used to better confine the spin axis of the particle-emitting residue on an event-by-event basis. In previous experiments focused on prompt particle emission, this was not possible due to low statistics and large spatial uncertainty.

Previous experimental results report proton emission from deformed to spherical nuclei, including ^{58}Cu [47]. Since the 2.8 MeV $g_{9/2}$ proton emission from the 3510(25) keV state in ^{57}Cu, which is the focus of exp1239, is spherical-to-spherical, the measurement of its angular distribution could provide an interesting insight into multi-dimensional quantum tunneling [50, 51]. In the present work, the angular distribution for ^{61}Ga prompt protons was measured and discussed in Sec. 4.4.3.

Deuteron evaporation close to the $N = Z$ line

During the offline analysis of the experiments, it was realized that the novel charged-particles detection setup is also capable of clearly distinguishing evaporated deuterons from evaporated protons. In combination with Gammasphere, this opens up for an unprecedented study of – possibly preferential – production cross sections along the $N = Z$ line involving the evaporation of deuterons for a series of compound and residual nuclei: for instance, $^{24}\mathrm{Mg}(^{40}\mathrm{Ca}, 2pn)^{61}\mathrm{Zn}$ vs. $^{24}\mathrm{Mg}(^{40}\mathrm{Ca}, dp)^{61}\mathrm{Zn}$. The results of this study are described in Paper V.

3.1.2 Fusion-evaporation nuclear reactions

As mentioned before, for the experimental campaign the fusion-evaporation nuclear reaction technique was employed to produce the exotic nuclei of interest.

During a fusion-evaporation reaction, an accelerated ion beam hits a target foil with an energy above or near the Coulomb barrier between the two participating atomic nuclei. As a result, a nucleus from the beam and the target can fuse, forming a compound nucleus. The compound nucleus is normally highly excited and therefore not very stable. Within a timescale of $\approx 10^{-19}$ seconds, the nucleus starts to emit light particles such as α particles, deuterons, protons, or neutrons. Hence, it loses a lot of its excitation energy by "evaporating" these light particles. When the residue on average is not excited enough to emit more particles, after about 10^{-15} seconds, it will instead continue by sending out first statistical and then, as the nucleus approaches the yrast line, discrete γ rays. The yrast line outlines the minimum excitation energy of a nucleus for a given angular momentum. The schematics of a fusion-evaporation reaction is depicted in Fig. 3.1 with an example of the fusion-evaporation reaction ^{24}Mg(^{40}Ca$, p2n)^{61}$Ga, where ^{61}Ga is depicted as a proton-emitting nucleus.

Because the underlying process is statistical, a compound nucleus can evaporate different number and combinations of particles. This leads to different residual nuclei, also referred to as different “reaction channels”. For example, $Z = 31$, $N = 30$ ^{61}Ga is produced as $p2n$ channel from the $N = Z = 32$ ^{64}Ge* compound nucleus.

During exp1239, a ^{36}Ar beam at 88 MeV and a ^{24}Mg target were used to produce the compound nucleus ^{60}Zn*. The target foil had a thickness of 0.43 mg/cm^2 and was isotopically enriched to 99.92%. The main reaction channel of interest for the experiment was $^{60}\text{Zn}^* \rightarrow {}^{57}\text{Cu} + 2n + p$. Another channel of importance included $^{60}\text{Zn}^* \rightarrow {}^{54}\text{Fe} + \alpha + 2p$ [44].

In exp1582 a ^{40}Ca beam at an energy of 106 MeV was used to bombard the same ^{24}Mg target foil leading to ^{64}Ge* compound nucleus. For that experiment, ^{61}Ga is of interest which comes from the evaporation of a proton and two neutrons, i.e., $^{64}\text{Ge}^* \rightarrow {}^{61}\text{Ga} + 2n + p$. For search of excited states in ^{62}Ge, the following reaction was used - $^{64}\text{Ge}^* \rightarrow {}^{62}\text{Ge} + 2n$ [48].

Additional compound nuclei were made as a result of contamination reactions,

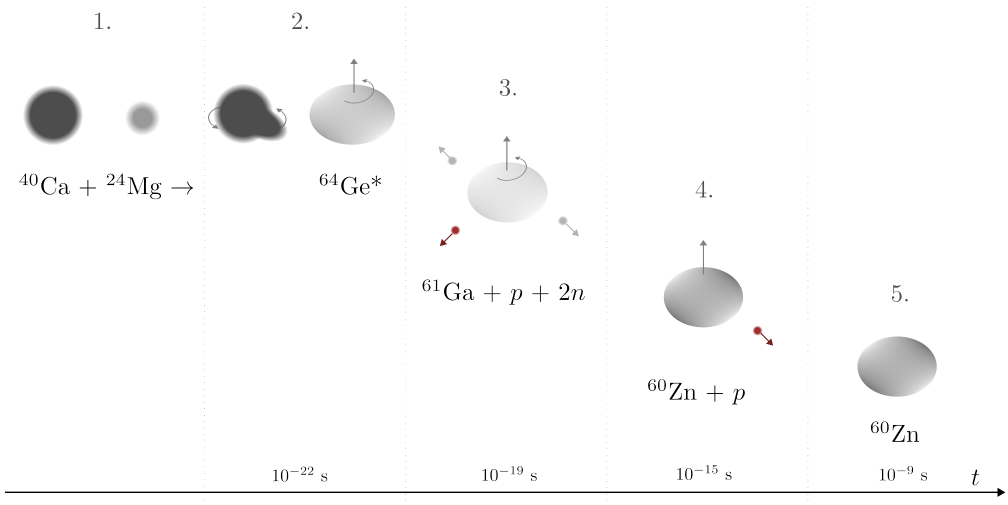

Figure 3.1: Schematic drawing of the fusion-evaporation process. The beam and target nuclei, ^{40}Ca and ^{24}Mg, are depicted at stage 1. The nuclei fuse to a highly energetic compound nucleus, ^{64}Ge (stage 2.). The compound nucleus releases its energy first through particle evaporation, for instance, one proton and two neutrons, as shown in stage 3. This results in excited ^{61}Ga recoil nucleus. Stage 4. indicates ^{61}Ga deexcitation through discrete proton emission into ^{60}Zn. The process ends in the ground state of ^{60}Zn (stage 5.). The x-axis provides a rough time scale of the various production and decay processes.

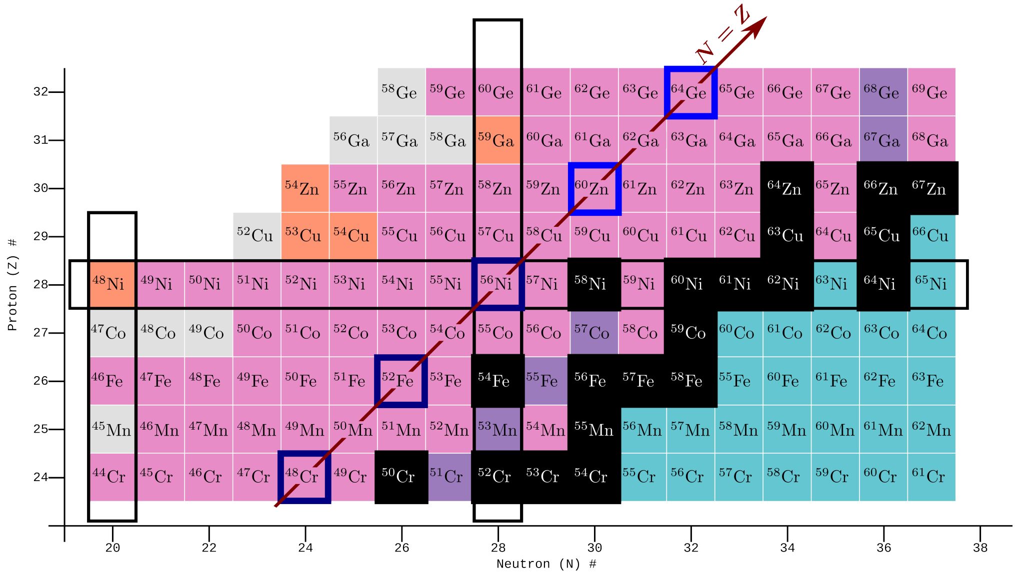

Figure 3.2: Part of the nuclidic chart showing compound nuclei produced during the $N = Z$ experimental campaign. Compound nuclei resulting from primary fusion-evaporation reactions in exp1239 and exp1582 are highlighted with blue frames. Dark blue frames indicate compound nuclei produced as a result of contamination reactions, either with oxygen or carbon build-up on the target foil. The $N = Z$ line is indicated in dashed red line. Figure adapted from [1].

namely the beam nuclei reacting with oxygen and carbon build-up on the surfaces of the ^{24}Mg target foil. This produces the following compound nuclei: ^{36}Ar + ^{12}C $\rightarrow$ ^{48}Cr*, ^{36}Ar + ^{16}O $\rightarrow$ ^{52}Fe*, or ^{40}Ca + ^{12}C $\rightarrow$ ^{52}Fe*, and ^{40}Ca + ^{16}O $\rightarrow$ ^{56}Ni*.

All $N = Z$ compound nuclei dealt with in the present thesis are shown in Fig. 3.2. A part of the thesis is exploring competing channels involving deuteron instead of one proton and one neutron, pn, evaporation leading to the same residual nuclei potentially populating different states. Notably, all residual nuclei are at or close to the $N = Z$ line which provides example cases for d vs. pn evaporation studies. The findings of that study are presented in Paper V.

3.2 Experimental setup

Several residual nuclei can be produced during a fusion-evaporation reaction. Therefore, different detector combinations have to be used for identifying nuclei of interest. In a typical Gammasphere plus Fragment Mass Analyzer (FMA) setup, γ rays are recorded with the Gammaphere Ge-detector array [35], and the recoil's mass number, A, and proton number, Z, are to be established from measurements with the Fragment Mass Analyzer (FMA) and an Ionization Chamber (IC) in its focal plane [37], respectively. Another way to select a recoil of interest is through the detection of evaporated particles. For an identification of channels resulting from the evaporation of neutrons, the Neutron Shell system of liquid organic scintillation detectors replaced a part of Gammasphere. For charged-particle detection, the array of CsI(Tl) detectors, Microball [38], was built primarily to fit Gammasphere. It is used around the target foil inside the vacuum chamber. Since the focus of the experimental campaign is the spectroscopy of protons coming from nuclear decay of low-lying discrete states, the need to properly record proton data goes beyond channel selection. Therefore, the experimental setup was enhanced with a combination of two CD-shaped double-sided silicon strip detectors, CD-DSSD, provided by Lund University. These were used together with the Microball detector array. The two ways of selecting a recoil of interest are complementary and when combined, as in our experiments, allow for a stricter or redundant selection. A simplified schematic of the full experimental setup is presented in Paper III and Supplemental Material to Paper IV. Photos of the main three detector systems of the upgraded setup, i.e. DSSD, Microball, and Gammasphere, are shown in Fig. 3.3.

Gammasphere

Gammasphere [35], an array of high-purity Ge detectors, was employed for γ-ray detection. In its full capacity, namely 110 detectors together with their surrounding BGO anti-Compton shields [52], an almost full 4π coverage around the target position is achieved. For the experimental campaign, 32 of the most forward Gammasphere detectors were removed in order to place Neutron-Shell detectors for neutron detection, thus leaving Ge coverage for a range of angles between 70° to 160° with respect to the beam direction. On average about 70 active Ge detectors with their respective shields were used during the campaign.

Prior to the experiments, a preliminary linear energy calibration of Ge detectors was done with measurements using a radioactive ^{207}Bi source. Between exp1239 and exp1582, comprehensive γ-ray energy and efficiency calibration data were taken using standard ^{133}Ba, ^{152}Eu, and ^{182}Ta sources placed at the center of the array. Peaks over a wide energy range from ^{133}Ba, ^{152}Eu, and ^{182}Ta sources were used for efficiency calibration [48].

The alignment of the Ge-detector energies for the first experiment was completed during the bachelor thesis work of Paul Böhm [44]. In this case, a re-calibration was done using peaks steaming from the decay of an isomeric state in ^{54}Fe and the 511-keV positron-electron annihilation peak. The work was followed with

$\gamma\gamma\gamma$-coincidences studies on transitions following the decay of the $I^{\pi} = 10^{+}$ isomer in ^{54}Fe, resulting in Paper II. For details on the analysis, the reader is referred to that publication and Ref. [44].

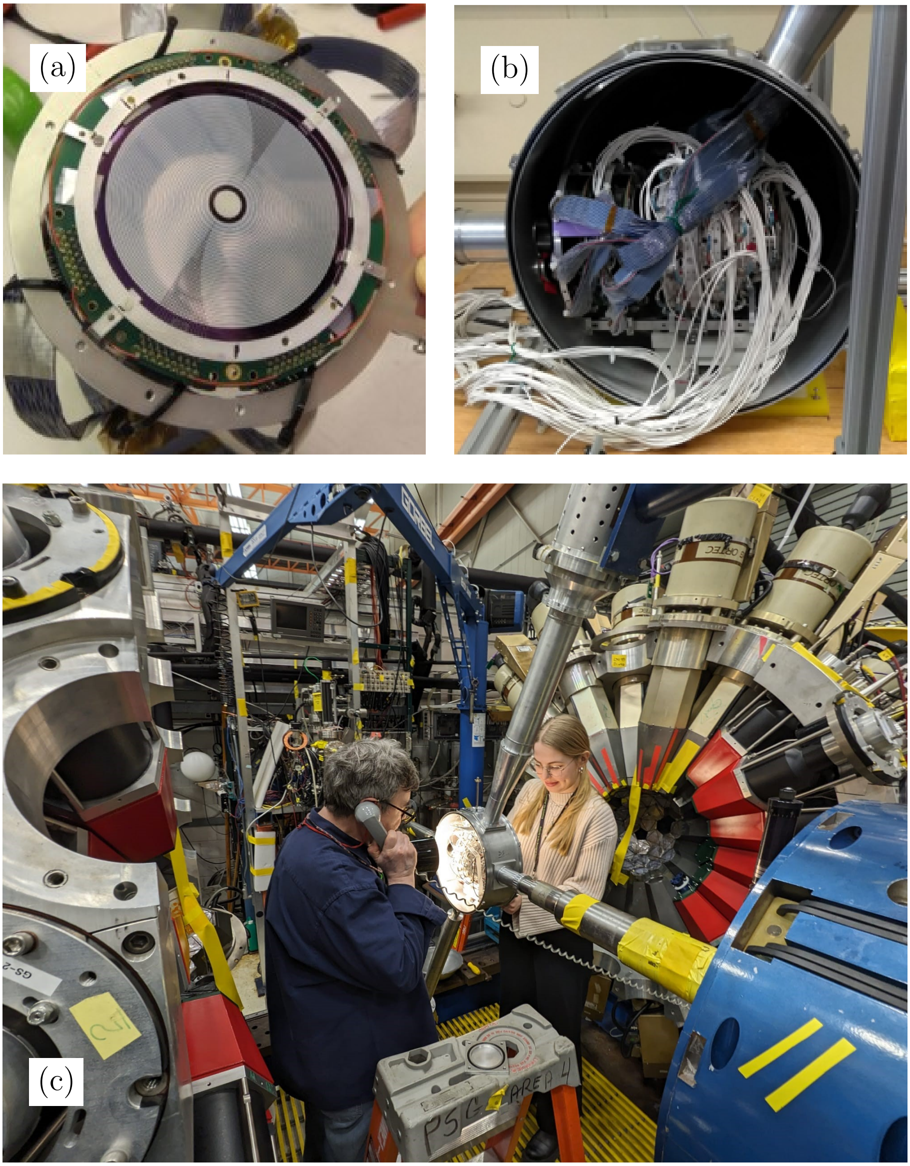

Figure 3.3: Photos of the detector systems of interest in the new upgraded Gammasphere setup. (a) Photo of the p-side junction of DSSD1. (b) CD-DSSDs together with Microball detector array inside of Gammasphere vacuum chamber. (c) Photo showing the beam alignment process with the Microball detector array with Gammasphere and neutron detectors (red) behind. Photos (b) and (c) courtesy P. Golubev and L.G. Sarmiento, respectively.

Extensive work on the improved calibration of Ge detectors for the second experiment during the offline analysis was done in the framework of the Master's thesis project by Dalia Farghaly [48]. First, several ^{152}Eu peaks were used for an improved linear calibration. Subsequently, a subset-dependent re-alignment was conducted using specific peaks in the in-beam data: 136.6 keV Couloum excitation peak from ^{181}Ta, the 511-keV positron-electron annihilation peak, and the 1732.2-keV Doppler-shifted line from ^{61}Cu.

For background and Compton scattered events suppression the Ge detectors in Gammasphere are surrounded with active anti-Compton suppression shields of BGO detectors. The latter were calibrated using also the ^{207}Bi source data.

Charged-particle Detectors

Since the experimental campaign focused on detailed spectroscopy of proton emission in prompt coincidence with γ rays, the charged-particle detector system and the associated data analysis are detailed in the dedicated Sec. 3.3.

Neutron Shell

The Neutron Shell [36], with up to 32 tapered hexagonal liquid scintillator detectors, was used for selecting neutron-evaporation channels. The neutron detectors replaced the corresponding forward Gammasphere detector modules, covering the laboratory angles $10^\circ \leq \theta_{NS} \leq 70^\circ$ with respect to the beam direction.

In order to distinguish between neutrons and γ rays recorded by the detectors, pulse-shape discrimination and the time-of-flight methods are used. For this, three parameters were recorded for each hit in neutron detectors: time, total energy, and tail energy. The ratio of the tail-to-total energy was computed as an additional parameter. Those parameters are plotted against each other into histograms as follows: time vs. total energy, total energy vs. tail energy, and time vs. tail-to-total energy ratios. This allows one to visually distinguish between low energy γ rays and neutrons as detailed in previous works [48, 53]. For each neutron detector, a combination was used of the three histograms for labeling a hit as a neutron for cleaner selection. Neutron-γ discrimination for exp1582 was also implemented in the framework of the Master's thesis of Dalia Farghaly [48]. The work confirmed the expected 30% efficiency for neutron detection in correctly registered events. However, during the offline analysis, it was discovered that only $\approx 1/8$ of the recorded data contained complete neutron information, i.e. timing coincidences with γ hits. Efforts to investigate and possibly recover missing statistics are described in Appendix B.2.

Fragment Mass Analyzer

The FMA [37] is a recoil mass spectrometer designed to separate recoils from the primary beam and to determine the mass number, A, of residual nuclei. The FMA consists of several magnetic quadrupoles, electrostatic dipoles, and a magnetic dipole. After the last magnetic quadrupole, a Parallel Plate Avalanche Counter (PPAC) detector is placed for the determination of A/Q value, where Q denotes the charge state of the recoiling ion of interest. The PPAC gives an X- and a Y- position for the recoils, which can be used for assigning the A value. Different parameters for the electromagnetic deflection of the FMA can be adjusted for optimal A separation with a focus on the desired A/Q value for reaction channels of interest for an experiment.

Due to a malfunctioning router, timestamps of PPAC signals in the data written for exp1239 and the majority of exp1582 were corrupted. The timestamps and thus correlations to Gammasphere were recovered as explained in Appendix B.1.

Ionization Chamber

The IC is placed at the end of the FMA for further classification of recoils through the determination of their proton number, Z. The IC at ATLAS consists of three individual sections with thicknesses of 50, 50, and 20 mm. The aim is to completely stop the recoils in the last section. A recoil going through the IC will transfer its energy to the gas medium of each of the IC parts resulting in current signals that can be individually read out. Summing the signals gives the total energy loss of a recoil in the detector. Therefore, using the IC it is possible to find the rate of energy loss in each section and total energy of a recoil. Since the energy loss is Z-dependent according to the Bethe-Bloch formula, it is thus possible to derive Z information for a recoil on an event-by-event basis.

3.2.1 Data Acquisition System

The data acquisition system for the experimental campaign consisted of three parts: Digital Gammasphere (DGS), Digital Fragment Mass Analyzer (DFMA), and the Washington University DAQ (WuDAQ). A simplified schematic of the full DAQ system is presented in Fig. 3.4. Hits registered by Gammasphere were handled by DGS with Ge traces taken, but only energy and timing information were stored. BGO energy and timing information was also recorded. To the DFMA, normally used for FMA detector systems, 2x(32+64) = 192 DSSD signals were connected. WuDAQ was used for recording signals from Microball and the Neutron Shell at first. Later on, duplicated neutron detector signals were additionally digitized by DFMA. Digitized Microball traces were recorded for the first time by DFMA as well, owing to problems with WuDAQ (see Appendix B.2).

The DGS and DFMA systems had a common trigger with two "clean Ge" signals, i.e., signals corresponding to the full-energy deposition of two γ rays in two Ge detectors with no registered scattering in their respective BGO shields.

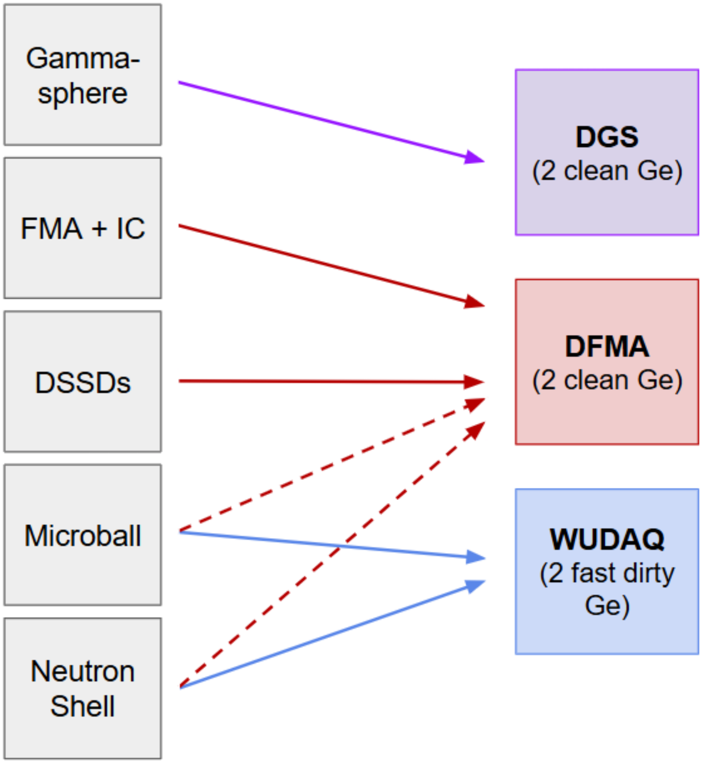

Figure 3.4: A simplified schematics of the three data acquisition systems used during the experimental campaign: DGS, DFMA, and WUDAQ. In parenthesis, the trigger requirements of each system are given. Solid arrows represent digitized signals coming from different detector systems into the three DAQs. Dashed arrows represent duplicated signals from Microball and Neutron Shell detectors into DFMA, see text for details.

WuDAQ had 2 fast "dirty" Ge hits, i.e., in coincidence with hits in BGOs, as the trigger to the system, since recording fast timing is important for neutron-γ discrimination. Combining the three DAQ systems with different trigger conditions resulted in difficulties, i.e., part of the neutron data remained uncorrelated to the rest as mentioned previously in Sec. 3.2 and detailed in Appendix B.2.

Due to issues with one of the routers in the DFMA, the timestamps from the PPAC detector in the focal plane of the FMA together with part of the Microball and Neutron Shell detector signals were partially corrupted throughout exp1239 and exp1582. As a result, parts of the data appeared uncorrelated with Gammasphere. The corrupted timestamps in both experiments were corrected, as detailed in Appendix B.1.

The experimental data was stored in files referred to as runs corresponding to approximately one hour of beam time. Each run consisted of three separate binary files recorded by each of the three DAQs. Data processing and analysis were done with the analysis codes GEBMerge and GEBSort [54] adapted from the originally developed ones at the ATLAS facility. The analysis codes are written in C, C++, and ROOT [55, 56]. GEBMerge goes through the three recorded files per run and creates a single output file with all subevents sorted in chronological order. The GEBSort code consists of functions allowing to read-in the time-ordered subevents, process them, and, produce an output ROOT file with histograms of interest.

The data was stored and analyzed first on Aurora [57] and later on the new iteration, COSMOS [58]. These are cluster computer resources available at LUNARC [59], the center of scientific and technical computing at Lund University.

3.3 Charged-particle detectors

A charged-particle detector system with high granularity was required to enable high-resolution particle-γ coincidence spectroscopy. In order to achieve this, two CD-shaped double-sided Si strip detectors (CD-DSSDs) were added to the Microball array. One ring of Microball (R4), comprising 12 CsI(Tl) elements, was taken out in order to fit the Si detectors at forward angles. The CD-DSSDs cover angles from $12°$ to $53°$ relative to the beam direction. The setup is tailored for inverse kinematics reactions, where the reaction products are strongly forward-focused due to the conservation of momentum. Thus, the CD-DSSDs are placed in the Microball with the idea of detecting the majority of the prompt protons. The advantages of employing this complex setup for proton detection are listed in Paper III. This section focuses on analyzing the data collected with charged-particle detectors. Details on calibration, internal detector correlations, tracking capabilities and, last but not least, particle identification are given.

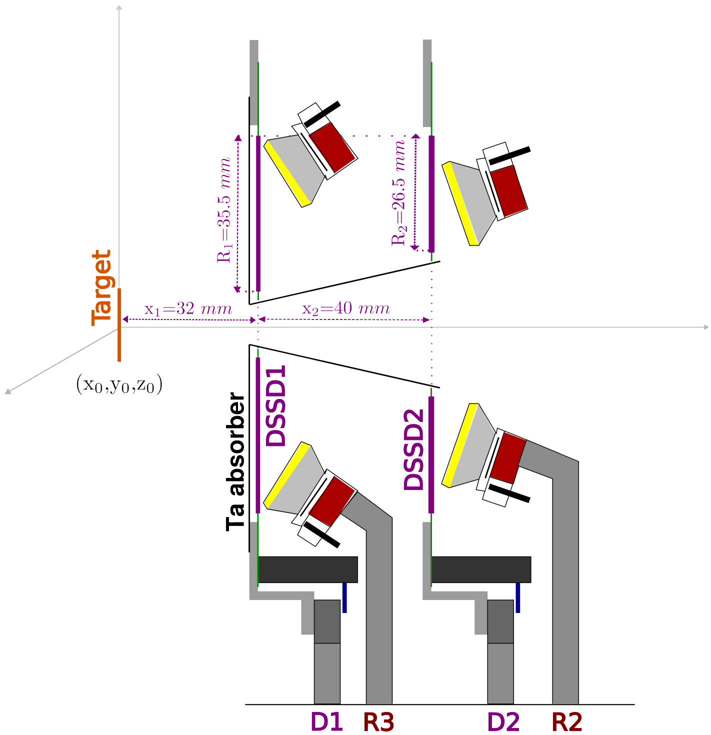

Figure 3.5: Simplified schematics of the combined setup of the two CD-DSSD detectors and Microball array with respect to the target. One ring of Microball array (R4) is taken out to fit the CD-DSSD detectors. Distances from the target holder and sizes of the DSSD detectors are given in purple. Adapted from original sketch by D. Rudolph and W. Reviol.

3.3.1 CD-DSSD detectors

The two CD-shaped DSSD detectors are 310 and 520 μm thick, respectively. DSSD1 is placed at 32 mm distance from the target, while DSSD2 is placed at 72 mm distance as depicted in Fig. 3.5. The detectors are designed to allow for most of the residual nuclei to continue to the FMA. Therefore, they have circular openings of 10 mm diameter in DSSD1 and 28 mm in DSSD2, while the outer active area diameter is 85 mm for both. The p-side (front) of each detector is divided into 64 sectors and the n-side (back) comprises 32 rings. Combining signals from the p- and n- sides of a detector allows having a pixelated setup.

Each CD-DSSD gives rise to 32 x 64 = 2048 pixels. The two DSSD detectors are also different in their segmentation: while rings of the DSSD2 are equidistant, in DSSD1 the width of the rings decreases from the inner to the outer part, with the innermost ring being 1.6 mm wide, while the outermost ring is 1.0 mm wide. Technical sketches of the two DSSD detector geometries are included in Appendix A.

Tantalum absorber foils

To protect the DSSDs from scattered beam, Ta absorber foils were added to the setup in front of DSSD1 and through the circular openings of the Si detectors.

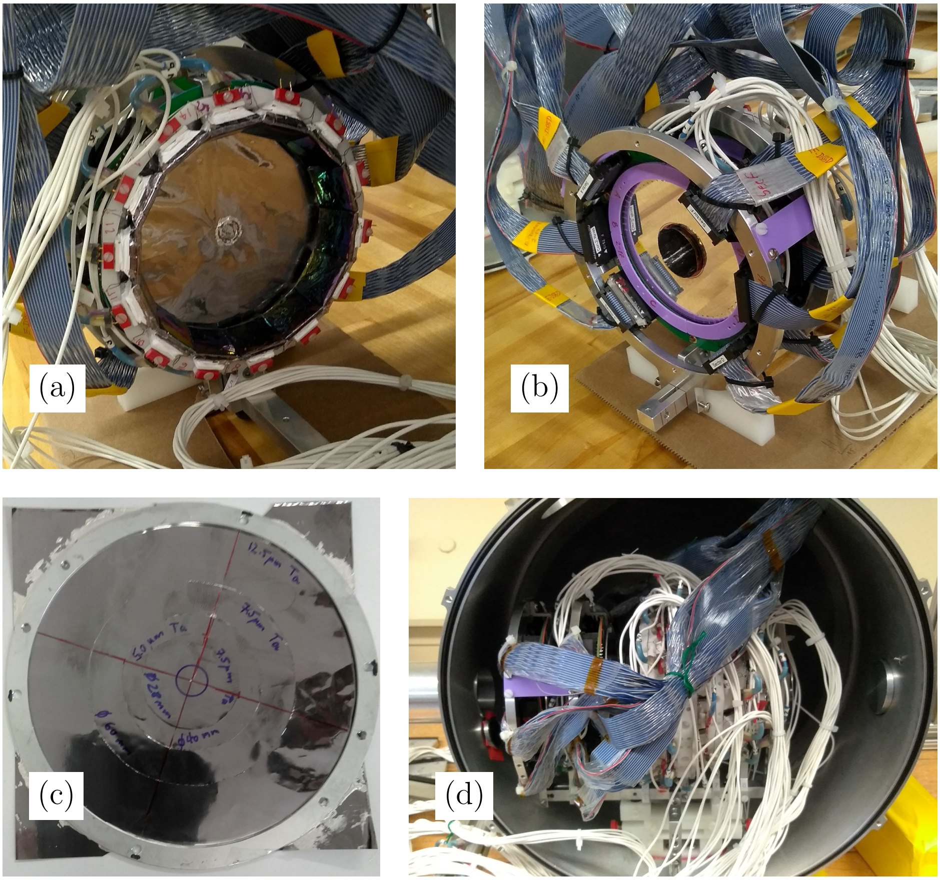

Figure 3.6: Pictures of Ta absorber foils attached to the CD-DSSD system of detectors. (a) A front view on the CD-DSSD system: a stack of Ta absorber foils was placed in front of the p-side of the DSSD1 detector. (b) A view from the back: part of a cylinder made from Ta absorber is visible through the hole of DSSD2. (c) Picture of the stack of Ta absorber foils placed in front of DSSD1 as shown in (a) with different thicknesses indicated. (d) Picture of the system of DSSDs detectors assembled with Microball and placed inside of Gammasphere vacuum chamber. Pictures courtesy of P. Golubev.

Photos of the foils are shown in Fig. 3.6. A stack of five absorber foils of different diameters and thicknesses (c) was placed in front of DSSD1 following the circular shape of the detector. The foils have a circular opening of 7 mm in diameter to allow recoil passage to the FMA. The thickness of the absorber layer in front of the active area of DSSD1 gradually decreased from 32.5 μm to 12.5 μm from innermost to outermost rings of DSSD1.

Geant4 simulation

The CD-DSSD detectors, along with Ta absorber foils, were implemented in Geant4 [25, 26, 27] to closely replicate their actual geometries. These simulated geometries included the unique ring division of DSSD1 and the equidistant rings of DSSD2, along with the division of both detectors into sectors. The simulation also accounted for varying radial thicknesses of Ta absorbers positioned in front of DSSD1 in the experimental setup. The output of the simulations included energy, ring id, and sector id per DSSD, enabling comparison with experimental data.

The primary motivation behind the Geant4 simulation of the DSSD detectors was to assist in setting up the experimental campaign. Specifically, the simulations aimed to investigate the angle-dependent energy loss of protons and α particles in the absorber foils and the two DSSDs. The study helped also to find the optimal electronics settings for the Si preamplifiers used during the experiments. For this purpose, PACE2 [60] output for the ^{40}Ca and ^{24}Mg fusion-evaporation reaction was read into Geant4, exploiting all evaporated particles. Simulated ΔE-E spectra were used to estimate energy ranges of proton and α particles for recording the experimental data.

During the offline analysis, the simulated model assisted the analysis of experimental data, namely light-charged-particle selection in experimental energy loss spectra. This is described in more detail in Sec. 3.3.6. The simulations also played a crucial role in the final stages of data preparations, namely in the verification of Ta-absorber energy correction for protons emitted by ^{61}Ga and their energy calculation in the center-of-mass frame. This is described in Sec. 4.2.3.

3.3.2 Microball

DSSDs are used for forward angles of looking in the beam direction. To ensure full angular coverage for charged-particle detection altogether, the Microball detector array was used. In full, Microball comprises 95 CsI(Tl) scintillation detector elements, from which 12 detectors corresponding to R4 were physically removed to fit in the Si detectors. On average, 75 working CsI(Tl) elements were used in the campaign. Panel (d) in Fig. 3.6 is a picture of the Microball array together with the DSSDs detectors as a part of the experimental setup.

3.3.3 Calibration

CD-DSSD detectors were calibrated based on the energy loss of protons in Si of a given thickness. Base calibration was done in preparation for the experimental campaign based on proton range correlations in DSSD1 and DSSD2 with proton energy loss in Si estimated in SRIM. Proton energy ranges in the DSSD system are presented in Sec. 3.3.7.

Microball calibration was done by matching the energy spectra of identified protons to energy spectra simulated in PACE2 for the fusion-evaporation reaction of exp1582 for each ring of the Microball detector array. The PACE2 energy spectra took into account different Ta absorber foils place in front of Microball detector elements.

Early on in the analysis stage time alignment of all channels of Microball and DSSD detectors was done. The correlations between different Si channels and Gammasphere, which was the main triggering system, is shown in Fig. 3.7 (a). Later in the analysis, it is important to choose good timing coincidences of Ge detectors and Si and CsI ones to have good particle and γ-ray correlations.

3.3.4 Internal DSSD correlations

The DSSD data analysis started by combining good hits from the p-side and n-side of the same detector to create so-called pixels. These pixels are then employed for particle identification in the subsequent analysis. Thus it is important to carefully select sub-events that form pixels to have cleaner data with reduced random coincidences.

To create a single pixel, a DSSD event should include at least one hit from the p-side (sector) and at least one hit from the n-side (ring). However, there are possibilities of having more than one hit on either or both sides, leading to various combinations, which makes the assignment of a pixel a non-trivial task. Therefore, in total, four stages of pixel creation were implemented:

1. The first round intended to select the majority of good hits, i.e., those

that fulfill a requirement of 50 ns internal time difference between a p- and n-side hit, as well as the energy ratio of the two hits being within a $R = E_p/E_n = [0.96, 1.04]$ window. The energy ratio between the sides of the two DSSD detectors is shown in Fig. 3.7(b). The selection resulted in about 85% and 70% of all pixels assigned for DSSD1 and DSSD2, respectively.

2. In the second round, an addback procedure was implemented for the remaining hits as follows: if two adjacent strips had hits within the appropriate time window, their energies were added together and stored as one hit in the sector/ring which initially had the larger energy. After this, the same check as in the first stage of pixel creation was applied to assign pixels.

3. The third case of the pixel creation procedure was applied for those remaining events that included hits in two sectors and one ring, or two rings and one sector. If the timing and energy requirements were fulfilled, two pixel numbers were assigned to these hits. This involved either storing the same ring number with two sectors, or using the same sector for two rings, respectively.

4. The fourth stage of pixel creation included a special recovery for DSSD2. At the end of exp1582, an adjustment of Si detectors electronics resulted in the partial loss of DSSD2 ring events, while sector signals were recorded regularly. A special recovery procedure for such events was implemented. For details, the reader is referred to Appendix B.3.

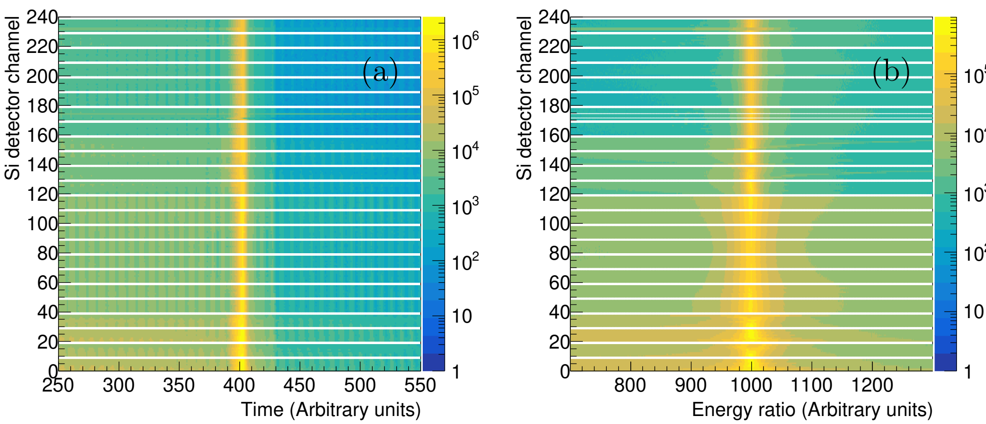

Figure 3.7: (a) Aligned timing signals of all Si channels from both DSSD detectors. The x-axis represents the time difference between DSSD channels and Gammasphere, which was the main triggering system. (b) Energy ratio of hits detected in p- and n-sides of the DSSD detectors.

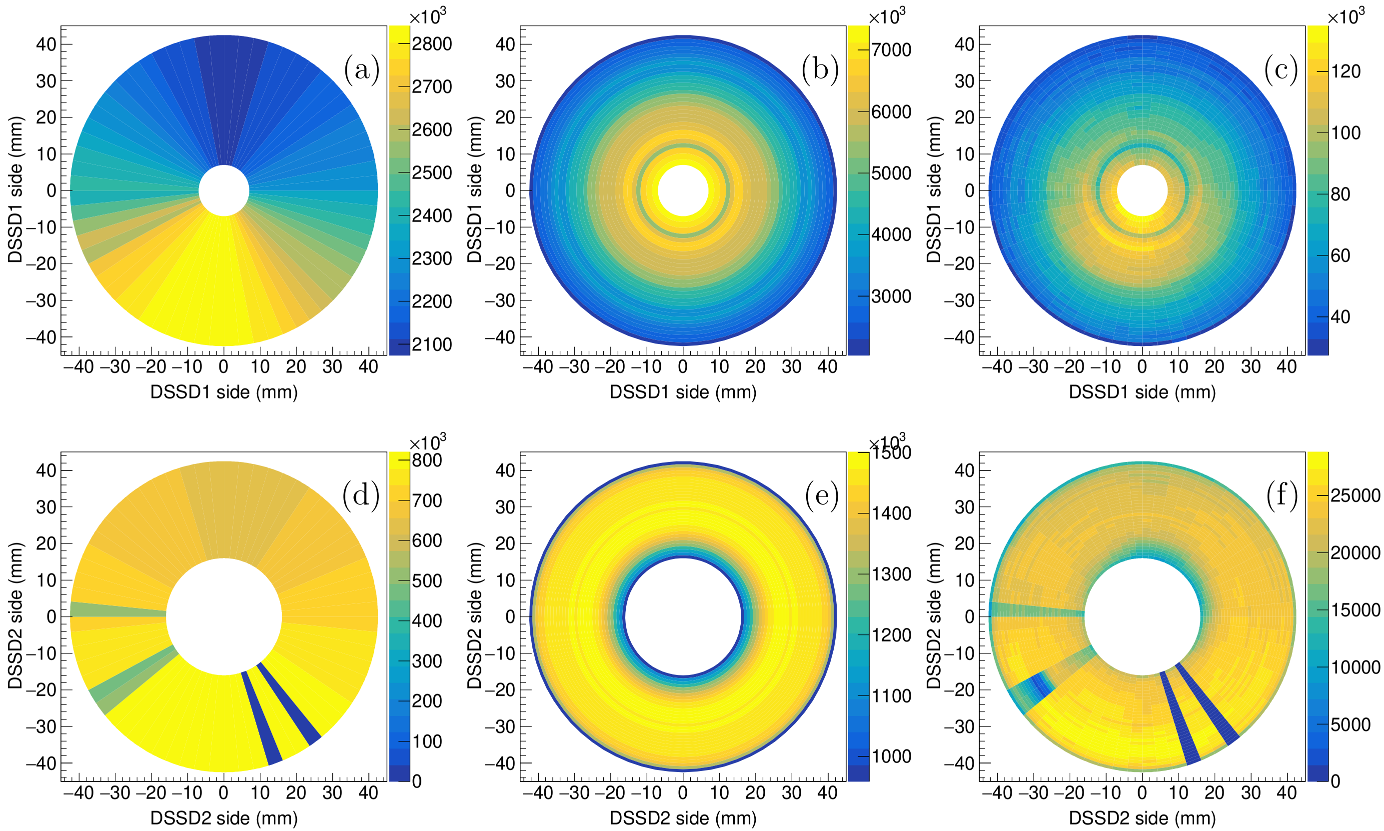

Figure 3.8: Hit patterns of CD-type DSSD1 and DSSD2 detectors for a sample subset of exp1582. Panels (a) and (b), as well as (d) and (e), show the hit patterns of p- and n-sides of DSSD1 and DSSD2, respectively. Combined hit patterns of the two sides of the detectors resulted in 2048 pixels used as histogram bins [panels (c) and (f)].

Hit patterns of the CD-DSSD detectors for a selected subset of exp1582 are presented in Fig. 3.8. Panels (a)-(c) and (d)-(f) showcase the result of combining good hits from p-side with n-side of the detectors into respective pixelated hit patterns for DSSD1 and DSSD2 respectively.

The hit patterns of 64 sectors of DSSD1 and DSSD2 representing p-sides of the detectors are displayed in panels Fig. 3.8(a) and (d) respectively, while panels (b) and (e) show hits in the 32 rings of the n-sides of the detectors. Note that the hit patterns are constructed to follow the geometries of the detectors described in Sec. 3.3.1, meaning that the scale is preserved and corresponds to active areas of the DSSD detectors. The division of the histograms into bins follows closely the actual strips of the detectors, including different sizes of n-side strips for DSSD1. This allows to correlate changes in the DSSDs hit patterns with real changes in the experimental conditions, for example, changes in beam position between runs. Starting with the p-side hit pattern of DSSD1 [Fig. 3.8 panel (a)], a higher number of counts in the lower sectors indicates that the beam position was slightly off-center for this subset of data. Furthermore, the first 14 rings of the DSSD1 register the majority of the charged-particle hits as seen in panel (b). This is as expected from the Geant4 simulations and can be explained by the fusion-evaporation reaction kinematics. Visible lower statistics in ring 4 can be explained by a higher energy threshold set during data acquisition. Finally, combining hits from p- and n- sides according to the procedure described above results in the pixelated hit pattern of DSSD1 shown in panel (c).

Two p-side strips in DSSD2 were disabled during the experimental run, as they were proven noisy during testings of the detector as part of the preparation for the experimental campaign. This is noticeable in the DSSD2 sector hit pattern displayed in panel (d). Three other strips show a lower number of counts, most likely due to higher energy thresholds during the campaign. It is also worth noting, that the inner rings of DSSD2 [panel (e)] have a lower number of counts which could be linked to the charged particles' kinematics as well as possible effects of Ta absorbers placed inside the holes of the DSSD detectors. Lastly, pixel creation for DSSD2 results in the hit pattern presented in panel (f).

3.3.5 DSSD1 - DSSD2 correlations

After sorting the events detected by both the Si detectors and identifying the pixels corresponding to valid hits, it is possible to analyze the correlations between DSSD1 and DSSD2. The promised features of the setup such as particle tracking capabilities and beam-spot estimation were evaluated and are described below.

Particle tracking

Charged-particle tracking capabilities of the DSSD1 - DSSD2 system are illustrated in Fig. 3.9. While forward tracking of the system is shown in Paper III, Fig. 3.9 demonstrates backward tracking: selecting a pixel in DSSD2 reveals which pixels in DSSD1 protons passed through. The correlations between DSSD1 and DSSD2 are considered valid, as coincident pixel hits in DSSD1 align with the expected θ and ϕ angles from the fusion-evaporation reaction kinematics. This, in turn, is also used to set a limit on the range of meaningful θ and ϕ for particle identification through the ΔE-E telescope method.

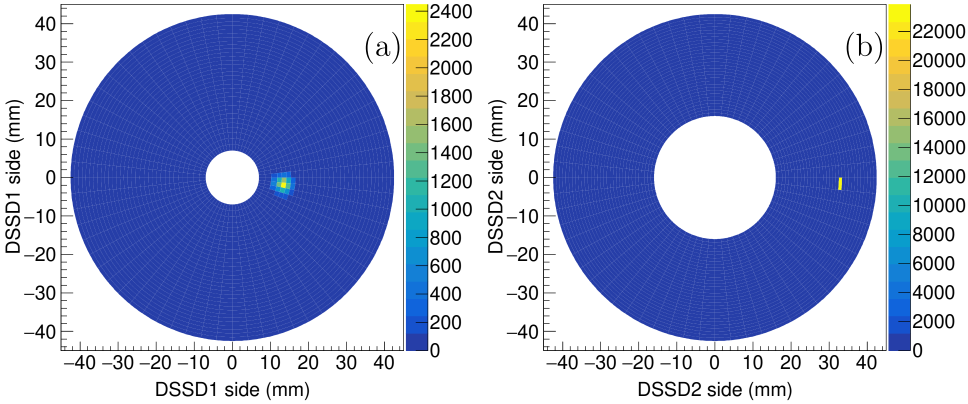

Figure 3.9: Particle tracking capabilities of the CD-DSSDs detector system. Backward tracking is displayed by showing a particle passing through a selected pixel in DSSD2 (b) and the correlated region in DSSD1 (a) that it passed through.

Beam-spot estimation

Since particle tracking capabilities of the CD-DSSD detectors system were established, it is possible to estimate the beam-spot position based on particle tracks in the Si detectors. This is a novel feature when it comes to experimental nuclear spectroscopy setups viable only due to the particular DSSD system's high granularity which enables sufficiently precise particle tracking to accurately estimate the beam spot along an experiment.

The beam-spot position is computed on an event-by-event basis for each proton identified in the DSSD detector system. The proton vector is computed in three dimensions based on Cartesian coordinates of pixels that were hit. The beam-spot X and Y coordinates are calculated for the vector crossing the Z-plane at

0 mm, i.e., the target position. For an example of beam coordinates calculated for a subset of exp1582, see Fig. 4 in Paper III.

Beam-spot offsets computed for each subset of exp1582 were grouped into three pairs which coincides with beam tuning during the experiment. The offsets, ranging from 0.1 to 1.2 mm, were significant enough to be included in the analysis, being on the order of the physical size of an average pixel. Thus, new θ' and ϕ' angles were computed for DSSD's pixels with respect to the origin of the new beam coordinates. These corrected angles were assigned to particles identified with the DSSDs for later use in recoil vector calculations and proton spectroscopy.

3.3.6 Particle identification

Proper particle identification is essential not only for correct evaporation channel selection, but also for reducing background levels while searching for prompt protons of interest in the campaign. The identification of charged particles using the DSSD and Microball array is done in two different ways. The two DSSDs act as telescope detectors so that particle selection is done by looking at the energy deposition of particles in the detection medium. For Microball signals, a pulse-shape discrimination technique is employed to distinguish among different charged particles. Both methods, as well as the combined Si and Microball detector analysis, are presented below.

Si detectors

Using telescope detectors, such as the two CD-DSSDs in question, allows for the separation of charged particles based on their energy loss in the detector material.

Plotting energies deposited in DSSD1, the ΔE detector, versus energy deposited in DSSD2, the E detector, one can experimentally distinguish between different charged particles as presented in Fig. 3.10. Since protons and α particles have significant mass and charge differences, clear separation was expected. Using the advantage of the Si detectors' geometry and restricting their θ and ϕ correlations, allows for significant background reduction in the ΔE-E spectrum. The effects of the inclusion of angle correlations are evident when comparing panels (a) and (b) of Fig. 3.10. The background level between protons and α particles in the spectrum is negligible and clear separation was achieved. Low background in the ΔE-E spectrum in turn also revealed that the setup is sensitive to deuterons, i.e.,

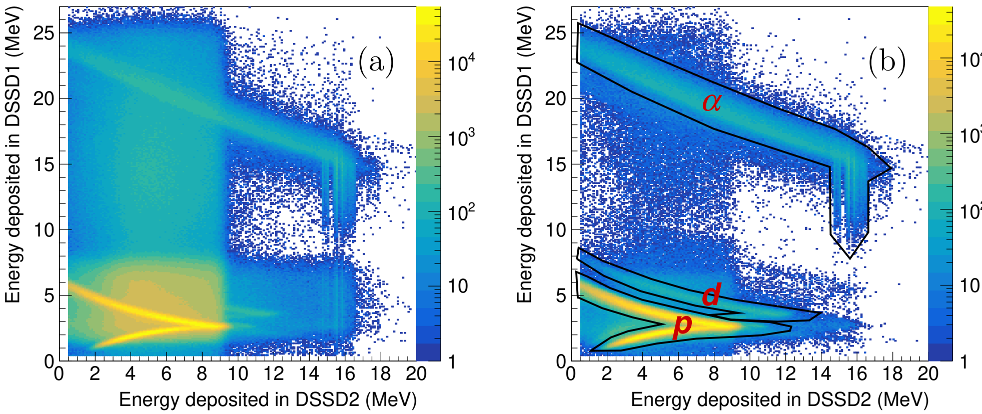

Figure 3.10: Energy depositions of charged particles (protons, deuterons, and α particles) in the ΔE (DSSD1) and E (DSSD2) detectors without (a) and including (b) θ and ϕ correlations between the detectors.

the thickness and geometry of the setup allow for separation between protons and deuterons, although this was not originally anticipated.

Further analysis revealed that only the first 14 rings of DSSD1 detected deuterons given the fusion-evaporation reaction kinematics. Experimental data selected for a single DSSD1 ring is displayed in Fig. 3.11(a). Therefore, for the inner rings of DSSD1, discrimination between protons and deuterons was done ring-by-ring. This approach helped to reduce the proton and deuteron line broadening, caused by the radial change in Ta absorber foil thickness in front of DSSD1, as well as the varying effective thicknesses in DSSD1 itself.

Si detectors with Microball

Since Microball ring 3 (R3) and ring 2 (R2) are placed directly behind DSSD1 and DSSD2, respectively (see Fig. 3.5), one can use the same telescope technique for particle separation based on their energy deposition with the DSSD acting as ΔE and a Microball crystal acting as E detector (Fig. 3.12).

A ΔE-E spectrum plotted for DSSD1 and MB R3 correlations is displayed in Fig. 3.12 (a). The histogram enables the selection of events where a proton passed through DSSD1 in the MB detectors of R3. Note that α-particles are stopped latest by the absorbers placed in front of the MB detectors.

It is possible to differentiate between higher energy protons and deuterons that overlap in the DSSD1-DSSD2 spectra by analyzing the DSSD2 and Microball

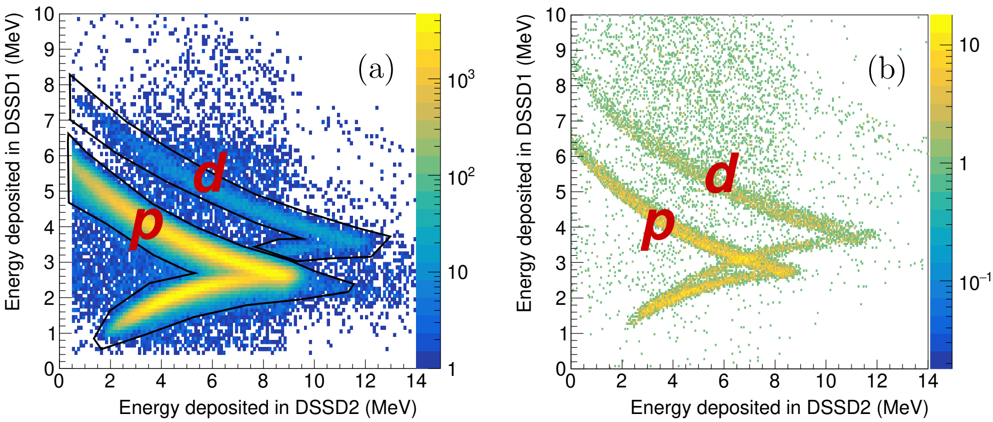

Figure 3.11: (a) ΔE-E spectrum plotted selection a single DSSD1 ring for a selected subset of experimental data from exp1582. (b) ΔE-E spectrum resulting from Geant4 simulations of protons and deuterons irradiating the Si detectors. p and d red text marks selected particle regions, protons and deuterons respectively.

R2 correlations. In panel (b) of Fig. 3.12, a distinct energy separation between the two particle types is shown, which allows for the recovery of almost all higher energy deuteron statistics, except for the two missing MB detectors from R2.

DSSD1

Finally, after the analysis of correlations in the DSSD1-DSSD2 detector system or individual Si detectors with rings in MB, the remaining events in DSSD1 were analyzed. Those events correspond to the charged particles being stopped in DSSD1. Proton events were discriminated from α based on their energy deposition in the Si detector alone.

Microball

Proton-α particle separation in the remaining rings of the Microball detector was done through pulse-shape discrimination. Digitized signals from the CsI(Tl) scintillator detectors were recorded for the first time during the experimental campaign. Two methods for pulse-shape discrimination, the classic charge-comparison method, and the cosine similarity method were implemented by Linus Persson in the frame of his bachelor's project [61]. The latter method led to up to 20% improvement in separation for certain detector elements. For further details, see Ref. [61].

3.3.7 Energy corrections

Once the charged-particle type has been identified, particle-dependent energy corrections can be implemented for particles identified in the DSSD1-DSSD2 system of detectors. Since the majority of protons and deuterons do not deposit all of their energy in the first Si detector, it means that the full energy of the particle has to be determined. In addition to that, the presence of Ta absorber foils placed in front of the first Si detector needs to be accounted for.

Fig. 3.13 relates proton and deuteron energies to thicknesses of the Si detectors [panel (a)] and Ta absorbers [panel (b)]. The minimal energy required for a proton and a deuteron to pass through DSSD1, i.e., 310 μm of Si, is about 6 and 8 MeV, respectively. The combined system of Si detectors can stop protons and deuterons with energies up to about 11 and 14 MeV. Particle energies beyond would not be fully registered. Nevertheless, the full energy of the particle can be reconstructed solely based on the DSSD1 signal as described below. On the other hand, Fig. 3.13(b) shows minimal energies for protons to pass through different Ta absorbers (R_{Ta1} - R_{Ta5}) into the Si detectors. This also signifies that protons detected in Si detectors could have previously lost up to 5 MeV in energy due to the presence of absorbers. This is accounted for ^{61}Ga prompt-proton candidates as described in Sec. 4.2.

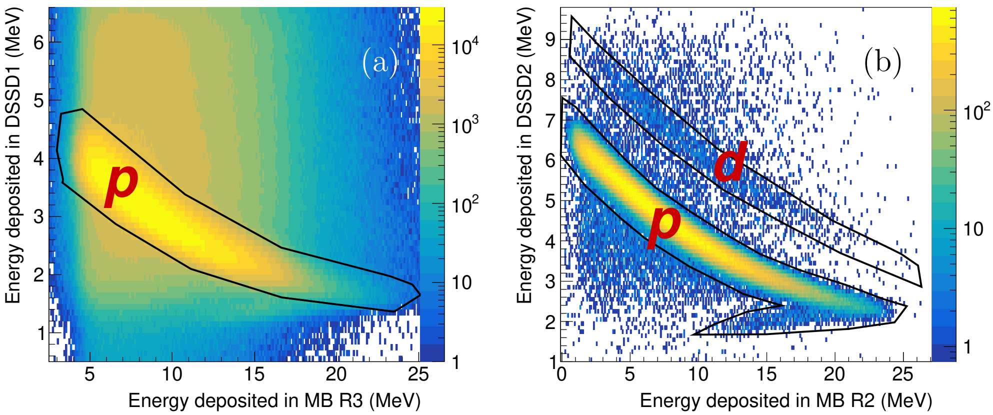

Figure 3.12: (a) DSSD1 - MB ring 3 ΔEE spectrum for charged particle discrimination. (b) DSSD2 - MB ring 2 ΔE-E spectrum used for distinguishing protons and deuterons.

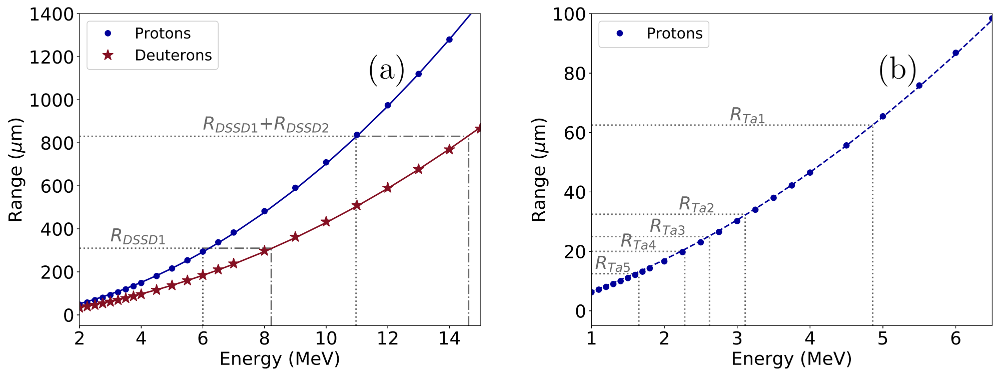

Figure 3.13: (a) Range of protons and deuterons in Si material calculated using SRIM [62]. Gray lines indicate the thicknesses of DSSD1 and DSSD1+DSSD2 detectors and the minimal energy needed for protons (dotted line) and deuterons (dotted dashed line) to pass through the thickness. (b) Range of protons in the Ta absorber material. Gray lines indicate different absorber thicknesses placed in front of DSSD1 and the minimal energy of protons needed to pass through the material.

Detector punchthrough

As previously mentioned, for high kinetic energies of particles, the combined thickness of about 830 μm of Si material is not sufficient for full-energy detection. As a consequence of this, in the ΔE-E spectrum presented in Fig. 3.10, the back-bending behavior is observed for protons and deuterons starting with $E_p \approx$ 9 MeV and $E_d \approx$ 13 MeV and towards lower energies detected in DSSD2. It means that the high-energy particles left the E detector with some remaining energy. The phenomenon is called punchtrough and can be corrected by using the energy deposited in the ΔE detector. The following relation applies:

$$E_{full} = E_{dE} + E_{rem.}, \tag{3.1}$$

together with the relation of the ranges of particles,

$$R_{full} = R_{dE} + R_{rem.}. \tag{3.2}$$

From the system of the equations, as shown in Refs. [63, 64], one can derive the full energy as

$$E_{full} = \frac{aE_{dE}^2 - E_{dE} + th_{dE,\theta}}{2aE_{dE}}, \tag{3.3}$$

where the a and b coefficients are obtained from fitting the range of particles in matter shown in Fig. 3.13(a). The value $th_{dE,\theta}$ is the effective thickness of the material relative to the beam axis at angle θ.

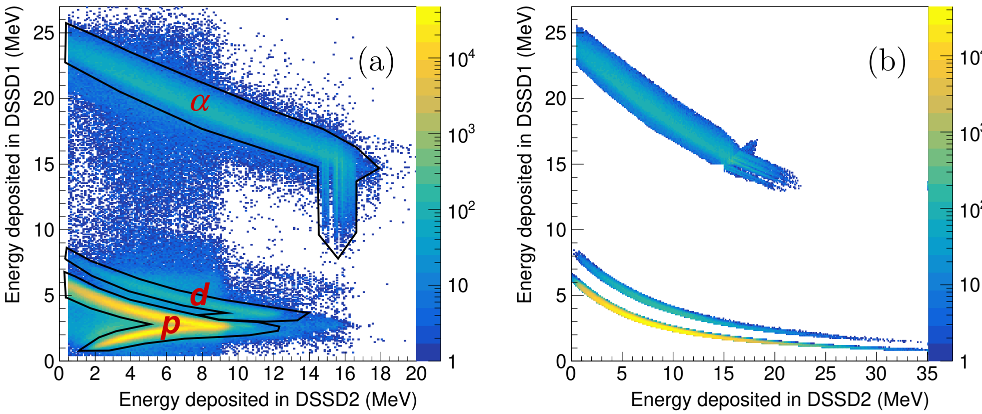

Figure 3.14: CD-DSSDs' ΔE-E spectra showing proton and deuteron energies before (a) and after (b) correction for the punchthrough effect.

Two sets of parameters are used in order to correct both protons and deuterons for the punchthrough effect. Note that α energies do not need to be corrected since they are fully stopped in the DSSD1-DSSD2 system of detectors. The result of the correction is depicted in Fig. 3.14. The resulting proton and deuteron lines are slightly thinner than the original energies in the ΔE-E spectrum. This is a result of using only the first Si for the energy estimation. Another thing worth noticing is the correction of the part of saturated DSSD1 signals for α particles.

3.4 Full experiment analysis

Once the charged-particle detectors analysis has been completed there are two additional considerations before diving into prompt proton search. First, in thin target experiments, the recoil is not fully stopped, necessitating the correction of γ-rays and prompt protons for the Doppler effect. To achieve this, the original recoil vector must be computed based on the vectors of all evaporated particles, including neutrons. Neutron momenta vectors are determined using the neutron time-of-flight method, as described in Sec. 3.4.1. The kinematic correction procedure is detailed in Sec. 3.4.2. Second, when searching for lower probability events, various signal-to-background improvement techniques must be employed. These techniques are introduced in Sec. 3.4.3.

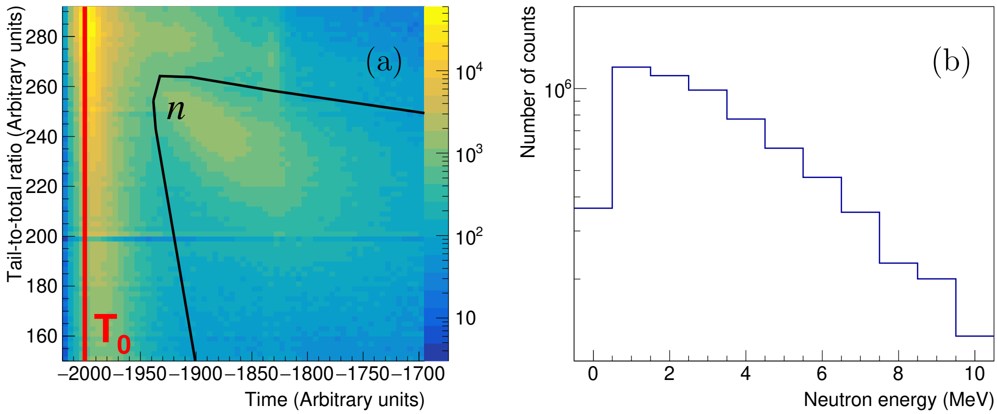

Figure 3.15: (a) Tail-to-total ratio plotted versus time for a typical Neutron Shell detector allowing to distinguish between neutrons (black outline) and γ rays (around red line). The red line marked with T_0 marks the reference time of the prompt γ flash used for the time of flight calculations (see details in text). (b) Neutron energy spectrum estimated based on the neutron time-of-flight method for a sample subset from exp1582.

3.4.1 Neutron time-of-flight

For each identified neutron subevent, the neutron energy can be calculated based on the time-of-flight method. For neutrons with less than $\approx$ 10 MeV energy, the neutron time-of-flight method can be used for computing its kinetic energies according to a simple classical energy formula:

$$E_{k_n} = \frac{1}{2} m_n \frac{D^2}{T_n^2 c^2}, \tag{3.4}$$

where E_{k_n} is the kinetic energy of neutron, m_n is the neutron mass, D is the average distance the neutron travelled, T_n is the neutron time-of-flight, and, c is the speed of light. For the experimental campaign, $D = 40$ cm is the distance between the target and the center of the neutron-detector elements. Fig. 3.15(a) shows the tail-to-total ratio plotted against time for hits registered in a single neutron detector allowing us to distinguish between neutron hits (black outline) and prompt γ hits (red line). Since γ rays travel at the speed of light, T_n of neutrons is calculated relative to the prompt γ flash time signal, T_0. Calculated energies of neutrons based on the time-of-flight method for the sample subset from exp1582 are displayed in Fig. 3.15(b). The computed energy spectrum has the desired peak at around 2 MeV and linear behaviour on a logarithmic scale as expected for evaporated neutrons.

3.4.2 Kinematic correction

Once all energies of all evaporated particles have been determined, they can be taken into account for establishing the kinematics of a recoil nucleus. Since γ rays and prompt protons are emitted from moving recoils, calculating and correcting for Doppler effects is required to obtain their energies in the center-of-mass reference frame. In order to achieve this, a so-called kinematic correction of the energies of γ rays and prompt protons emitted from moving recoils is done on an event-by-event basis. The evaporation of particles during the fusion-evaporation reaction affects the motion of the recoil. Kinematic correction aims at calculating a recoil vector based on the following parameters: (i) the location in the target where the fusion-evaporation reaction takes place, (ii) the kinetic energy of the compound nucleus, (iii) the momenta of evaporated particles calculated from their detected energies and angles, and, (iv) energy loss of the recoil in the remaining thickness of the target layer. Once the recoil vector at the exit of the target is established, a new Doppler correction coefficient is found.

The following relationship applies:

$$\overrightarrow{p}_{recoil} = \overrightarrow{p}_{compound} - \overrightarrow{p}_{total}, \tag{3.5}$$

where $\overrightarrow{p}_{recoil}$ is the momentum of recoiling nucleus, $\overrightarrow{p}_{compound}$ is the momentum of the compound nucleus, and $\overrightarrow{p}_{total}$ is the total momentum of all evaporated particles.

Starting with the original beam momentum, assuming that the beam is perfectly centered:

$$\overrightarrow{p}_{beam} = (0, 0, m_{beam} v_{beam}) \tag{3.6}$$

The fusion-evaporation reaction is assumed to take place mid-target for the reactions of interest and on the target surface for contamination reactions. The energy loss of the beam in the target material has to be taken into account. The calculated energy loss of the beam mid-target is about 6 MeV. Based on the new energy of the beam, the kinetic energy of the compound nucleus can be found as follows:

$$E_{comp} = \frac{m_{beam}}{m_{comp}} E_{beam} \tag{3.7}$$

From the kinetic energy of the compound, its momentum can be found using the simple relationship:

$$p_{comp} = \sqrt{2m_{comp}E_{comp}}, \tag{3.8}$$

The evaporated particles' momentum can be calculated as

$$p_{ev} = \sqrt{2mE_{lab}}, \tag{3.9}$$

where m is the mass of a particle, E_{lab} is its energy measured in the laboratory frame, i.e., deposited or reconstructed. The evaporated particle momentum components can be calculated as follows:

$$p_{ev,x} = p_{ev} sin\theta cos\phi \tag{3.10}$$

$$p_{ev,y} = p_{ev} sin\theta sin\phi \tag{3.11}$$

$$p_{ev,z} = p_{ev} cos\theta \tag{3.12}$$

The total evaporated particles momentum is then simply calculated as:

$$\overrightarrow{p}_{total} = \sum \overrightarrow{p}_{ev} \tag{3.13}$$

Finally,

$$v_{rec} = \sqrt{v_{rec,x}^2 + v_{rec,y}^2 + v_{rec,z}^2} \tag{3.14}$$

The newly calculated velocity of the recoil can be used for an improved event-by-event Doppler and prompt proton corrections.

Doppler correction for γ-ray energies

In the non-relativistic limit, a Doppler shift of the emitted γ occurs according to:

$$E_\gamma = E_{\gamma 0}(1 + \beta cos\theta), \tag{3.15}$$

where $E_{\gamma 0}$ is the center-of-mass γ-ray energy, E_γ is the detected energy of a γ ray, $\beta = \frac{v}{c}$, where v is the velocity of the recoil, c is the speed of light, and θ is the angle between recoil and γ-ray momenta vectors.

For a standard Doppler correction, an average velocity, v_{av}, at the exit of the target is used. However, for an improved Doppler correction, one can use the recoil-specific velocity with the applied kinematic correction to find a new β_{rec}.

In addition to that, $cos\theta$ has to be calculated for the recoil and respective detector element in which a γ ray was detected.

The γ-rays stemming from recoils from evaporation channels involving α-particles are more strongly affected by Doppler shift in comparison to the evaporation of lighter particles. For ^{58}Ni recoils, the $\alpha 2p$ evaporation channel of ^{64}Ge compound, employing the kinematic correction resulted in a reduced FWHM from 16 keV to 11 keV for the peak of the 1005-keV transition ^{58}Ni. This corresponds to a relative improvement of 32% for the selected evaporation channel. Fig. 3.16 illustrates the impact of the applied correction on ^{58}Ni recoils for 2000 keV $\leq E_\gamma \leq$ 2850 keV. Notably, the correction leads to the clear separation of the 2139-keV and 2166-keV peaks, which were previously merged.

Alternatively, for recoils detected with the FMA, $v_x = v_y \approx 0$, and v_z-variations can be estimated from the energy losses in the IC.

3.4.3 Signal-to-background improvement

Information on total γ-ray multiplicity, K, and total energy of γ rays registered, H, as well as total evaporated particle energy, P, could be used for further distinguishing between different reaction channels leading to background reduction for a reaction channel of interest.

To be able to measure K and H, the heavimet collimators, usually used to protect the Gammasphere anti-Compton shields from direct γ radiation, were

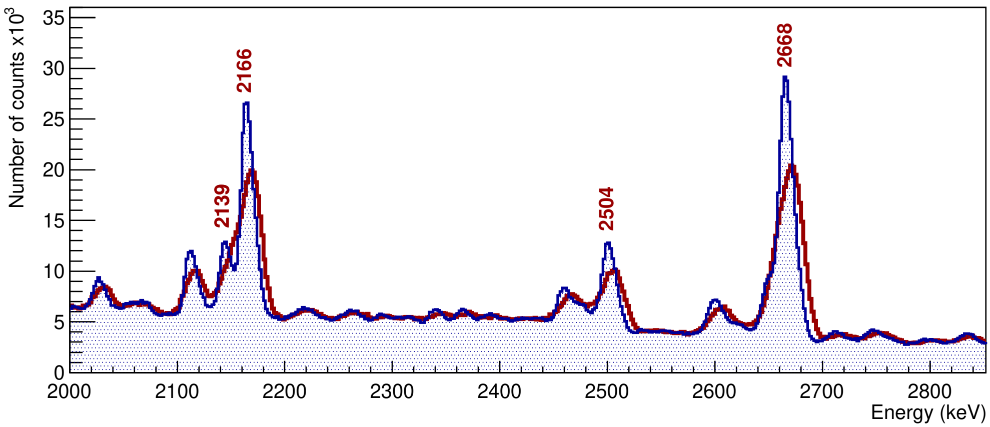

Figure 3.16: The γ energy spectrum of ^{58}Ni from $\alpha 2p$ evaporation channel before (red) and after (blue) kinematic correction shown for 2000 keV $\leq E_\gamma \leq$ 2850 keV. The energies of several γ-ray transitions known to belong to ^{58}Ni are indicated in red text.

removed. Those parameters can be used for the experimental campaign since the experiments of interest have low γ-ray multiplicity.

The total γ-ray multiplicity, K, was computed on event-by-event basis as follows:

$$K = N_{GS} + N_{BGO} + N_{GS+BGO} + N_{NS}, \tag{3.16}$$

where N_{GS} and N_{BGO} are the number of γ rays registered only in Gammasphere and only in BGOs respectively, while N_{GS+BGO} denotes the number of γ rays scattered from Gammasphere into BGO shields; finally, N_{NS} is the number of γ rays counted in the Neutron Shell. Similarly to K, H is computed by counting the energies of each γ-ray from the three detector systems.

The energy of particles, P, is computed by summing energies of all identified evaporated particles in DSSDs, Microball, and Neutron Shell detector arrays.

HK and HP histograms, namely plotting the total number of γ rays, K, vs. the total γ energy, H, and total energy of γ rays, K, vs. total energy of the particles, P are used for improving reaction-channel selection. Fig. 3.17 shows an example with ^{61}Zn and ^{49}Cr nuclei, both selected by requiring events with two protons and one neutron in the dataset. The nuclei come from $2pn$ evaporation channel, however, ^{61}Zn comes from the main compound nucleus for exp1582, ^{64}Ge, while ^{49}Cr is created as a result of contamination reaction of the beam with carbon leading to a ^{52}Fe compound (see Fig. 3.2). The top panels in Fig. 3.17 displaying HP histograms show noticeable separation, where majority of ^{49}Cr is detected with total γ-ray energy per event $H(^{49}\mathrm{Cr}) \leq 7$ MeV. This requirement is then used for plotting HK histograms for the nuclei. The histograms further confirm the validity of the requirement. In addition to that, adding $K(^{49}\mathrm{Cr}) \leq 4$ also helps to further separate the two residual nuclei. Thus, H, K, and P parameters have proven useful for improving reaction-channel selection on an event-by-event basis, especially if there is no recoil information available.

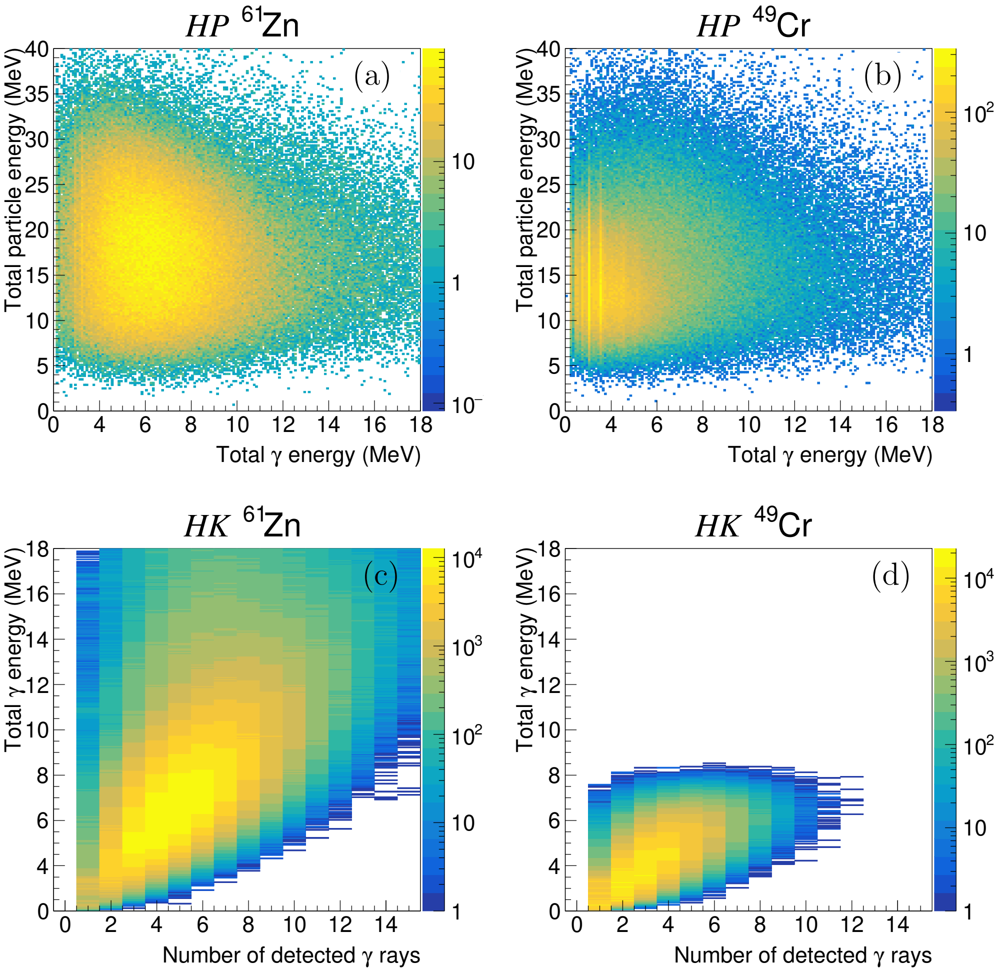

Figure 3.17: Top panels show HP-histograms, i.e., total particle energy, P, plotted as a function of total γ energy, H, while bottom panels display HK-histograms, H as a function of total number of γ rays, K, for the $2pn$ reaction channels. HP-histograms for ^{61}Zn and ^{49}Cr are presented in (a) and (b), respectively. HK-histograms for the same recoils are shown in (c) and (d). Note that HK-histograms are filled taking into account discrimination using HP-histograms. For further details see text.

Chapter 4

Proton emission in ^{61}Ga

The second experiment of the ANL2020 campaign aimed to discover prompt proton emission from the deexcitation of the excited $9/2^+$ state in ^{61}Ga nucleus [45] into the ground state of ^{60}Zn [65]. This $9/2^+$ state is expected to represent the proton $\pi g_{9/2}$ single-particle state mirroring the known neutron $\nu g_{9/2}$ single particle state in ^{61}Zn [65, 66, 67]. Identification of this proton-state with high precision through means of in-beam particle-γ spectroscopy would allow to asses mirror-energy differences of the ^{61}Ga and ^{61}Zn pair to study isospin-symmetry breaking in the upper fp shell.

This chapter focuses on details of the analysis behind the experimental identification of the prompt proton leading to Paper IV. The chapter describes the selection criteria of ^{61}Ga prompt proton candidates in Sec. 4.1 followed by energy corrections applied alongside detailed Geant4 simulations done to verify each of the energy-correction steps presented in Sec. 4.2. Experimental results are presented in Sec. 4.3 including other proton lines tentatively assigned to ^{61}Zn and not used for publication due to the lack of sufficient statistics.

4.1 Conditions for prompt protons selection

Since the vast majority of protons identified during the experiment arise from evaporation after compound nuclei formation, strict proton candidate selection conditions have to be applied to improve the signal-to-background ratio. First, proper evaporation channel selection is very important. ^{61}Ga represents the $p2n$ evaporation channel of the ^{64}Ge compound. Proton emission from ^{61}Ga results in ^{60}Zn. Hence, for the analysis, the following basic conditions were imposed for the channel selection:

- mass $A = 60$ recoils detected in the FMA, to pick among others events with ^{60}Zn recoils;
- the number of protons, N_p, should be 1 or 2, i.e., the proton of interest and possibly, the second, evaporated proton from the ^{64}Ge compound.

To have a cleaner channel selection, one could additionally include at least one neutron in the event requirement, since ^{61}Ga is a neutron-evaporation channel. However, due to the issues with the neutron-detector DAQ detailed in Sec. 3.2, the remaining statistics obtained from including any neutron requirement is usually too small for detailed analysis, and in particular when combined with FMA data. Furthermore, Z separation coming from the IC turned out to be insufficient as a channel-selection requirement as well. Instead, options for additional channel "clean-up" are considered using HK and HP histograms (see Sec. 3.4.3).

Once the channel selection is applied, additional criteria are taken into consideration for identified protons. For more accurate energy determination of the identified protons, only those detected with DSSD1 are considered for further analysis (see Sec. 3.3.1). The protons of interest gain about 3-4 MeV kinematic boost upon being released from ^{61}Ga in-flight. Thus, given the total laboratory frame energy of around 5-6 MeV, only those protons identified and stopped in DSSD1 are considered potential candidates. For these proton candidates, further energy corrections and transformations are applied to obtain their center-of-mass energies. These corrections are described in the following.

4.2 Proton energy corrections

According to the suggested location of the $9/2^+$ level [45], the expected proton energy should be about $E_{p,c.o.m.} = 2.0$ MeV in the center of the mass frame. However, in the laboratory frame, the detected protons have higher energies since they receive additional momentum from the moving ^{61}Ga recoil. Therefore, to identify potential candidates, the laboratory kinetic energies of protons need to be converted into the center-of-mass reference frame.

4.2.1 Correction for absorber foils

Detected proton energies are significantly affected by energy loss in the Ta absorber foils placed in front of DSSD1, as introduced in Sec. 3.3.1. To account for this is non-trivial, and, thus, SRIM [62] is used to estimate the original energy, E'_{lab}. The energy loss correction is applied in several steps for every detected proton:

1. Range in Ta, R_{Ta}: Using the detected proton energy, E_{lab}, its corresponding range in Ta, $R_{Ta}(E_{lab})$, is estimated based on SRIM.

2. Effective thickness, th_{eff} of the Ta foil: The actual thickness of the Ta foil in front of DSSD1 needs to be added. To do this, a table was prepared with the Ta foil thickness corresponding to each DSSD1 ring, th, based on Sec. 3.3.1. th_{eff} is then calculated as

$$th_{eff} = \frac{th}{cos\theta'} \tag{4.1}$$

   where θ' is the angle between the recoil and the detected proton.

3. The total range in Ta foil, $R_{Ta,tot}$, is calculated as:

$$R_{Ta,tot} = R_{Ta}(E_{lab}) + th_{eff}, \tag{4.2}$$

4. Corrected energy, E'_{lab}: Finally, the total range, $R_{Ta,tot}$, is used to find the corresponding energy $E'_{lab}(R_{Ta,tot})$ also by using SRIM.

4.2.2 Center-of-mass frame calculations

The kinematic correction of prompt protons released from nuclear deexcitation can be done similarly to previously described γ-ray corrections (see Sec. 3.4.2). The proton energies in the center-of-mass system are the ones of interest, $E_{p,c.o.m}$. One of the differences, however, is that the prompt particle momentum is not taken into account while calculating v_{rec}, as the prompt particle is assumed to be released after the recoil exits the target.

The energy of a prompt proton in the center-of-mass system, $E_{p,c.o.m}$, can be computed based on its kinetic energy, E_p, related to the recoil energy, and the energy measured in a detector system, E_{lab} [68]:

$$E_{p,c.o.m} = E'_{lab} + E_p - 2\sqrt{E'_{lab}E_p}\cos\theta' \tag{4.3}$$

Similarly, angular proton distributions in the center-of-mass frame, $\theta_{p,c.o.m}$, can be calculated as follows:

$$\theta_{p,c.o.m} = arctan(\frac{sin(\theta')}{cos(\theta') - \sqrt{E_p/E'_{lab}}}) \tag{4.4}$$

4.2.3 Geant4 simulation

The Geant4 model of the DSSD detectors presented in Sec. 4.2.3, was used to verify the impact of the detector geometry, presence of absorbers, and recoil kinematics on the estimation of the energy of proton candidates. The simulation provides a controlled environment, in which Q_p of the protons, and hence E_p, is used as an input. The output of the simulation is energy depositions in the DSSDs pixels, corresponding to the experimental E_{lab}. The same energy correction steps were then applied to the simulated data to obtain E'_{lab} and $E_{p,c.o.m}$ as it was done for experimental data. By working with simulated data, it is possible to estimate the level of uncertainty in proton-energy determination at various stages of corrections given the experimental setup. Specifically, three stages were explored: (i) energy output from DSSD1 with the presence of Ta absorbers, which corresponds to experimental reality before any corrections, (ii) impact of correction for Ta absorbers, helping to verify SHRIM functions used, and (iii) final transformation into center-of-mass frame.

The simulation focused on proton deexcitation of ^{61}Ga. Experimental proton candidate energy spectra are expected to be dominated by the continuous background from evaporated protons with limited statistics in ^{61}Ga discrete prompt proton peak. Thus, the simulation serves as an excellent tool for studying the impact of corrections on the prompt protons specifically, independent of any background. Proton emission was added to the ^{61}Ga decay file with $Q_{p,in}$ = 2.000 MeV. This corresponds to proton energy of $E_{p,in}$ = 1.968 MeV. The kinetic energy of the ^{61}Ga recoil was sampled from a uniform energy distribution $E_{kin}(^{61}\mathrm{Ga})$ = [50 MeV, 56 MeV] based on where in the target the fusion-evaporation reaction takes place. The recoil unit vector of direction was sampled randomly with ϕ and θ reflecting forward kinematics of the recoils and taking into account the opening angle of the FMA to mimic the experimental condition of mass $A = 60$ selection. The energy loss of ^{61}Ga in the remaining target material was taken into account, as proton emission is assumed to take place outside the target material.

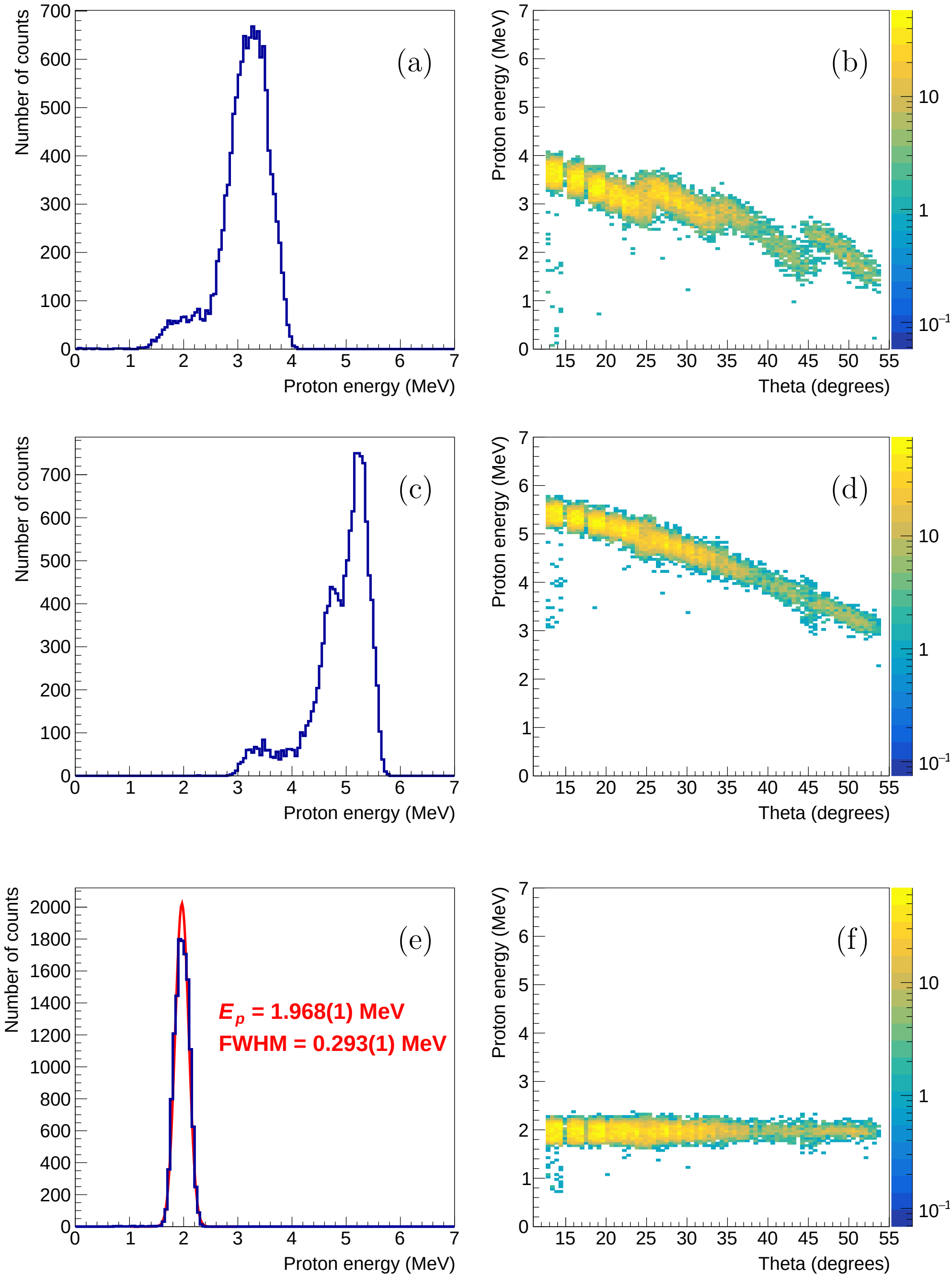

Figure 4.1: Results of Geant4 simulations of ^{61}Ga proton emission with $Q_{p,in}$ = 2.000 MeV. The two spectra in the top row show the proton energy deposition in the first DSSD1 (a) and its dependence on the laboratory angle, θ (b). Correction of simulated events for energy loss in Ta absorbers results in the proton energy distribution shown in (c) together with energy and angular distribution shown in (d). Calculated center-of-mass proton energies based on kinematic correction provides the spectra displayed in panels (e) and (f). See text for details.

The simulated energy spectrum of protons originating from in-flight deexcitation of ^{61}Ga and detected by DSSD1 is depicted in Fig. 4.1(a). Simulated protons gain kinetic energy from the recoil motion, and lose some energy in the Ta absorber (see Fig. 3.6), resulting in a peak with the centroid around 3.2 MeV. The width of the peak is influenced by the presence of four Ta rings in front of DSSD1 as it is visible when plotting proton laboratory energy vs. laboratory angle as shown in Fig. 4.1(b). Reconstructing the energy before the energy loss in the absorber results in an energy shift of about 2 MeV as presented in panel (c). The angle-dependent effect of applying the correction for Ta absorbers is visible in Fig. 4.1(d). Finally, converting the energy to the center-of-mass reference frame removes the dependence on the laboratory detection angle [see panel (f)] and results in a narrow peak with E_p=1.968(1) MeV matching the original energy used as an input, $E_{p,in}$. The FWHM of the simulated peak displayed in Fig. 4.1(e) is 0.293(1) MeV. The result is influenced by both recoil kinematics and the detector geometry as expected according to Ref. [68]. The former accounts for the fact that fusion evaporation can occur at any point within the target, resulting in a wide energy distribution of the emitted protons. The latter pertains to variations in the thickness and size of the DSSD1 pixels, as well as the presence of Ta absorbers with different radial thicknesses.

4.3 Experimental results

The analysis method to find candidates for prompt proton emission includes creating various $E_{p,c.o.m.}$-E_γ correlation matrices for a recoil of interest. For ^{61}Ga proton deexcitation, the conditions described in Sec. 4.1 were applied. In addition, several combinations of various parameters were tested to reduce the background from evaporated protons. The overall background suppression was achieved by selecting total γ multiplicity $K > 3$ as well as requiring prompt timing for γ-proton coincidence.

In the final $E_{p,c.o.m.}$-E_γ matrix, a 1.871(24)-MeV proton was identified in coincidence with a 957.6(5) γ-ray transition. The proton peak plotted on top of the normalized background is shown in Fig. 4.2(a). The proton peak is obtained by requiring a coincidence with the 958 keV γ ray. Panel (b) shows the spectrum after subtraction of the normalized background resulting in 29(8) counts in the proton peak. It is worth noting that the kinematic correction and proton center-of-mass energy reconstruction already include a correction for varying offsets of the position of the beam spot. This capability arises from the two DSSDs acting as the tracking system (see Sec. 3.3.5 and Paper III).

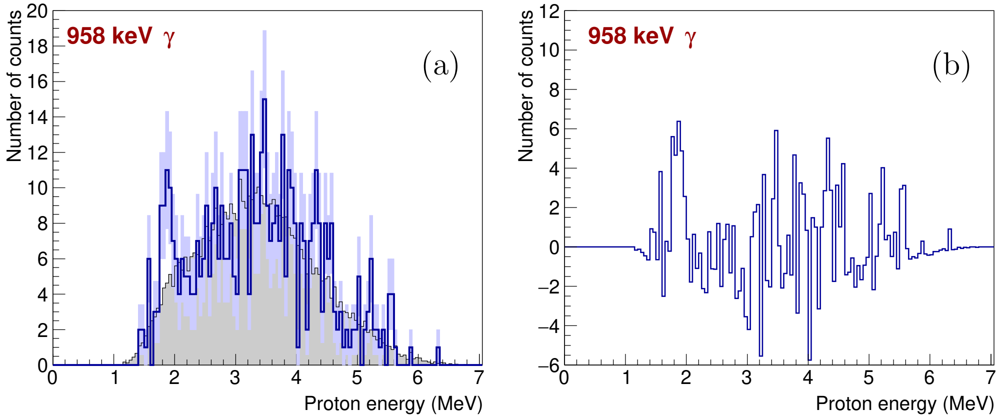

Figure 4.2: Center-of-mass proton energy spectrum in coincidence with a 958-keV γ ray associated with ^{61}Ga deexcitation. The peak is shown in dark blue together with uncertainties in counts (lighter blue shade) plotted on top of the normalized gray background. The background-subtracted proton energy spectrum is shown in panel (b).

4.3.1 958-keV γ coincidence

Looking at the mirror nucleus to ^{61}Ga, ^{61}Zn, a 958-keV γ could be associated with a $13/2^+ \rightarrow 9/2^+$ transition in ^{61}Ga. The energy corresponds to the 937-keV γ ray from $13/2^+ \rightarrow 9/2^+$ in ^{61}Zn [65, 66, 67] taking into account some variations of mirror energy differences. The $9/2^+$ state in ^{61}Ga deexcites by emitting a $g_{9/2}$ proton resulting in the 0^+ ground state of ^{60}Zn. The ground state of ^{60}Zn with respect to ^{61}Ga proton separation energy is at 243(23) keV [43, 69, 70]. For further discussions, see Sec. 4.4 and Paper IV.

To confirm the coincidence between the proton candidate and the 958-keV γ ray, a γ-ray energy spectrum was plotted in coincidence with $1.75 \leq E_{p,c.o.m} \leq 2.05$ MeV. The resulting γ-ray spectrum is shown in Fig. 4.3. First of all, the spectrum confirms a coincidence with the 958-keV γ ray. Furthermore, several γ rays were identified with a few counts on top of the background, namely at 778.6(6), 1006(2), 1039(2), 1188(1), and 1697(2) keV. The origin of those γ rays has to be investigated to aid in constructing a ^{61}Ga level scheme with respect to the anticipated proton-emitting $9/2^+$ state.

4.3.2 Other γ coincidences

Proton energy spectra in coincidence with 778.6(6), 1006(2), 1039(2), 1188(1), and 1697(2) keV are displayed in Fig. 4.4(a)-(e). A possible peak-like structure, or excess of counts, around 2.0 MeV is visible in all those proton energy spectra,

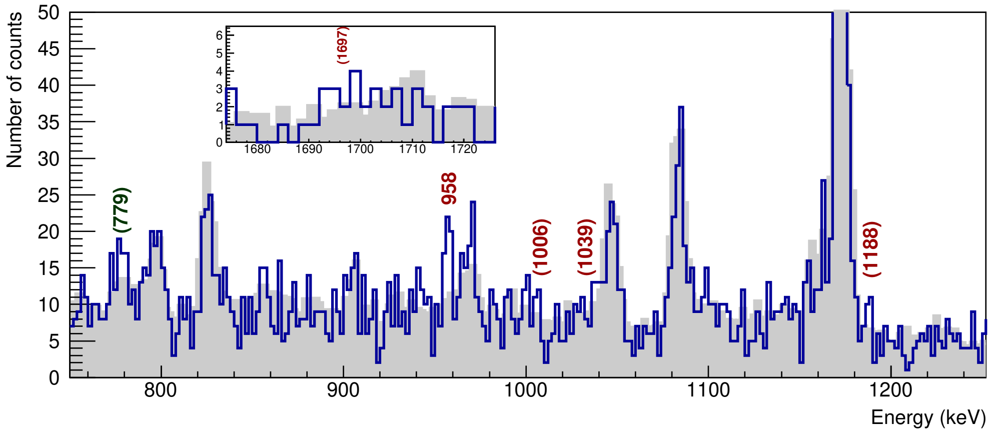

Figure 4.3: γ-ray energy spectrum (dark blue) plotted in coincidence with $1750 \leq E_{p,c.o.m} \leq 2050$ MeV. The background is depicted in gray. Transitions of interest are labeled with their energy in keV. For details see text.

hence the extra counts in the corresponding γ peaks in Fig. 4.3. However, note that some of the aforementioned proton peak-like structures hardly have counts in excess of the uncertainty band and are questionable in terms of compatible experimental peak widths.

Panels (a) and (b) in Fig. 4.4 display proton energies in coincidence with 1039(2) and 1697(2) keV γ rays. Since the $21/2^+ \rightarrow 17/2^+$ and $17/2^+ \rightarrow 13/2^+$ transitions in ^{61}Zn are 1675 and 1079 keV, respectively, one could tentatively assign the newly identified γ transitions as follows: 1697(2) keV as $21/2^+ \rightarrow 17/2^+$ and 1039(2) as $17/2^+ \rightarrow 13/2^+$ transitions in ^{61}Ga, considering mirror symmetry. Excitation energies of the $21/2^+$ and $17/2^+$ states would be $E_x(21/2^+)$ = 5.844(23) MeV and $E_x(17/2^+)$ = 4.147(23) MeV.

Proton energies in coincidence with 1006(2) and 1188(1) keV γ rays are drawn in panels (c) and (d) in Fig. 4.4. Those γ peaks could be potentially assigned to already known yrast transitions in ^{60}Zn, namely the $2^+ \rightarrow 0^+$ 1003.9(2) keV and $4^+ \rightarrow 2^+$ 1189.2(4) keV [72]. While the identified γ-ray peaks correspond to the tabulated values within the uncertainty, the number of counts and uncertainty in the proton peaks associated with them is too small for an unambiguous assignment. In case those events would be confirmed, it would imply that excited states in ^{60}Zn might be populated by proton deexcitations from higher lying states in ^{61}Ga, e.g. the $21/2^+$ or $17/2^+$ states suggested earlier, to the 4^+, 2^+ states in ^{60}Zn, respectively. Simple calculations could be done to verify whether those transitions are energetically possible. The states in ^{60}Zn are at $E_x(2^+)$ = 1253(38) keV and $E_x(4^+)$ = 2442(38) keV with respect to the ground state of ^{61}Ga. Proton deexcitation from $13/2^+$ in ^{61}Ga to 2^+ in ^{60}Zn would result in

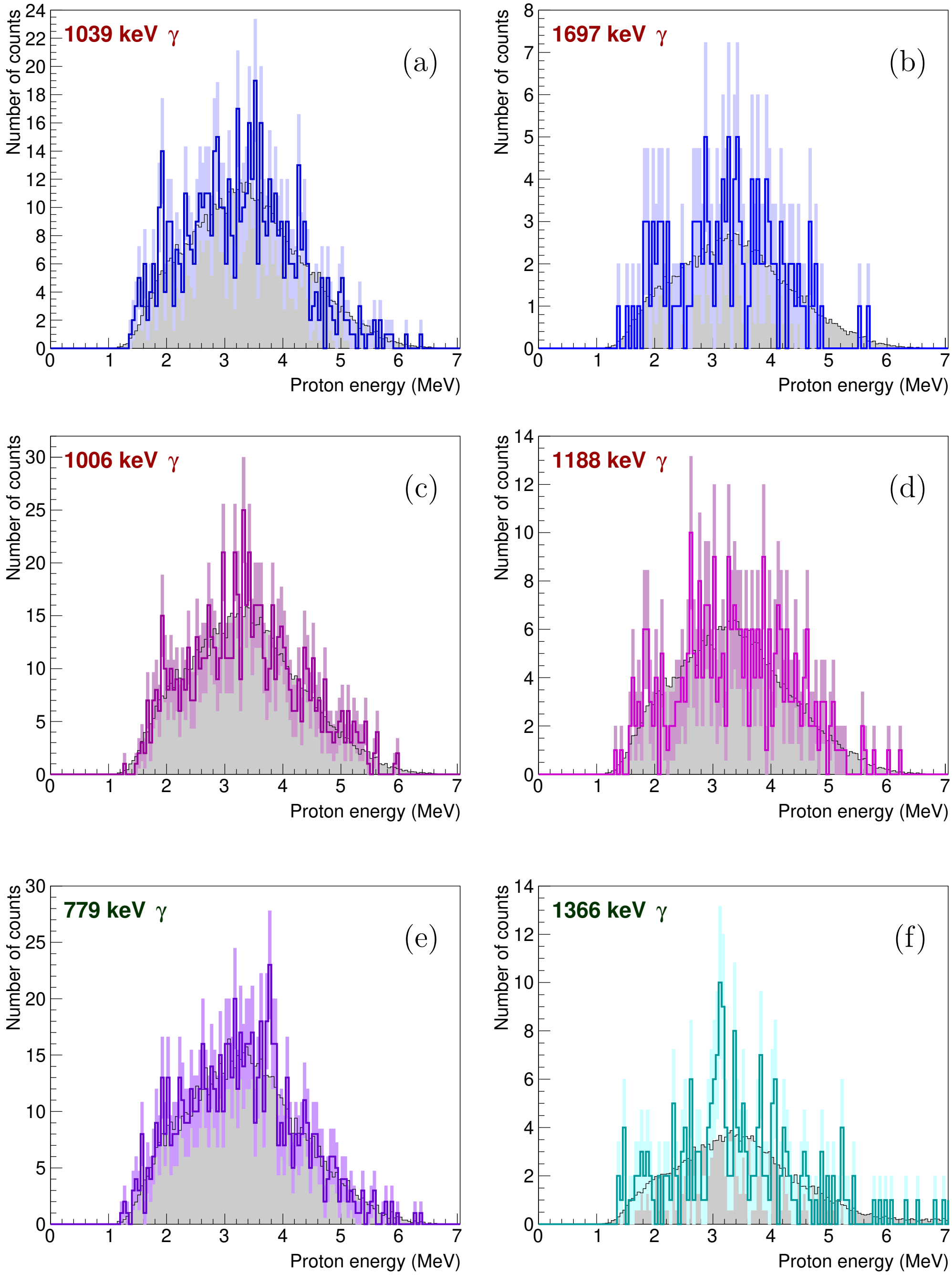

Figure 4.4: Proton energy spectra in coincidence with 778.6(6), 1006(2), 1039(2), 1188(1), 1366(1) and 1697(2) keV γ rays. Proton energies in the center-of-mass frame are selected for A=60 recoils and protons that are detected by only DSSD1. Additional requirements on the number of protons are $1 \leq N_p \leq 2$ for panels (a)-(e), and $N_p \geq 3$ for panel (f). See text for details.

$Q_{p_2} = 1856$ keV and proton energy $E_{p_2} = 1826$ keV. Similarly, $Q_{p_4} = 1706$ keV and $E_{p_4} = 1678$ keV for the case of $17/2^+$ in ^{61}Ga to 4^+ in ^{60}Zn. Since there are very few counts in the proton energy spectra [cf. Fig. 4.4(c) and (d)], and if so, rather at $E_{p,c.o.m.} \approx 2.0$ MeV for the 1006-keV coincidence, there is no evidence of the presence of such protons given the statistics and uncertainties of the present data set.

The newly identified 778.6(6) keV peak cannot be assigned to a proton emission from ^{61}Ga to ^{60}Zn. This calls for further investigation and better control of reaction channel selection.

4.3.3 Influence of N_p parameter

A way of channel selection without including neutron detectors or the IC, is to control the number of protons required, N_p. Since the potential proton emissions should result in $A = 60$ daughters, there is a limited list of candidates. They are summarized in Table 4.1. The number of protons required takes into account the fact that some evaporated protons missed detection. This means that when requiring $1 \leq N_p \leq 2$ to select ^{61}Ga proton emission to ^{60}Zn, the selection could also potentially pick up protons associated with deexcitations from excited states in ^{61}Zn or ^{61}Cu, if those existed. At the same time, choosing $N_p \geq 3$ cannot select any of the ^{61}Ga protons.

Table 4.1: List of evaporation channels (first column) from ^{64}Ge compound nucleus resulting in $A = 61$ recoils (second column). A list of final $A = 60$ nuclei in case excited states in the recoils undergo proton emission is given in the third column. The last column shows the number of protons, N_p, used for different channel selection.

Evaporation channel	Recoil	Final nucleus	N_p
$p2n$	^{61}Ga	^{60}Zn	1-2
$2pn$	^{61}Zn	^{60}Cu	2-3
$3p$	^{61}Cu	^{60}Ni	3-4

The integral of each proton peak as a function of N_p is displayed in Fig. 4.5 for several γ-ray transitions of interest. It is important to note that yields associated with ^{61}Ga and ^{60}Zn [panel (a)] have a significantly reduced number of counts for the selection of 2-3 protons, and 0 counts within uncertainty for $N_p \geq 3$. This strongly suggests that they belong to the correct reaction channel, i.e., proton emission from ^{61}Ga into ^{60}Zn. Panel (b) shows a comparison of proton yields in coincidence with 779 and 1366 keV γ rays vs. the 958-keV selected proton. It is clear that 779- and 1366-keV selected proton peaks have a higher number of counts for 2-3 protons and 3-4 protons, respectively. This implies that, if they

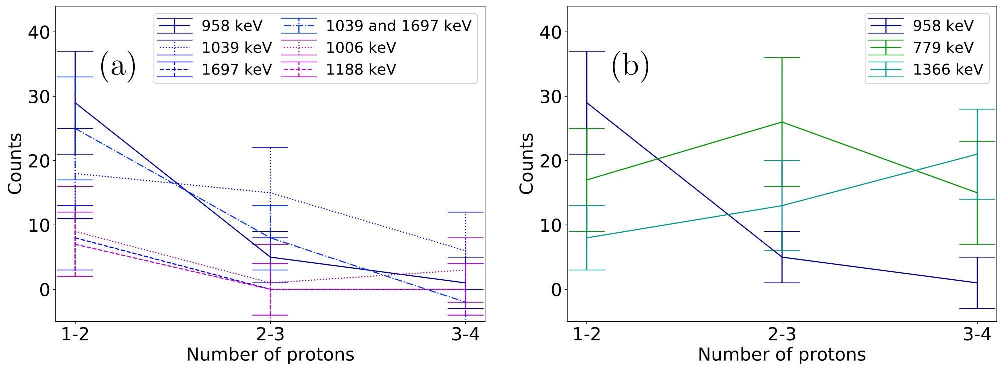

Figure 4.5: Yield of proton energy peaks as a function of number of protons required in the channel selection, denoted as N_p parameter. Panel (a) shows proton peaks in coincidence with γ-ray candidates associated with ^{61}Ga proton emission into ^{60}Zn. Panel (b) repeats the yield in coincidence with the 958-keV γ ray in comparison with yields from two other γ rays, possibly preceding proton emission. For details see text.

exist, they rather have to be associated with proton emission from exited stated in ^{61}Zn or ^{61}Cu (see Sec. 4.4.2).

4.4 Interpretation

4.4.1 ^{61}Ga proton emission

Given the previous arguments, as well as a sufficient level of statistics in the 958 keV- selected proton peak, it can be assigned as the proton candidate from the proposal, i.e., proton emission from the $g_{9/2}$ single-particle state in ^{61}Ga to the 0^+ ground state in ^{60}Zn. It can also be concluded that there is not enough evidence to suggest other proton emissions from higher excited states of ^{61}Ga into the 2^+ or 4^+ excited yrast states in ^{60}Zn.

Even though 1039-keV and 1697-keV selected proton peaks have a relatively low number of counts, those could be added up with 958 keV forming a single proton line. We can suggest a cascade of γ transitions: $21/2^+ \rightarrow 17/2^+$, $17/2^+ \rightarrow 13/2^+$, $13/2^+ \rightarrow 9/2^+$ followed by the proton emission to the ground state of ^{60}Zn. A comparison between the proton energy spectrum in coincidence with 958 keV and the sum of all three γ-ray transitions is shown in the Supplemental Material to Paper IV. The selections give the following proton energies: $E_p = 1.871(24)$ MeV and $E_{p,sum} = 1.897(26)$ MeV. Both energies overlap within the uncertainty, which allows to claim that it is the same peak. The derived FWHM for both cases being 0.18(5) MeV and 0.21(5) MeV are in the same order of magnitude as predicted by the Geant4 simulation [cf. Sec. 4.2.3 and Fig. 4.1(f)]. This confirms that all three transitions are in coincidence with the proton line. This concludes the search for proton emission lines and allows adding the newly found levels to the ^{61}Ga level scheme displayed in Fig. 4.6.

To summarize, Fig. 4.6 shows the assignment of the identified proton and three newly identified γ transitions in ^{61}Ga. The details are presented in Table 4.2. The proton line at $E_p = 1.876(24)$ MeV is associated with the decay from the proton $\pi g_{9/2}$ single-particle state in ^{61}Ga into the ground state of ^{60}Zn, based on the $A = 60$ requirement and because there were no identified coincidences with yrast transitions in ^{60}Zn. The spins and parities of the states connected by the 958-, 1039-, and 1697-keV γ-ray transitions were tentatively assigned based on mirror symmetry with ^{61}Zn, which has a 937-, 1079-, and 1675-keV cascade feeding into its neutron $\nu g_{9/2}$ single-particle state [66, 67].

Finally, mirror energy differences between the newly identified states in ^{61}Ga and their counterparts in ^{61}Zn can be computed and compared with theoretical predictions. The results are presented in Paper IV, with details of the shell-model calculations provided in the Supplemental Material to Paper IV. For background on the shell model and additional discussion of the results, see Chapter 5.

Table 4.2: Newly identified excited states ^{61}Ga nucleus with respect to its ground state. Experimentally measured energies of γ rays and the proton line are stated in columns E_γ in keV and E_p in MeV, respectively. Energy of excited states associated with transitions is indicated in the first column, together with initial spin I_i and final I_s state spins. Spin assignment of tentative γ transitions is given is square brackets. Additional information on the proton peak is given in columns FWHM and Q_p.

E_x (MeV)	I_i	I_f	E_γ (keV)	E_p (MeV)	Counts	FWHM (MeV)	Q_p (MeV)
2.150(34)	$9/2^+$	0^+		1.876(24)	29(8)	0.18(5)	1.907(24)
3.108(34)	$[13/2^+]$	$(9/2^+)$	957.6(5)		30(8)		
4.147(34)	$[17/2^+]$	$[13/2^+]$	1039(2)		15(7)		
5.844(34)	$[21/2^+]$	$[17/2^+]$	1697(2)		9(4)		

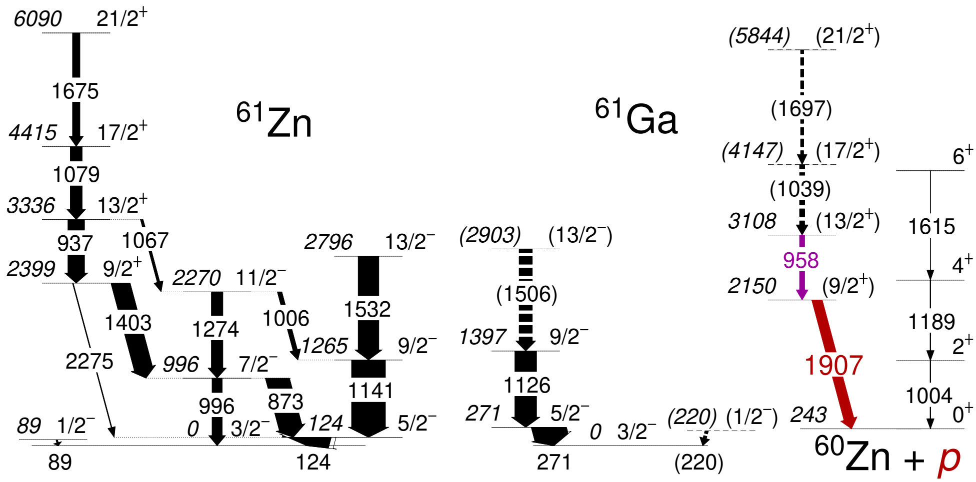

Figure 4.6: The proposed level scheme for ^{61}Ga (right) [45] with newly identified proton emitting state E_x = 2150-keV highlighted in red together with tentative transitions building on top of the state with 958-keV γ-transition marked in magenta. All energy values are given in keV, relative to the ground state of ^{61}Ga [43, 69, 70]. Corresponding parts of the level schemes for its mirror nucleus ^{61}Zn (left) [67] and ^{60}Zn (rightmost) [72] are shown for comparison. Tentative transitions and levels are represented with dashed lines, and the arrow widths reflect the relative intensities of the transitions. This figure is reproduced from Paper IV.

4.4.2 Tentative proton lines from ^{61}Zn

Two newly identified tentative proton lines, $E_{p1} \approx 2.0$ MeV and $E_{p2} \approx 3.0$ MeV, in coincidence with newly identified 779-keV and 1366-keV γ transitions deserve to be studied [see Fig. 4.4 panels (e) and (f)]. Looking at the Q values of the proton peaks, spin-parity conservation, and energies of known excited states, ^{61}Cu proton emission into ^{60}Ni can be practically ruled out. In turn, both candidate proton lines can be tentatively assigned to ^{61}Zn proton emission to excited states in ^{60}Cu. An attempt of an assignment of the proton lines is sketched in Fig. 4.7.

The first one is $E_{p1} \approx 2.0$ MeV. It could originate from branches in normally deformed structures in ^{61}Zn [67], for example, a $21/2^+$ to $19/2^+$ transition being a 779-keV γ emission followed by $g_{9/2}$ proton emission from the $19/2^+$ state into the 5^+ excited state in ^{60}Cu.

The second proton peak with energy $E_{p2} \approx 3.0$ MeV is tentatively linked to the superdeformed band 1, SD1, in ^{61}Zn [67]. The 1366-keV γ-ray transition associated with the proton could correspond to the $29/2^+ \rightarrow 25/2^+$ deexcitation in SD1. The proton line emission from the $25/2^+$ state would result in an 8^+ exited state of ^{60}Cu by emitting a $g_{9/2}$ proton. In case the $g_{9/2}$ proton stems from a $23/2^-$ excited state, it would end in the 7^- excited state in ^{60}Cu.

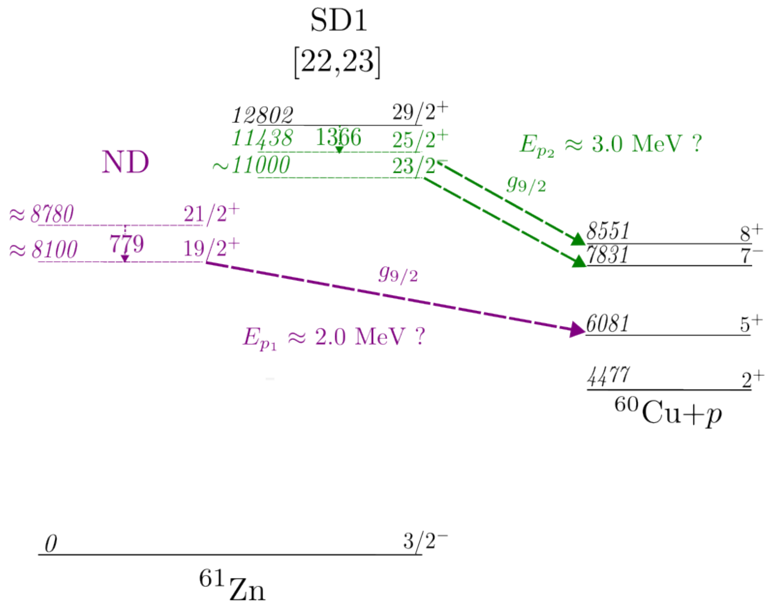

Figure 4.7: Suggested tentative assignment of two proton lines, E_{p1} (purple) and E_{p2} (green). The 779-keV γ-ray transition associated with E_{p1} with suggested level assignment is drawn in purple. Two suggestions assigning the tentative E_{p2} with 1366-keV γ ray are shown in green. ND and SD1 mark a normally deformed structure and superdeformed band 1 in ^{61}Zn, respectively [72]. Previously known energy levels in ^{61}Zn and ^{60}Cu are portrayed in black [72].

4.4.3 Angular distribution of prompt protons

^{61}Ga prompt protons are expected to have a $\ell = 4$ angular distribution, which is strongly forward focused in the laboratory reference frame. Experimental θ values of the proton peak of interest are obtained on an event-by-event basis for events that fulfill the E_p and E_γ requirements of the proton peak of interest. Since the rings in DSSD1 are not equidistant (see Sec. 3.3.1), each ring covers a different solid angle. To correct for this, the total solid angle as seen by the detector is calculated, Ω_{tot}, and a solid angle of each ring is computed. The number of experimental counts associated with a specific ring is corrected to make each ring have an equal contribution to the solid angle making it $\frac{\Omega_{tot}}{32}$. θ values are then converted from the laboratory into the center-of-mass frame. DSSD1 angular coverage of about 12° to 35° along the beam axis in the laboratory frame, corresponding to some 20° to 90° in the center-of-mass reference frame.

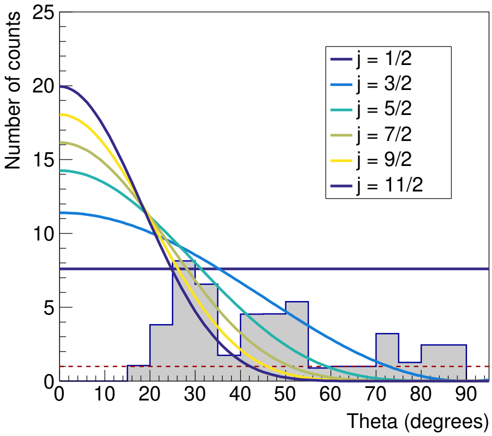

Figure 4.8: Angular distribution of $g_{9/2}$ proton counts coming from ^{61}Ga experimentally measured (gray counts) and theoretically predicted for different j (six lines). Experimental values for θ are converted into the center-of-mass frame. The special geometry of DSSD1 with not equidistant rings is taken into account, see text for details. The experimental background is indicated with the red dashed line. Theoretical θ values are reproduced from Ref. [73] and scaled by the same factor to match the experimental data.

A comparison of the experimentally obtained and theoretically predicted [73] angular distribution of the newly identified proton line in ^{61}Ga is shown in Fig. 4.8. Experimental θ counts are depicted in gray with a constant background indicated with the red dashed line. Theoretically predicted angular distributions for increasing j reproduced from [73] for odd-Z proton emitters that populate the ground state (0^+) of the daughter nuclei are portrayed in differently colored lines. All theoretical functions are multiplied by a factor to adapt them to the experimental values. The plot indicates that the most decisive region with $\theta_{c.o.m.} = [0°, 20°]$ is not covered in the present experimental setup. Limited statistics in the experimental dataset does not allow for clear assignment. However, several conclusions can be drawn: (i) $j = 1/2$ can be excluded as the constant line is hardly compatible with the data, (ii) $j = 11/2$ is likely to be excluded due to a more narrow width, (iii) the best fitting options are $j = [5/2, 7/2, 9/2]$. An important note to consider is that the ^{61}Ga spin axis is affected by particle evaporation from the compound nucleus ^{64}Ge. As the compound nucleus evaporates particles, it gradually loses its initial orientation within the reaction plane. This process, along with the subsequent γ-ray emission in ^{61}Ga, dampens the original spin alignment and further complicates any ℓ assignment.

Chapter 5

Shell-model calculations

The discovery of a weakly proton-bound state in ^{61}Ga together with several tentative excited states on top provides a perfect test ground for existing theoretical models. Shell-model calculations describing the newly discovered positive-parity states in ^{61}Ga are detailed in Paper IV and its Supplemental Material. In this Chapter, important theoretical concepts of the work are explained starting with the nuclear shell model in Sec. 5.1, isospin symmetry, and mirror nuclei in Sec. 5.2, and the description of nuclear shell model calculations in Sec. 5.3. Additional comments regarding shell-model results in comparison to experimental findings for several nuclei in the upper fp shell including the $A = 61$ mirror-pair ^{61}Zn - ^{61}Ga are given in Sec. 5.4.

5.1 Nuclear shell model

The nuclear shell model describes the arrangement of protons and neutrons in discrete energy levels within the atomic nucleus. It can be seen as analogous to the Bohr model for atoms in that both describe particles occupying discrete energy levels, with enhanced stability linked to filled shells. In the atomic shell model, electrons occupy orbitals around the nucleus, with filled electron shells leading to chemically inert elements, the noble gases. Similarly, in the nuclear shell model, protons and neutrons, also called nucleons, fill energy levels within the nucleus. Filled nuclear shells correspond to particularly stable nuclei, often identified by the so-called magic numbers. For nuclei not too far from the line of stability, nuclear magic numbers include 2, 8, 20, 28, 50, and 82 for protons and neutrons with an additional 126 for neutrons. While atomic shells are shaped by the Coulomb potential due to the electrostatic attraction between electrons and the positively charged nucleus, nuclear shells are governed by the nuclear potential, primarily resulting from the strong nuclear force. This potential is much more complex, incorporating both a central attractive force and additional contributions like the spin-orbit interaction, which significantly influence the energy levels and thus the overall structure of a given nucleus.

The behavior of nucleons within the nucleus can be described starting with the time-independent Schrödinger equation:

$$H\Psi = E\Psi \tag{5.1}$$

The Hamiltonian for an A-nucleon system consists of the kinetic energy of individual nucleons and potential energy among all nucleons:

$$H = \sum_{i=1}^{A} t_i + \frac{1}{2}\sum_{i \neq j}^{A} v_{ij}(\vec{r_i}, \vec{r_j}) \tag{5.2}$$

The first part of the Hamiltonian is total kinetic energy computed as a sum of the individual kinetic energies:

$$t_i = -\frac{\hbar}{2m}\Delta_i \tag{5.3}$$

The second part of the Hamiltonian is the potential energy between two particles i and j, depending on their relative positions $\vec{r_i}$ and $\vec{r_j}$. Note that $i \neq j$ is an important restriction meaning that the particles are not allowed to interact with themselves, which takes care of the Pauli exclusion principle. No exact form of nuclear potential exists, because the derivation of a comprehensive nucleon-nucleon force from underlying first principles remains challenging. The nucleon-nucleon interaction is not completely understood.

For simplification, the nuclear Hamiltonian can be divided into two parts:

$$H = H_{central} + H_{residual}, \tag{5.4}$$

where $H_{central}$ contains a central potential, which approximates the motion of each nucleon as if it moves independently in a common average field. $H_{residual}$, in this case, accounts for the remaining correlations between nucleons that are not captured by the central potential and can be treated as a small perturbation in energy with respect to the central potential. This approach allows us to use perturbation theory to analyze the influence of the residual interactions on the energy levels and wave functions of the nucleons.

The central part then becomes:

$$H_{central} = \sum_{i=1}^{A} (t_i + U_i), \tag{5.5}$$

with its main purpose being to describe magic numbers, energy gaps, and the energy sequences of orbitals experimentally observed.

The residual part is given by:

$$H_{residual} = \frac{1}{2} \sum_{i \neq j}^{A} v_{ij}(\vec{r_i}, \vec{r_j}) - \sum_{i=1}^{A} U_i. \tag{5.6}$$

This term accounts for the correlations between nucleons not included in the independent description, for instance, pairing interactions between nucleons in the same shell and configuration mixing.

Shell-model potential

A good approximation of an average nuclear potential is Woods-Saxon potential [74]:

$$U_{WS}(r) = \frac{-V_0}{1 + \exp \frac{r-R}{a}}, \tag{5.7}$$

where V_0 is the depth of the potential well, R is the the mean radius, and a is the skin diffuseness thickness. The values are chosen to fit the measurements, with V_0 being of the order of 50 MeV to give the proper separation energies, and $a \approx 0.55$ fm [74].

The inclusion of spin-orbit coupling [75], which adds the interaction between the orbital angular momentum $\vec{\ell}$ and the spin $\vec{s}$, is essential to reproduce the experimentally observed large energy gaps, corresponding to the magic numbers. The spin-orbit term, $V_{\ell s}$, is [71]:

$$U_{\ell s} = \lambda \left(\frac{1}{r} \frac{d}{dr} U(r) \right) \vec{\ell} \cdot \vec{s}, \tag{5.8}$$

where $U(r)$ could be any radial potential, λ is a constant scaling the strength of the spin-orbit interaction, $\vec{\ell} \cdot \vec{s}$ is the dot product of the orbital angular momentum $\vec{\ell}$ and the spin $\vec{s}$.

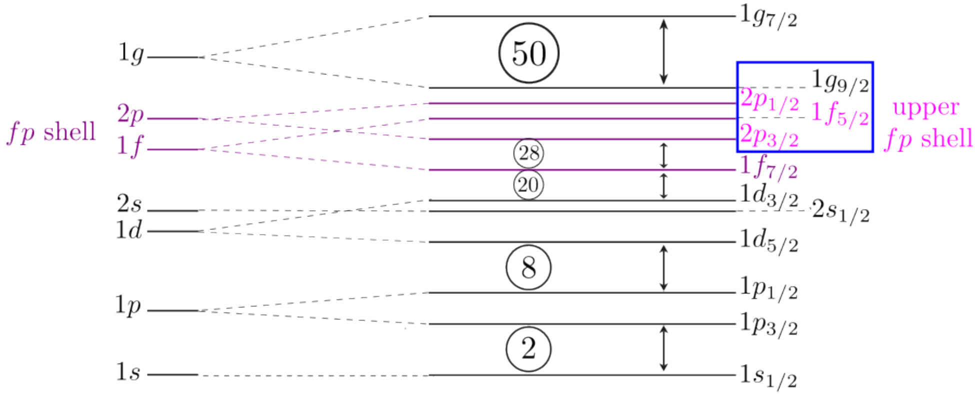

Figure 5.1: Shell-model orbitals with magic numbers reproduced using a Woods-Saxon potential parametrization including spin-orbit coupling. Magic numbers are indicated inside circles. All orbitals corresponding to the fp shell are in magenta, while the upper fp shell orbitals are written in pink. Orbitals belonging to the "$f_{5/2}pg_{9/2}$" model space are enclosed in the blue rectangle. Adapted from Ref. [74].

Although the Woods-Saxon potential is a good approximation, its disadvantage for practical applications is that it cannot be solved analytically. To address this, the modified oscillator potential was introduced by S.G. Nilsson [76, 77]:

$$U_{MO} = \frac{1}{2}\hbar\omega_0\rho^2 - \kappa\hbar\omega_0 \left[2\ell \cdot s + \mu(l^2 - \langle l^2\rangle_N)\right], \tag{5.9}$$

with

$$\rho = \left(\frac{m\omega_0}{\hbar}\right)^{\frac{1}{2}} r, \tag{5.10}$$

where μ and κ are parameters controlling the spin-orbit and orbital angular momentum contributions, respectively. $\hbar$ is the reduced Planck constant and ω_0 is the angular frequency of the oscillator. The modified oscillator potential offers an analytical solution, making it more practical for certain nuclear structure calculations, especially when analyzing deformed nuclei.

The quantized energy levels resulting from solving the Schrödinger equation for these potentials provide the foundation for understanding nuclear shell structure. As shown in Fig. 5.1, the inclusion of the spin-orbit term is crucial for explaining the splitting of these levels, leading to the experimentally observed magic numbers. The figure highlights the upper fp shell, which is of interest for this thesis, in particular those at $N = Z = 28$ and $N = Z = 50$.

Mean field approach

Beyond the nuclear shell model, more advanced approaches such as the Hartree-Fock (HF) and Hartree-Fock-Bogoliubov (HFB) methods can provide a more realistic description of nuclear structure. In the HF method, nucleons interact with an average mean field created by all other nucleons, allowing the system to self-consistently adjust the potential based on particle correlations. This approach goes beyond the independent particle approximation of the shell model by incorporating the effects of nucleon-nucleon interactions. The Hartree-Fock-Bogoliubov method extends HF by including pairing correlations between nucleons. These methods are crucial for capturing deformation, pairing effects, and more complex structures of nuclei, especially those far from stability.

5.2 Isospin symmetry

The isospin quantum number, t, was introduced by W. Heisenberg in 1932 to explain the similarities between protons and neutrons in the nucleus, considering them as two states of a single particle, the nucleon [78]. Using this notation and projecting it onto the quantization z-axis results in $t_z(n) = +1/2$ for neutrons and $t_z(p) = -1/2$ for protons. The total isospin projection of a nucleus is then given as:

$$T_z = \frac{1}{2}(N - Z), \tag{5.11}$$

where N and Z denote the number of neutrons and protons in the nucleus.

Isospin symmetry is a fundamental concept assuming nuclear charge symmetry and independence under the strong force dominating inside the nucleus. It is possible to experimentally probe the symmetry by studying pairs of mirror nuclei with the same number of nucleons but the number of protons and neutrons interchanged. Corresponding energy levels in mirror pairs are called isobaric analogue states, which should be identical assuming isospin symmetry. In reality, there are several isospin-breaking terms that result in usually small differences in excitation energy between corresponding levels in mirror nuclei. Those are denoted as mirror energy differences (MED):

$$MED_J = E_J(T_z = -T) - E_J(T_z = +T), \tag{5.12}$$

where E_J is the excitation energy of a state with spin J.

Two main contributors to MED are the Coulomb multipole effects, V_{CM}, and the Coulomb monopole effects, V_{Cm}. For comparison with experimental data, an additional isovector term, V_B, may have to be included. Thus MED can be expressed as [79]:

$$MED_J = \Delta\langle V_{CM}\rangle + \Delta\langle V_{Cm}\rangle + \Delta\langle V_B\rangle, \tag{5.13}$$

where angle brackets denote the energy expectation value at spin J. All isospin-symmetry breaking terms are detailed below. Note that $\Delta\langle V_B\rangle$ breaks isospin symmetry on the level of the strong nuclear force.

The Coulomb multipole effect, V_{CM}, is related to proton-proton interaction inside a nucleus and is added to proton-proton two-body matrix elements (TBME) in the context of shell-model calculations. The effect accounts for the breaking and alignment of proton pairs, as the average distance between nucleons differs based on the alignment, which directly impacts the strength of the Coulomb repulsion. Specifically, the repulsion is weaker for aligned pairs and stronger for anti-aligned pairs. This contributes to MED, as energy differences arise when comparing a nucleus with breaking and aligning a proton-proton pair to one with neutron-neutron or proton-neutron pairs. This effect contributes approximately 10-100 keV as reported for the upper fp shell pairs [79].

The Coulomb monopole effects, V_{Cm}, are further divided into a V_{Cr} term constituting deformation and radial effects, and $V_{C\ell s}$ for the electromagnetic spin-orbit interaction [79].

According to the nuclear shell model, shell effects and particle configuration influence the nuclear charge distribution depending on the state. The V_{Cr} term is included to account for changes in the radius of the charge distribution based on the occupation number of nucleons in the orbitals. This radial term also reflects deformation effects tied to multi-particle excitations in the shell model.

The electromagnetic spin-orbit term, $V_{C\ell s}$, has to be taken into account when dealing with excitations of particles between orbitals of opposite spin-orbit coupling. In the context of the upper fp shell, these would include excitations between $2p_{3/2}$ $(\ell + s)$ and $1f_{5/2}$ or $2p_{1/2}$ $(\ell - s)$ orbitals, respectively. The $V_{C\ell s}$ can be derived as:

$$\langle V_{C\ell s}\rangle = (g_s - g_\ell)\frac{1}{2m^2c^2}\langle\frac{1}{r}\frac{dV_C(r)}{dr}\rangle\langle\vec{\ell}\cdot\vec{s}\rangle, \tag{5.14}$$

where m is the mass of the nucleon, $V_C(r)$ is the Coulomb potential of the core, while g_s and g_ℓ are the gyromagnetic factors related to the motion of a nucleon related to the intrinsic spin and orbital motion, respectively.

The inclusion of the V_B term into MED calculation was motivated by the discrepancy between theoretically predicted and experimental values for excited mirror states in nuclei located in the $1f_{7/2}$ shell, i.e., between ^{40}Ca and ^{56}Ni. This was explained by the presence of charge asymmetric components of the strong nucleon-nucleon interaction and their contributions included in the V_B term [80].

Specific values used as isospin-breaking terms for studying $A = 61$ ^{61}Zn - ^{61}Ga mirror pair are included in Paper IV and its Supplemental Material.

5.3 Shell-model calculations with ANTOINE

Nuclear shell-model codes are essential for describing large nuclear systems, offering precise predictions of energy levels, transition probabilities, and other nuclear properties that are otherwise analytically unattainable. Mirror energy differences for the ^{61}Ga and ^{61}Zn pair are presented in Paper IV. They were computed using the shell-model code ANTOINE [81, 82]. In the following, the basic interactions used in the code as well as additional considerations for results computed for several nuclei in the upper fp shell (cf. Fig. 5.1) are given.

5.3.1 Method

The ANTOINE shell-model code evaluates the nuclear Hamiltonian based on single particle energies (SPEs) and two-body matrix elements (TBMEs). SPEs represent the energy levels of individual nucleons in a nucleus, assuming no interactions between them. TBMEs, on the other hand, represent the interaction between pairs of nucleons and are crucial for determining the energy levels and other properties of the predicted nuclear states.

The Hamiltonian for two states can be expressed as

$$H = \begin{pmatrix} \epsilon_{a_1} & 0 \\ 0 & \epsilon_{a_2} \end{pmatrix} + \begin{pmatrix} \langle\phi_1|V_{11}|\phi_1\rangle & \langle\phi_1|V_{12}|\phi_2\rangle \\ \langle\phi_2|V_{21}|\phi_1\rangle & \langle\phi_2|V_{22}|\phi_2\rangle \end{pmatrix}, \tag{5.15}$$

where ϵ_a are the single-particle energies and $|\phi\rangle$ are the basis states characterized by given quantum numbers such as spin, parity, and isospin. The first matrix contains the SPEs, while the second represents the TBMEs, with diagonal values as the expectation values for interactions and off-diagonal elements representing state mixing. By diagonalizing this Hamiltonian matrix, one obtains the energy eigenvalues corresponding to different nuclear states.

The ANTOINE code employs the Lanczos method, an iterative algorithm designed to efficiently compute eigenvalues and eigenvectors of large, sparse Hamiltonian matrices. This method reduces computational complexity by generating a Krylov subspace and constructing a smaller tridiagonal matrix, facilitating the computations.

The diagonalization of large Hamiltonians often requires substantial computational power, especially when dealing with nuclei proton and neutron numbers far away from doubly-magic "inert" cores. By defining an inert core, for example, using $N = Z = 20$ ^{40}Ca or $N = Z = 28$ ^{56}Ni, one reduces the number of valence nucleons, t, participating in the calculation. Therefore, ANTOINE uses several so-called interaction files, where the SPEs and TBMEs are often adjusted based on experimental data to best reflect the interaction region under study.

The code includes different interactions: the Cohen-Kurath interaction [83] for $4 \leq A \leq 16$ (the p shell), the USD interaction [84] for $16 \leq A \leq 40$ (sd shell), KB3G [85], gxpf1a [86] for $40 \leq A \leq 80$ (the fp shell), and JUN45 [87] for $56 \leq A \leq 100$ (the $f_{5/2}pg_{9/2}$ orbitals). Since the latter two are more modern interactions for the fp shell and the focus of the Paper IV relies primarily on $A = 57, 61$, the interactions are detailed below.

Up front, gxpf1a and JUN45 are semi-empirical, i.e., they are based on realistic nucleon-nucleon potentials, but to a larger or lesser extent fitted to experimental data. The gxpf1a interaction is tuned for nuclei around ^{56}Ni and JUN45 for upper fp shell nuclei.

gxpf1a

The gxpf1a interaction [86] has been successfully tested for the fp shell. The interaction includes the full fp shell, i.e., the orbit $1f_{7/2}$ below and the $2p_{3/2}$, $1f_{5/2}$, and $2p_{1/2}$ orbitals above the $N = Z = 28$ shell closure. Note, all these orbitals have odd angular momentum values, i.e. ℓ=1 for p and ℓ=3 for f, meaning they cannot generate positive parity states for odd-A nuclei like ^{61}Zn or ^{61}Ga.

JUN45

JUN45 [87] is one out of several of "$f_{5/2}pg_{9/2}$" interactions that exclude the $1f_{7/2}$ orbit from its calculation as it uses the ^{56}Ni core and allows excitations only outside of its core. Instead, $1g_{9/2}$ orbital is included since the interaction is adjusted for nuclei with $N, Z > 28$ and $N, Z < 50$. It is tuned for the upper fp shell of $N \gtrsim Z$. The inclusion of the $1g_{9/2}$ orbital is necessary for the description of the positive-parity states in $A = 61$ nuclei of interest in this thesis.

5.4 Results for fp shell calculations

5.4.1 Predictions of excited states

As illustrated in Fig. 4 of Paper IV, the experimental values of MEDs for the $A = 57$ and $A = 61$ mirror pairs are well-reproduced by the gxpf1a ($\pi = -$ states only) and JUN45 interactions. However, a notable concern arises: while the MEDs align closely with experimental values, the energy levels of these nuclei themselves do not exhibit the same level of agreement when compared to reported experimental data.

Figure 5.2 shows a comparison of experimentally measured and theoretically predicted excited states for several nuclei in the $A = 60$ region. In addition to the ^{61}Ga and ^{61}Zn pair, ^{61}Cu, ^{58}Cu, and ^{62}Ga are included for comparison. The number of excitations across the shell gaps at ^{56}Ni for gxpf1a is limited to $t \leq 6$.

Starting with ^{61}Ga [panel (a)] and ^{61}Zn [panel (b)], gxpf1a is in excellent agreement with the few known negative-parity states in ^{61}Ga and respective states in ^{61}Zn. Predictions of the JUN45 interaction, however, are slightly different from experimental values for negative-parity states and overestimate positive-parity states by about 500 keV. It is important to recall that the energies for positive-parity states are only possible to predict with JUN45 since it specifically includes the $1g_{9/2}$ orbital. One should also note that the states are overestimated in ^{61}Ga and ^{61}Zn with the same offset. Hence, the effect cancels out when calculating MEDs.

Energies of selected negative and positive parity states in ^{61}Cu predicted with ANTOINE are presented in Fig. 5.2(c). ^{61}Cu is the $Z = 29$ and $N = 32$ nucleus, indicating one proton and four neutrons more than doubly-magic ^{56}Ni core. The extra proton can be placed in the $2p_{3/2}$ orbital, with the four neutrons forming pairs in, e.g., $1p_{3/2}$ or $1f_{7/2}$ orbitals. Thus, the expected ground state of ^{61}Cu is $3/2^-$ in line with experiment. Starting with negative parity states, the $11/2^- \rightarrow 7/2^- \rightarrow 3/2^-$ cascade energies are well reproduced with the JUN45 interaction file. However, in the case of the $5/2^-$ state, the excitation energy is overestimated by about 400 keV. This may indicate that the SPE for $f_{5/2}$ needs to be adjusted, which could lead to a better agreement for the whole $13/2^- \rightarrow 9/2^- \rightarrow 5/2^-$ cascade with experimental data. This is significant because the $9/2^-$ and $13/2^-$ states also involve a proton in the $f_{5/2}$ orbital and excitations of neutrons from broken neutron pairs. When looking at the positive-parity states in ^{61}Cu, it is clear that the JUN45 interaction is not well optimized for the nucleus. The $9/2^+$ state is significantly overestimated, similar to the $A = 61$ pair mentioned above, even though the predicted energies of $13/2^+$, $17/2^+$, and $21/2^+$ states are in good agreement with the experimental data. This indicates that to correct the $9/2^+$ states, TBME elements must be carefully adjusted, requiring a delicate balance to avoid compromising the agreement for the higher excited states.

Figures 5.2(d) shows predicted vs. experimentally measured energies predicted with JUN45 for two odd-odd $N = Z$ nuclei ^{58}Cu and ^{62}Ga. Starting with the $N = Z = 29$ ^{58}Cu nucleus, the predicted energy for its 3^+ excited state is in perfect agreement with the experimental data. The problem arises already with the 5^+ state, representing both the valence proton and neutron aligned in the $f_{5/2}$ orbital. The overestimation of this state is similar to the ^{61}Cu nucleus' $5/2^-$ state discussed earlier, being approximately twice that value since there are two valence nucleons in ^{58}Cu. The predicted energy for the 9^+ excited state in ^{58}Cu also does not agree well with the experimental observation. In analogy to the $9/2^+$ state in ^{61}Cu with a single proton in the $1g_{9/2}$ orbital, ^{58}Cu has one proton and one neutron in the orbital in its 9^+ excited state, indicating that the solution would also involve adjusting the TBMEs. Finally, the predicted 7^+ state is completely incorrect, which can be explained by the absence of the $1f_{7/2}$ orbital in the JUN45 model space, limiting the model's ability to predict this state accurately. As for $N = Z = 31$ ^{62}Ga nucleus, it is important to recall that there are six valence nucleons in the upper fp shell. While the calculated energies for the 1^+, 3^+, and 7^+ are well reproduced, there are challenges in accurately predicting the 5^+, 9^+, and 11^+ excited states. Due to the larger number of valence nucleons in ^{62}Ga compared with ^{58}Cu, there are many more configurations to create, for instance, the 5^+ excited state in ^{62}Ga. Its predicted energy is thus dependent on an intricate combination of SPEs and TBMEs. Such adjustments must be made carefully, as the V_{Cls} term and thus predicted MED is highly sensitive to changes in the orbital configuration [79]. In turn, knowing experimental MEDs puts constraints on these modifications.

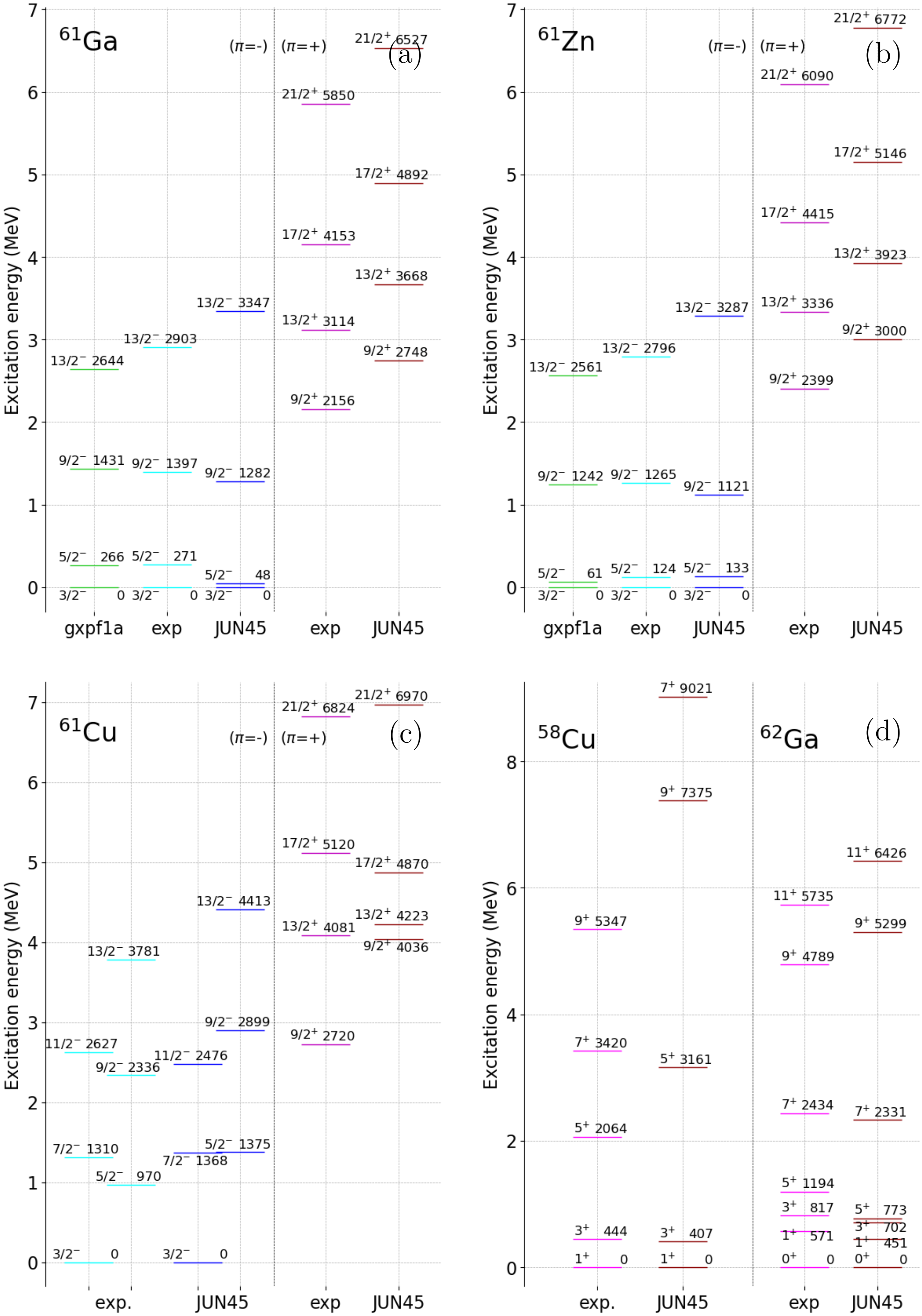

Figure 5.2: Excitation energies experimentally measured and theoretically predicted using the gxpf1a and JUN45 interactions for ^{61}Ga (a), ^{61}Zn (b), ^{61}Cu (c), ^{58}Cu, and ^{62}Ga (d).

5.4.2 Predictions of occupation numbers

In the ^{61}Ga nucleus, the configuration of the $9/2^+$ excited state can be understood as two protons and two neutrons outside the doubly magic ^{56}Ni core and in addition one proton in the $1g_{9/2}$ orbital. The mirror nucleus ^{61}Zn has the same configuration but instead with one neutron in the $1g_{9/2}$ orbital. The ground state in the daughter nucleus ^{60}Zn, reached by proton emission from the $9/2^+$ state in ^{61}Ga, is thus expected to have a very similar configuration as ^{61}Ga except for this single $1g_{9/2}$ proton. One expects a spectroscopic factor close to one because the overlap of the initial and the final wave functions of this proton-emission case is expected to be large. This is confirmed by the numerical result presented in Paper IV. One could verify the claim and further probe the validity of the JUN45 interaction used in Paper IV by looking at the predicted occupation numbers for different orbitals in positive-parity states in ^{61}Ga, and then compare to ^{61}Zn and ^{60}Zn as presented in Fig. 5.3.

At first, one can look at the single-particle character of the $9/2^+$ state in ^{61}Ga. The code also predicts the contributions of different particle configurations to the total wave function. Using the JUN45 interaction, the code predicts that the proton $1g_{9/2}$ single-particle contributions account for about 55% of the total wave function for the $9/2^+$ excited state in ^{61}Ga. This is consistent with ^{56}Ni being a soft doubly-magic core [88].

Occupation numbers refer to the number of particles, protons or neutrons, in each orbital for each state. For the present case, the numbers for ^{61}Ga, ^{61}Zn, and ^{60}Zn were calculated with the ANTOINE code.

Occupation numbers of protons and neutrons in the $p_{3/2}$, $f_{5/2}$, $p_{1/2}$, and $g_{9/2}$ orbitals as a function of spin of positive-parity states discovered in ^{61}Ga are shown in Fig. 5.3(b) in comparison to its mirror nucleus ^{61}Zn in panel (a). The occupation numbers for the even-spin yrast cascade of the daughter nucleus ^{60}Zn are shown in panel (c). Several conclusions can be drawn. In the mirror pair ^{61}Ga and ^{61}Zn, the occupancies of the $g_{9/2}$ proton and neutron orbitals are interchanged. In ^{61}Ga, the occupancy of the $\pi g_{9/2}$ is slightly greater than one, while the value for the $\nu g_{9/2}$ orbital is slightly above zero. For ^{61}Zn the situation is reversed. This is in line with the expected single-particle nature of the states. Note that the values are not exactly one and zero, since they correspond to average values including the cases of occasional additional nucleon $1g_{9/2}$ pairs present in the total wave functions of the states. The values for the $p_{3/2}$, $f_{5/2}$, and $p_{1/2}$ proton and neutron orbitals are expected to be the same for ^{61}Ga and ^{61}Zn assuming mirror symmetry. However, there are small but visible differences related to proton and neutron $p_{3/2}$ and $f_{5/2}$ orbitals. Given the electromagnetic

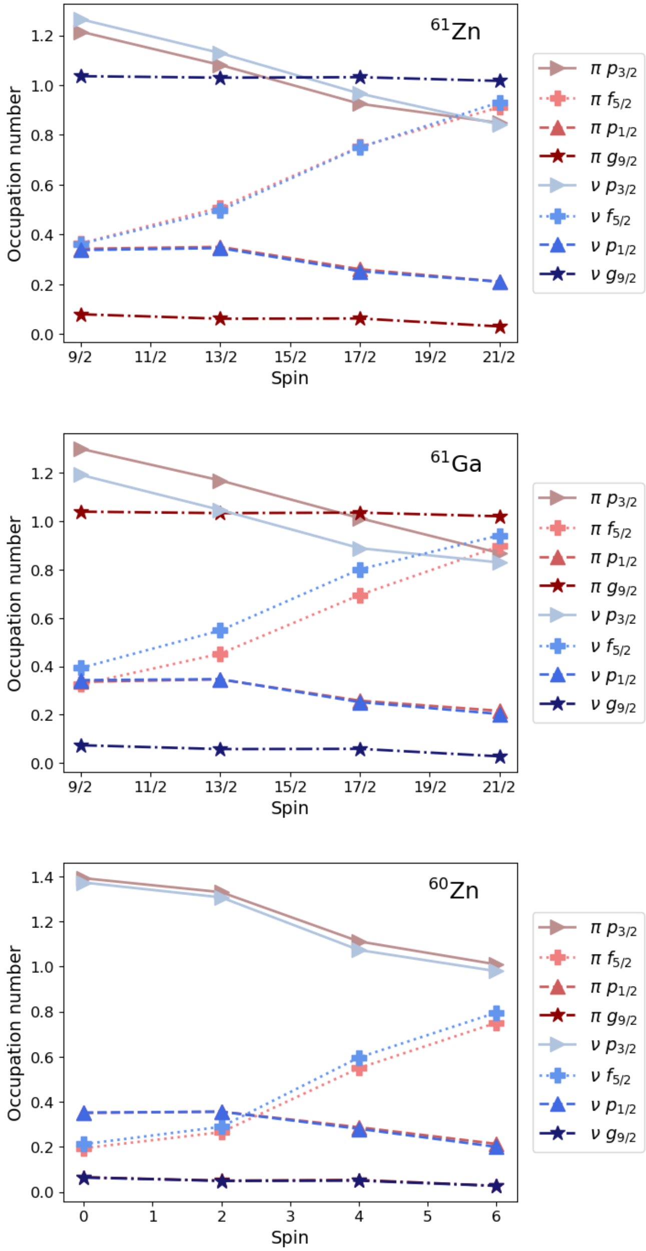

Figure 5.3: Occupation numbers of protons and neutrons in the $p_{3/2}$, $f_{5/2}$, $p_{1/2}$, and $g_{9/2}$ orbitals computed for positive-parity states in ^{61}Zn, ^{61}Ga, and ^{60}Zn with the ANTOINE shell-model code using the isospin-breaking version of JUN45 interaction file (see Paper IV). Proton occupation numbers are depicted with various red lines, while those for neutron orbitals are drawn with blue colors.

spin-orbit coupling nature of the orbitals, changing their occupational numbers has a large impact on the V_{Cls} term. Looking at the ^{60}Zn occupation numbers presented in Fig. 5.3(c), the values in both proton and neutron $1g_{9/2}$ orbitals are close to zero. This agrees with expectations as it lacks either an additional proton in ^{61}Ga or a neutron in ^{61}Zn, respectively. The occupancies in the rest of the orbitals are expected to be very similar to ^{61}Ga and ^{61}Zn. However, some deviations are observed for $p_{3/2}$ and $f_{5/2}$ orbitals. If one modifies SPEs and TBMEs (see Sec. 5.4.1) these occupation numbers are subject to change, which in turn influences predicted MEDs because of the $V_{\ell s}$ term as described in Sec. 5.2.

5.4.3 Conclusions

The JUN45 shell-model interaction in the $f_{5/2}pg_{9/2}$ space, incorporating isospin-breaking terms as used in Paper IV, provides a very good description of the experimental MED in the $T_z = \pm 1/2$, $A = 61$ mirror pair. However, comparing predicted energies of excited states in several other fp shell nuclei with experimental values highlights the necessity for further adjustments of the interaction to better describe the spectroscopic observables of those nuclei. Additional adjustments across more nuclei are needed before drawing conclusions regarding details of Coulomb effects in isospin breaking.

Chapter 6

Deuteron evaporation

The sensitivity of the DSSD-Microball system to light-charged particle detection enabled the clean identification of deuterons in the datasets of the experimental campaign. The complexity of the experimental setup and availability of information of all other detector systems, including γ-rays, neutrons, and recoil mass A information, opens up the possibility of unprecedented in-beam deuteron-γ coincidence studies. Of specific interest is that the compound nuclei produced during the first two experiments are $N = Z$ nuclei. In this Chapter, details on experimental data analysis and theoretical considerations leading to Paper V are presented.

6.1 Motivation

As presented in Fig. 3.2, all compound nuclei created during the first and second experiment have equal number of neutrons and protons, $N = Z$. For these compounds, we have experimental information available for several evaporation channels, allowing for a quantitative comparison of production yields with d vs. pn evaporation. One of the ideas behind this study was to investigate whether neutron-proton pairing is enhanced for $N = Z$ nuclei, in comparison to, for example, $N = Z + 1$ or $N = Z + 2$ systems.

The following nuclei were selected for this study: ^{49}Cr, ^{53}Fe, ^{61}Zn, ^{60}Cu, and ^{58}Cu, which were produced via different evaporation channels involving d or pn emission. These nuclei resulted from reactions such as $2pn$ (^{61}Zn), $3pn$ (^{60}Cu), and αpn (^{58}Cu), as well as the competing dp, $d2p$, and αd channels from the ^{64}Ge* compound nucleus. $2pn$ and dp evaporation channels lead to ^{49}Cr and

^{53}Fe recoils from ^{52}Fe* and ^{56}Ni* compounds, respectively. This selection offers a broad range in mass number A and provides a good basis for first studies.

Fusion-evaporation codes presently in use often do not take into account deuteron evaporation. They focus on the more common neutron, proton, and α evaporation followed by statistical γ-ray emission. These codes are frequently utilized to estimate reaction pathways for the production of exotic nuclei at the stage of planning experiments. A recent assessment [89] of various codes highlighted a significant issue with overestimated production cross-sections, that could potentially lead to inaccurate beam-time requests and other experimental complications. One potential reason for this discrepancy is the lack of experimental data or large uncertainties in existing data. This underscores the need for a reassessment of these codes and an effort to provide them with high-quality experimental data. Another possible factor is the absence of deuteron evaporation in most of these models. It may have been excluded because it is expected to be less likely than single particle emission, and due to the lack of experimental data indicating its contribution to fusion-evaporation process. Experimentally, it is difficult to distinguish deuterons from evaporated protons, as both particles have similar charges and thus energy depositions in charged-particle detectors. In fact, the study is only possible due to the use of the highly-pixelized Si detection system, combined with modern detector readout technologies and the integration of multiple detector systems.

It is particularly interesting to examine what the relative ratio of the production of nuclei of interest via deuteron vs. the more common $p + n$ evaporation is. Preliminary explorations of this topic were conducted in the context of the B.Sc project of Sean Mc Caughley [90], revealing that a more comprehensive study would be worthwhile. The comprehensive study, along with theoretical support, led to the publication of the Paper V. In the following, theoretical considerations, experimental data preparation, and key findings are presented.

6.2 Theoretical considerations

The term "evaporation" in this context in nuclear physics refers to the process in which particles are emitted from an excited nucleus in a manner analogous to the evaporation of particles from an ideal fluid composed of non-interacting, structureless particles held at a fixed temperature within a fixed volume [91].

This concept is formalized in the Weisskopf theory of evaporation from a compound nucleus [92], which compares the energy stored in the compound nucleus with the heat energy of a solid body or a liquid, and, the subsequent expulsion of particles to be analogous to an evaporation process. The statistical model of particle evaporation initially developed by Weisskopf was later refined through the Hauser-Feshbach treatment [93, 94]. The latter forms the basis for several codes currently used to calculate fusion-evaporation cross-sections [95, 96, 97, 98].

For the study in Paper V, theoretical computations were performed by A. Idini, using Weisskopf model to analyze the emission of deuterons and protons around the $N = Z$ line and to compare to experimental data. The Weisskopf model for single- and multi-particle emission is detailed below.

6.2.1 Weisskopf model

The Weisskopf model calculates the decay width, Γ, representing the probability per unit time of transition via particle or γ-ray emission from a particular nuclear state per unit time. The model can be expanded from single-particle to multi-particle emission as described below, adapted from notes from A. Idini [99].

Single-particle emission

The decay width, Γ, of the nuclear state is the integral of the emission probability, W, over all possible transitions:

$$\Gamma(E_m^*) = \int_0^\infty W(E, E_m^*)\mathrm{d}E, \tag{6.1}$$

This emission probability depends on the energy of the emitted particle, E, the excitation energy of the mother, E_m^*, and daughter nuclei, E_d^*, and the cross section of the reaction.

The probability for emitting a particle with energy E from a nuclear state with excitation energy E_m^*, if the Q–value is positive, is

$$W(E, E_m^*) = gmE\sigma \frac{\rho_d(E_d^*)}{\rho_m(E_m^*)} \tag{6.2}$$

where g is the degeneracy of the final state of the emitted particle and m is its mass. The level density for mother and daughter states are denoted as ρ_d and ρ_m, respectively. These are calculated at the corresponding excitation energy E^*. This probability of decay is given by the ratio of the phase space of the initial and final state multiplied by the cross section for the decay, in particular particle emission. Assuming no internal excitation of the emitted particle, the excited state of the daughter nucleus can be calculated as:

$$E_d^* = E_m^* - E + BE_d - BE_m + BE_p, \tag{6.3}$$

where BE_d, BE_m, and BE_p correspond to the binding energies of the daughter and mother nuclei states and the eventual binding energy of the emitted particle respectively.

The cross section for particle emission is modeled geometrically and includes corrections for quantum tunneling effects. The level density of the nucleus is derived using the equidistant model from a harmonic oscillator potential.

For comparison with experimental data, the yield of particle emission, $\tilde{Y}_p$, can also be computed. It is calculated by integrating the decay width and level density of the final state over the relevant energy range:

$$\tilde{Y}_p(E_d^*) = \int_{E_d^*}^{E_m^* - Q} \tilde{\Gamma}_p(E)\rho_d(E)\mathrm{d}E, \tag{6.4}$$

with E_d^* the final state energy, E_m^* the compound nucleus excitation energy, and Q the Q–value of the decay.

Multi-particle emission

Building on the single-particle emission framework, the Weisskopf model can be extended to account for multi-particle emissions, as shown below. Considering multiple subsequent decays, such as for example $2pn$ or dp evaporation of interest in the study, the probability of emission will be the product of the probability of the subsequent decays.

Using the example of two particle emission, such as dp from ^{52}Fe compound resulting in ^{49}Cr, the emission probability W_{dp} is then:

$$W_{dp}(E_p, E_d, E_{52Fe}^*) = 6m_d m_p \sigma_d \sigma_p E_p E_d \frac{\rho_d(E_{49Cr}^*)}{\rho_m(E_{52Fe}^*)}, \tag{6.5}$$

where E_p and E_d in this case are energies of evaporated proton and deuteron, respectively, and $g = 6$ is the degeneracy of the deuteron-proton evaporation process. This leads to the following expression for the decay width:

$$\Gamma_{dp}(E^*_{^{49}Cr}) = \int_0^{E_p^{\max}} W_{dp}(E_p, E_d, E^*_{52Fe})\mathrm{d}E_p \tag{6.6}$$

Assuming that the second emission is also prompt, so that there are no intermediate decays, the state of the daughter for the first decay is the mother of the second. Therefore, the probability of subsequent decays depends only on the level density of the first compound nucleus state and the final state. The same applies when there are more decays involved. The decay width of multiparticle decay will be obtained by integrating over the allowed emitted energy.

This indicates an interesting property of multiple particle decay, that, in the end, has only a minor dependency on the properties of intermediate nuclei in the form of the cross section. For cross section calculations the path dependence is minor and relevant only at the highest excitation energies of the final daughter nucleus.

6.2.2 Hauser-Feshbach formalism

The Hauser-Feshbach formalism [93, 94] offers a more detailed approach for modeling particle emission by treating the nucleus as a compound system in thermal equilibrium. Unlike the Weisskopf formalism, which simplifies the emission process and is often used for single-particle emissions, the Hauser-Feshbach model accounts for multiple decay channels and complex multi-particle emissions through a statistical treatment. It incorporates the density of states, transmission coefficients, instead of emission cross-section, and competition between different decay channels, offering a more detailed and refined characterization of the decay process. Although the Weisskopf formalism can also be adapted for multi-particle emission, the Hauser-Feshbach approach is generally considered more comprehensive.

One significant improvement in the Hauser-Feshbach formalism is its use of transmission coefficients, which describe the probability that a particle will penetrate the nuclear potential barrier. These coefficients are energy-dependent, offering a more accurate depiction of the emission process, particularly for charged particles, where the Coulomb barrier is important. These coefficients can also depend on emission angles for non-spherical nuclei. The Weisskopf model, by contrast, assumes a constant geometric cross-section, which can limit its accuracy in such cases.

Another advantage of the Hauser-Feshbach model is its ability to incorporate angular momentum coupling. The emission process takes into account the conservation of angular momentum and parity, which is particularly relevant when high-spin states or angular momentum of the emitted particles influence the decay.

Finally, the Weisskopf model, though adaptable to multi-particle decays, typically treats each decay as an independent event, while the Hauser-Feshbach approach considers competition between different decay channels and interactions that occur within more complex decay sequences.

For our study, the Weisskopf formalism was sufficient due to its simpler application and the adequacy of its results for our analysis. Although the Hauser-Feshbach model provides greater precision for complex decay processes, the Weisskopf approach was sufficiently accurate for our purposes.

6.2.3 Preformation factors

Preformation factors are quantities that help us evaluate the probabilities used in nuclear physics to describe the likelihood of a nuclear cluster (like a deuteron or α particle) forming inside a nucleus before the emission process occurs. It is interesting to explore deuteron preformation in the context of the Paper V. Here the simplified description of deuteron preformation is given in comparison to the more studied α preformation.

α-particle preformation

The preformation of an α particle refers to the likelihood that an α particle (two protons and two neutrons system) is already preformed within a nucleus before its emission, typically but not uniquely in α decay. α particles are doubly magic and strongly bound with a binding energy of 28.3 MeV, making them an efficient way of reducing energy in a system and forming clusters inside the nucleus. Theoretical models, such as the liquid drop model or microscopic cluster models, are often used to compute the preformation factor by comparing experimental decay energies with calculated emission probabilities. The preformation factor for α particles can range from 10^{-2} to 10^{-1} in nuclei near $N = Z$ as reported in the study of Ref. [100].

Deuteron preformation

Deuteron preformation refers to the probability that a deuteron (a bound state of a proton and neutron) is already formed inside a nucleus before being emitted. Unlike α-decay, deuteron emission is mostly known in the context of fusion-evaporation processes. Deuteron preformation differs significantly from α particle preformation due to its lower binding energy of only 2.22 MeV and weaker clustering within the nucleus. This relatively low binding energy makes it more susceptible to disintegration under higher excitation energies.

6.3 Experimental analysis

A list of reaction channels with evaporated particles including either a deuteron or proton-neutron pair considered for the study is presented in Table 6.1. ^{61}Zn has one of the largest cross-sections to be created for the ^{40}Ca and ^{24}Mg beam-target combination. Thus, it is a prime candidate for the studies. Since ^{53}Fe and ^{49}Cr are also present in $2pn$ data from the contamination reaction of ^{40}Ca on oxygen and carbon build-up, it is interesting to compare the three nuclei. Other interesting study cases involve $3pn$ and αpn channels. However, only ^{60}Cu and $N = Z$ ^{58}Cu residues from ^{64}Ge compound reveal sufficient statistics in the dataset.

Table 6.1: Evaporation channels (first column) from the three compound nuclei (second column) and residual nucleus (third column) considered for deuteron evaporation studies. The last column indicates whether the reaction channel was found in the experimental dataset with sufficient statistics.

Evaporation channel	Compound	Residue	Status
$2pn$ or dp	^{52}Fe	^{49}Cr	present
	^{56}Ni	^{53}Fe	present
	^{64}Ge	^{61}Zn	present
$3pn$ or $d2p$	^{64}Ge	^{60}Cu	present
αpn or αd	^{52}Fe	^{46}V	not present
	^{56}Ni	^{50}Mn	not present
	^{64}Ge	^{58}Cu	present

6.3.1 Individual reaction channels analysis

A comparative study of d vs. pn evaporation was carried out individually for each of the following nuclei: ^{49}Cr, ^{53}Fe, ^{58}Cu, ^{60}Cu, and ^{61}Zn. In the experimental data, reaction channels of interest were selected event-by-event by identifying the appropriate combination of evaporated particles and γ-ray coincidences. Once a reaction channel was assigned to an event, the kinematic correction was computed according to Sec. 3.4.2. Due to the significant mass differences among the studied recoils, separate correction parameter sets were used for each recoil to ensure accurate calculations. Based on these parameters, Doppler corrections were applied to the γ rays associated with each event. Additionally, since the energies of evaporated particles could provide valuable insights, the kinematic correction procedure was also used to determine the center-of-mass energies of each evaporated particle, as detailed in Sec. 4.2.2. For deuterons and α-particles detected with the DSSDs, energy corrections for absorbers were performed similarly to the procedure for protons outlined in Sec. 4.2.1.

The analysis of each nucleus relied on $\gamma\gamma$ and particle coincidences. For this, two $\gamma\gamma$ matrices were generated for each recoil: one involving a d coincidence, and another one including a pn pair instead. Since evaporated deuterons could only be identified using the DSSDs, to ensure a fair comparison between the d and pn channels, the creation of the pn $\gamma\gamma$ matrix also required the detection of a proton only with the DSSDs. Also, due to difficulties in neutron data acquisition (see Sec. 3.2), the statistics in the γ spectra significantly decreased when requiring neutron detection. To address this issue, an additional $\gamma\gamma$ matrix was created for the pn channels without neutron detection requirement, placing significant emphasis on thorough analysis of $\gamma\gamma$ coincidences for accurate channel identification.

Detailed evaporated particles-γ coincidence analysis for each reaction channel was done and ratios of the ratio of yields, $R(\frac{Y(d)}{Y(pn)})$ were calculated. These are presented and discussed in detail in Paper V. In the following, additional comparative studies of deuteron evaporation among the nuclei are explored.

6.3.2 Excitation energy of compound nuclei

Knowing the excitation energy of the compound nucleus is crucial for studying evaporation processes since it directly determines the available energy for particle emission, which influences the types and probabilities of particles that are emitted during the decay. This available excitation energy can be calculated as well as measured using experimental observables.

Calculation through reaction kinematics

One way of estimating the nuclear excitation energy is simply through reaction kinematics. Starting with linear momentum conservation between beam and compound nucleus:

$$p_b = p_c, \tag{6.7}$$

where p_b and p_c are the momenta of beam and compound nuclei, respectively, in the laboratory reference frame. From this, we can rewrite it as:

$$m_b E_b = m_c E_c, \tag{6.8}$$

where m is the mass and E is the kinetic energy. From this, the kinetic energy of the compound can be derived as:

$$E_c = \frac{m_b}{m_c} E_b \simeq \frac{A_b}{A_b + A_t} E_b, \tag{6.9}$$

where A_b and A_t denote the mass numbers of beam and target nuclei respectively.

Finally, the excitation energy of the compound, E_c^* can be calculated as:

$$E_c^* = E_b - E_c + Q, \tag{6.10}$$

where Q is the amount of energy released during the reaction.

Following the previous derivations, the excitation energies for the three compound nuclei were calculated, with the results shown in Fig. 6.1. With a ^{40}Ca beam energy of 106 MeV, reactions with ^{12}C and ^{16}O contaminants resulted in excitation energies of 37 MeV for ^{52}Fe and 44.6 MeV for ^{56}Ni, respectively. Since the fusion-evaporation reaction in the ^{24}Mg target is assumed to occur at the midpoint of the foil, the beam loses about 5 MeV, leading to an excitation energy of 43 MeV for the ^{64}Ge compound. These excitation energies are crucial for estimating the available energy in reaction channels of interest.

Nuclear thermodynamics description

The thermodynamic description of nuclear level density, ρ, can also be applied to experimentally determine the excitation energies of the compound nuclei.

Starting with the following expression:

$$\rho_{CN}(E^*) \propto e^{\frac{E^*}{kT}}, \tag{6.11}$$

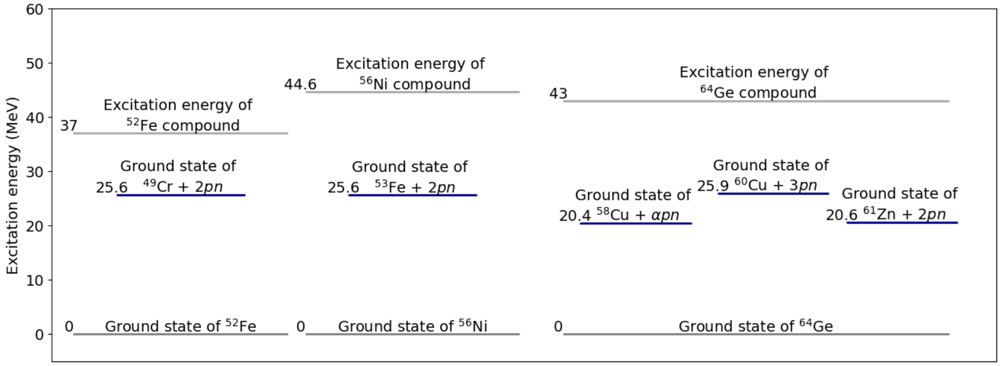

Figure 6.1: Excitation energies of compound nuclei in exp1582 plotted in relation to their ground state. Ground-state energies of several reaction channels are plotted with respect to the ground states of their compound nuclei.

where ρ_{CN} is the nuclear level density of the compound nucleus, E^* is the excitation energy of the compound, k is the Boltzmann constant, and T would represent nuclear temperature.

Since the evaporated particles were measured during experiments, their kinetic energy information is available. To calculate the excitation energy of the compound nucleus from the energy spectrum of evaporated particles, a Maxwell-Boltzmann distribution is typically fitted to the spectrum to extract the nuclear temperature, T. The energy distribution of evaporated particles is expected to follow:

$$N(E) \propto E \cdot e^{-E/T}, \tag{6.12}$$

where E is the energy of evaporated particle, $N(E)$ is the number of evaporated particles at energy E.

Once the nuclear temperature T is known, the excitation energy E of the compound nucleus can be calculated using the Fermi-gas model relation:

$$E = aT^2, \tag{6.13}$$

where a is the level density parameter. This parameter is often approximated as

$$a \approx A/10, \tag{6.14}$$

with A being the mass number of the compound nucleus [71].

This approach allows the excitation energy to be estimated from the measured proton spectrum, providing a crucial connection between experimental data and theoretical nuclear models.

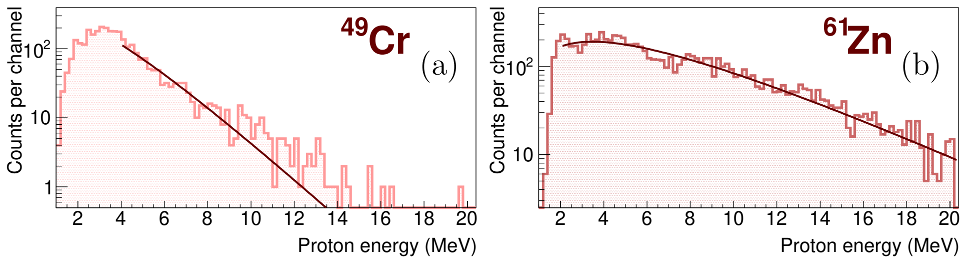

Figure 6.2: Evaporated proton spectra from dp reaction channels of ^{52}Fe (a) and ^{64}Ge (b) compound nuclei resulting in ^{49}Cr and ^{61}Zn respectively. Proton energies are computed in the center-of-mass frame. Lines show Maxwell-Boltzmann distribution fitted to the spectra. Background removed from spectra, see text for details.

Evaporated proton energies in the center-of-mass reference frame associated with the dp channels of ^{52}Fe and ^{64}Ge compound nuclei are presented in Fig. 6.2 panels (a) and (b), respectively. To select ^{61}Zn residues, a coincidence with a 124-keV γ ray was required. For ^{49}Cr a more strict condition of a $\gamma\gamma$ coincidence between the 812-keV and 272-keV cascade was applied. Fitting a Maxwell-Boltzmann distribution to the spectrum in Fig. 6.2(a) results in $T(^{52}\mathrm{Fe}) =$ 1.42(5) MeV. One can utilize this value together with the computed excitation energy of the ^{52}Fe compound nucleus to deduce the level density constant from Eq. 6.13. For ^{52}Fe one obtains $a_{exp}(^{52}\mathrm{Fe}) \approx 20$, while $a \approx 5$ using Eq. 6.14. Applying the same fitting procedure to the ^{61}Zn case results in $T(^{64}\mathrm{Ge}) =$ 3.48(3) MeV. This leads to $a_{exp}(^{64}\mathrm{Ge}) \approx 5$. This is close to the expected $a \approx$ 6. The result for ^{64}Ge obtained with the γ-gated proton thermometer is in good agreement with the commonly used value for the level density parameter. However, it is important to note that different approximations for the parameter can be used, and $a \approx A/10$ is only an approximation. From the experimental point of view, it is difficult to study the reaction mechanism on a more precise level due to experimental limitations. For instance, the fit is highly sensitive to the fitting range as well as the tail end of the distribution, which corresponds to the high kinetic energies of particles, in this case, protons. The energies of those particles are not fully detected but rather reconstructed based on partial energy depositions in the Si system. Nevertheless, this attempt represents a different way of investigating nuclear reactions, i.e., using the nuclear thermodynamics approach while involving particle-γ coincidences.

6.4 Common trends

Instead of focusing on the individual production rates through deuteron evaporation for the nuclei ^{49}Cr, ^{53}Fe, ^{58}Cu, ^{60}Cu, and ^{61}Zn, the next step is to explore common trends across the different reactions. To achieve this, it is necessary to find a meaningful way to compare the different nuclei. One approach is to examine the spectra of evaporated particles, which can provide insight into the underlying patterns. Additionally, it is valuable to plot the yields of each reaction as a function of the available excitation energy, offering a broader perspective on how these energies influence deuteron evaporation across the different nuclei.

6.4.1 Energies of evaporated particles

Correlation matrices where evaporated proton energies are plotted vs. evaporated deuteron energies for *dp* channels from ^{52}Fe and ^{64}Ge compound nuclei leading to the production of ^{49}Cr and ^{61}Zn are presented in Fig. 6.3. To identify the recoils, 272-keV and 124-keV γ-ray coincidences are required when filling ^{49}Cr and ^{61}Zn matrices, respectively. Similarly, background matrices were prepared by selecting coincidences with γ energies just outside the main peaks. Projections of the matrices yield proton and deuteron spectra associated with the reaction channels, from which the respective backgrounds have been removed. Since the measured proton and deuteron energies are transformed from the laboratory frame to the center-of-mass frame, the spectra from the two nuclei can be directly compared.

According to Fig. 6.1, about 13 and 25 MeV of energy are available for particle evaporation and γ emission for the ^{49}Cr and ^{61}Zn reaction channels, respectively. Note that the energies already account for the extra 2.2 MeV of deuteron binding energy available for evaporation. Given the available phase space, it is expected that protons and deuterons associated with ^{61}Zn will exhibit higher energies in comparison to ^{49}Cr ones. This is evident when comparing E_pE_d matrices for the channels [Fig. 6.3(a)-(b)]. The same conditions were applied to identify ^{49}Cr and ^{61}Zn as previously described for Fig. 6.2.

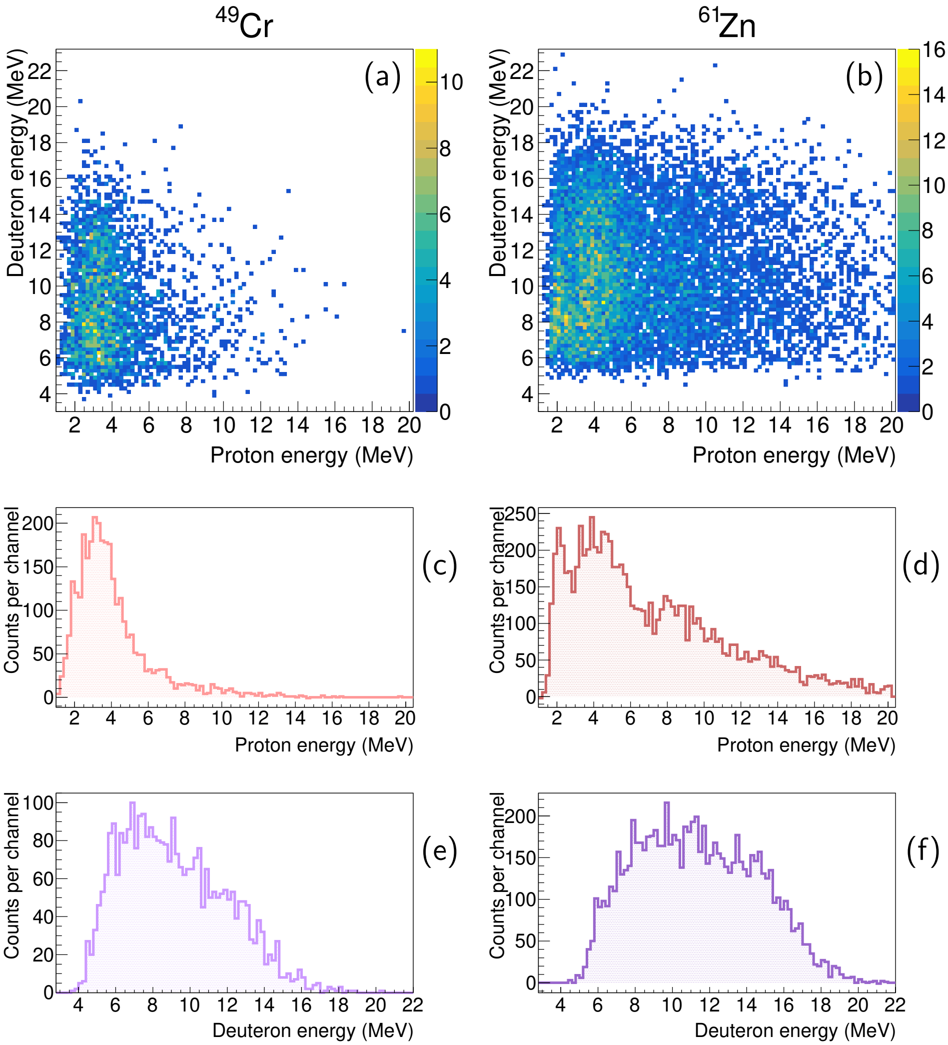

Figure 6.3: Proton-deuteron energy matrix plotted for dp evaporation channels of ^{53}Fe and ^{64}Ge resulting in ^{49}Cr (a) and ^{61}Zn (b), respectively. X- and Y- projections correspond to proton and deuteron energy spectra in the center-of-mass frame [(c)-(f)]. The background is removed for the projected spectra, see text for details.

Examining the evaporated proton energy distribution for ^{49}Cr (Fig. 6.3(c)), two observations can be made. First, the majority of evaporated protons have about 3-4 MeV of energy. Second, the energy distribution ends at about 13 MeV, which is consistent with the total available energy for evaporation. In the ^{61}Zn evaporated protons spectrum, Fig. 6.3(d), several peak-like structures are visible. This could be attributed to residual background in the lower energy part of the spectrum potentially signifying a need for more strict recoil selection, not feasible

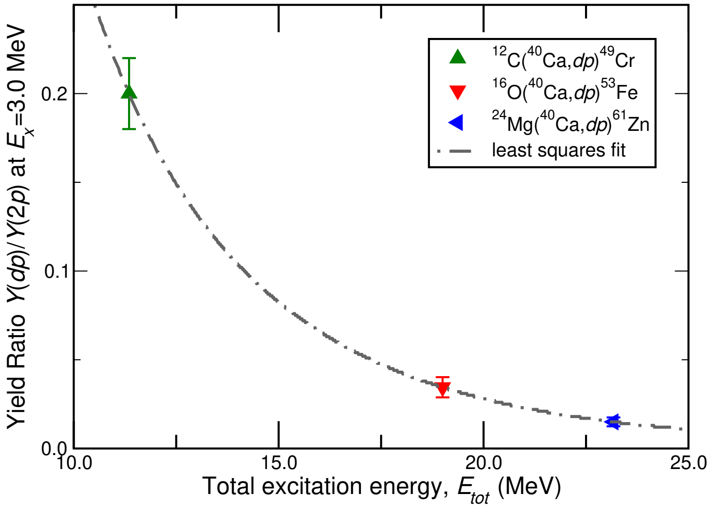

Figure 6.4: Experimental ratio of yields, $Y(dp)/Y(2p)$, computed at 3 MeV excitation energy, E_x, for $2pn$ reaction channels ^{49}Cr, ^{53}Fe, and ^{61}Zn as a function of total excitation energy, E_{tot}, available for particle evaporation and γ emission. This figure is reproduced from Paper V.

with the present level of statistics. It can be noted that during the background subtraction procedure for the ^{61}Zn spectrum, the majority of the background also fell below 6 MeV, with a similar shape as ^{49}Cr.

Examining the evaporated deuteron energies in Fig. 6.3(e) associated with ^{49}Cr it is evident that the distribution ends at around the expected 15 MeV. The higher energies observed for deuterons associated with ^{61}Zn [Fig. 6.3(f)] are consistent with the greater amount of energy available in this system.

6.4.2 Excitation energy

Ratios of yields $Y(dp)/Y(2p)$ as a function of excitation energy for each of the reaction channels are presented in Paper V. The values for each nucleus were extracted from their respective fits at $E_x = 3$ MeV and plotted as a function of the total available excitation energy, denoted E_{tot}. The results are also presented in Fig. 6.4. The total available excitation energy for each reaction is computed as the difference between the excitation energy of the compound nucleus and the ground state energy of the resulting nucleus, as shown in Fig. 6.1. Since ^{49}Cr, ^{53}Fe, and ^{61}Zn are created as a result of $dp/2pn$ evaporation, those nuclei can be directly compared. However, ^{58}Cu and ^{60}Cu, which are products of $d2p/3pn$ and $\alpha d/\alpha pn$ evaporation, respectively, cannot be directly included in this comparison.

Fig. 6.4 reveals that as the excitation energy available to the system increases, single-particle emissions become more probable, while deuteron evaporation dominates at lower excitation energies. This behavior can perhaps be attributed to deuteron preformation factors, indicating that at higher excitation energies, the energy exceeds the one of the deuteron binding, which increases the likelihood of the bond breaking and the nucleons being emitted individually. For further discussion, see Paper V.

6.5 Conclusions

This study marks the first clear in-beam identification of deuteron evaporation using a setup specifically designed to enable γ-ray coincidence analysis, providing unprecedented insights into deuteron production in fusion-evaporation reactions. The results indicate that deuteron evaporation is not linked to the proximity of nuclei to the $N = Z$ line, but rather to the available excitation energy in the system. This finding redirects the emphasis from examining nuclear structure to analyzing the mechanisms of nuclear reactions in the context of deuteron production. Major results of the study along with theoretical considerations are the subject of Paper V.

Future analyses could extend this work by including nuclei from the other compound nuclei produced in the first and third experiments of the ANL campaign while applying similar methods to further explore the role of excitation energy in the deuteron evaporation mechanism and refine our understanding of the underlying mechanisms.

Chapter 7

Concluding remarks

Exploring nuclei that are progressively further from the line of stability reveals increasingly unstable systems that decay through rare modes. Gaining deeper insights into these decays requires enhancing the sensitivity of experimental setups. This can be accomplished by developing more advanced detectors with higher efficiency, granularity, and resolution alongside advancements in modern digital electronics, thereby optimizing signal processing. As we venture into the outskirts of the nuclide chart, the complexity of these experimental setups grows, frequently requiring a wide array of detectors of various types, or detector readout channels with intricate triggering conditions. This thesis focuses on two experimental setups: the upgrade of locally designed and maintained Compex Ge-detector modules with anti-Compton shields for γ-spectroscopy and the advanced ANL Gammasphere setup with the addition of Lund's silicon detectors aiming at in-beam charged particle-γ coincidence spectroscopy. Both setups are designed and employed to study rare decays, with only a few available worldwide capable of such tasks. The concluding remarks presented in this chapter are related to the implementation of the anti-Compton shield for Compex detectors and their future use. The research findings obtained employing the ANL setup are summarized below, along with suggestions for future research directions.

The upgrade of the five Compex Ge detectors with active anti-Compton shields makes the system of detectors an ideal tool for γ-ray spectroscopy of rare decays occurring at rest. The ACS pockets, made from BGO detectors, were specifically designed and tested in combination with a Compex detector. These pockets maintain the versatility of Compex detectors. The full pocket design is suitable for single-detector applications, and the corner pocket design is perfect for tight configurations using four Compex detectors, such as in a future Lundium chamber or wall configuration. The performance of the full BGO shield, tested with a Compex detector, demonstrated up to 70% improvement in the peak-to-total ratio of the 662-keV ^{137}Cs peak. The thesis also highlights the critical role of specialized digitizers, along with dedicated front-end readout algorithms for detector signal processing, in achieving optimal detector readout performance. Measurements confirmed the reliability of the VME-based DAQ for Ge-detectors, with the future transition to FEBEX4 cards planned. Presently, a Compex-ACS-DSSD combination has been set up locally for environmental filter sample measurements employing the γ-α coincidence technique. This is an example of taking the next step for the kind of studies presented in Ref. [101]. Future applications of the Compex detector array with their respective shields include their use behind various decay stations at different accelerator facilities, such as the future GSI FAIR facility [102]. Prior to that, starting 2025, they are expected to be part of setups used for superheavy research [103, 104] at Lawrence Berkeley National Laboratory.

An experimental campaign focusing on isospin-symmetry and proton emission in the upper *fp* shell was performed at ANL in 2020. Owing to the setups in-beam proton spectroscopy and tracking capabilities, a coincidence between a 957.6(5)-keV γ ray and a 1876(24)-keV proton line in ^{61}Ga was observed. The resolution of the proton peak in the experiment is much improved from its predecessors [47, 105] due to a more precise definition of the recoil vector, owing to the setup's tracking capabilities and including beam-spot on target estimation. In addition, the first results of the experimental measurement of the angular distribution of prompt protons were presented. The complexity of the experimental setup remains unrivaled for this type of study. Future experiments aiming at prompt proton spectroscopy could built on experimental experience and technique presented in this thesis. In the near future, benchmarking of prompt proton lines in ^{57}Cu [1, 41] and a search for predicted proton emission in ^{65}Ar [106] as results of the first and third experiments in the campaign are pending. Further improvements in proton spectroscopy resolution could be achieved by optimizing the combination of DSSD's thicknesses for optimal mass resolution power combined with high tracking capabilities. Neutron detectors also play a critical role in clean fusion-evaporation channel selection, and recent upgrades to their data acquisition system at ANL aim to resolve synchronization issues in future experiments. Continued advancements in data processing algorithms, including machine learning techniques for extracting physics-related information utilizing pulse-shape analysis, could significantly streamline the analysis process and reduce, for instance, the amount of background in various types of projected particle- and γ-ray spectra.

This newly identified proton line corresponds to the quasi-bound proton $\pi g_{9/2}$ single-particle state in ^{61}Ga at E_x=2150(34) keV and probes isospin-symmetry breaking in the upper fp shell by means of mirror-energy differences. The JUN45 shell-model interaction ($f_{5/2}pg_{9/2}$ space) expanded with isospin-breaking terms provides a very good description of the measured MED in the $T_z = \pm1/2$, $A = 61$ mirror pair. The interaction is planned to be further tuned for a better description of the neutron-deficient nuclei in the upper fp shell. Future spectroscopy experiments beyond the proton drip line will further consolidate these efforts. For example, analyzing the first and third experiments of the campaign using the same techniques as presented in the thesis is envisioned as the next step, focusing on revising proton spectroscopy from excited states in ^{57}Cu [1, 41] and identifying more excited states in ^{65}As [107]. These new experimental data will help refine shell-model calculations and contribute to an improved theoretical description of nuclei with neutron number close to the proton number, just above the doubly-magic nucleus ^{56}Ni.

Owing to the light-charged-particle sensitivity of the setup, deuteron evaporation was observed from the $N = Z$ compound nuclei ^{52}Fe*, ^{56}Ni*, and ^{64}Ge*. Results were interpreted using a statistical evaporation formalism for multiple subsequent particle emissions. The study allowed to gain additional insights into the fusion-evaporation process. The study gives the first valuable experimental points to refine the description of fusion evaporation involving deuterons. For instance, it could be included in modern evaporation codes. Since there were two more experiments from the campaign employing the same setup, more compound nuclei and their residuals could be studied to compare with the original conclusions.

The findings presented in the thesis emphasize the critical significance of advanced experimental setups and detector technologies capable of providing a comprehensive view of observables in the exploration of rare decays and exotic nuclei. The results from this thesis provide valuable experimental data points for refining current theoretical nuclear models.

Appendix A: CD-DSSD detectors

This appendix provides technical details on the wafers of the CD-DSSD detectors used in the ANL experimental campaign. Two types of wafers for the DSSD detector construction were employed, differing in thickness and inner opening. The DSSD1 is a 300 μm thick silicon detector with a 14 mm inner active diameter. The rings vary in size, with the width of the inner rings increasing to ensure uniformity in area across all rings. A technical sketch of DSSD1, showing the design of the rings and sectors, is presented in Fig. A.1. In contrast, the wafer of DSSD2 has a thickness of 525 μm and an inner opening of 28 mm, featuring equidistant rings. A technical sketch of the DSSD2 design is provided in Fig. A.2.

Table A.1 lists the technical specifications provided by RADCON Ltd., the manufacturer of the DSSD wafers, including key parameters such as leakage current, resolution, and noise levels for a standard test with all sectors and rings connected as measured by the company for the factory acceptance tests. The results are shown for the DSSD2 type detector.

Table A.1: Technical specifications for CD-DSSD2 detector wafer [108].

Interstrip distance	110 μm
Thickness	0.525 +/- 0.010 mm
Leakage current	20 nA/sector
Capacitance	15.2 pF/sector
Specific resistivity	$>$ 12.0 $k\Omega\cdot$ cm
α resolution (at 5.485 MeV)	25 keV/sector
Noise level (measured with ORTEC4IZBI)	$<$ 14.0 keV/sector
Tested under vacuum	$\leq 10^{-6}$ mm Hg

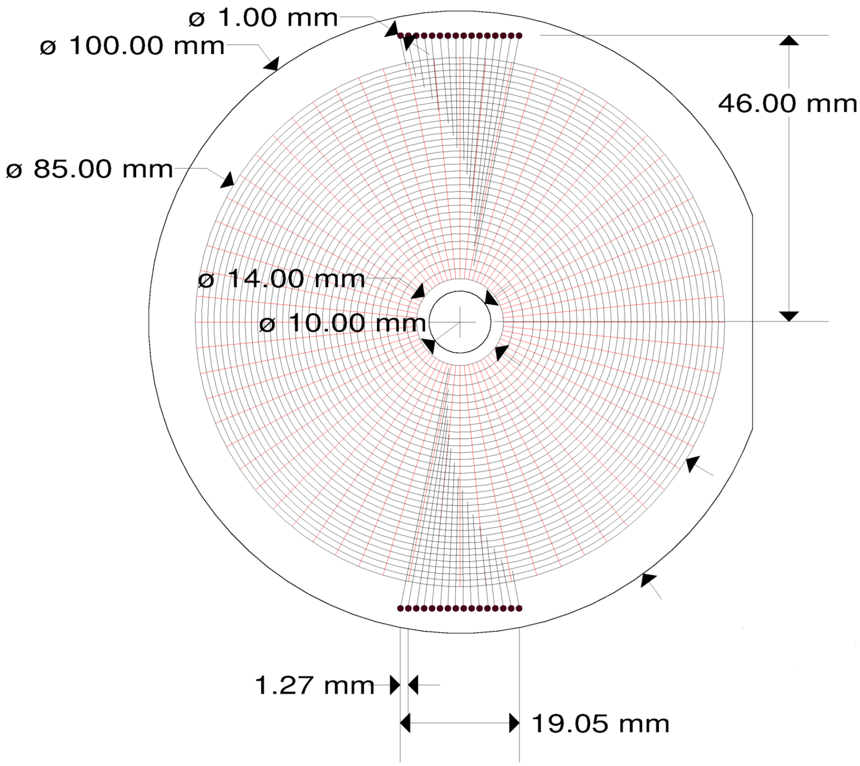

Figure A.1: Technical sketch of the wafer for DSSD1. The wafer is divided into 64 segments and 32 rings, highlighted in red. The inner physical diameter is 10 mm, and the outer physical diameter is 100 mm. The active area has inner and outer diameters of 14 mm and 85 mm, respectively. The widths of the rings, from inner to outer, are as follows: 3 × 1.6 mm, 4 × 1.2 mm, 9 × 1.1 mm, and 16 × 1.0 mm.

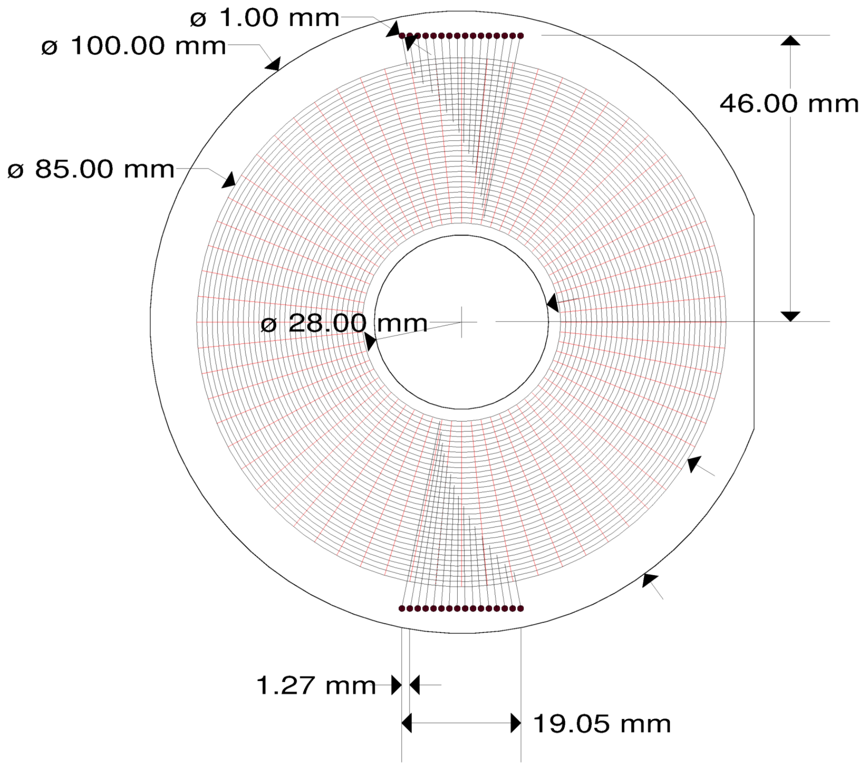

Figure A.2: Technical sketch of the wafer for the DSSD2. The wafer consists of 64 segments and 32 equidistant rings, highlighted in red. The inner physical diameter is 28 mm, while the outer physical diameter is 100 mm. The active area has inner and outer diameters of 28 mm and 85 mm, respectively. The width of the rings is consistently 1.66 mm from inner to outer.

Appendix B: Data recovery

The experimental campaign had a very complex setup with three data acquisition systems as presented in Sec. 3.2.1. Running the three data acquisition systems simultaneously posed numerous challenges during the experiments, especially under the restrictive Covid-19 conditions. Some issues became clear only during the offline processing of data after requiring additional correlations among different detector systems. In this appendix, attempts for various data recovery are presented. In Sec. B.1, a successful recovery of correlations from multiple detectors connected to the DFMA DAQ with the DGS DAQ is presented. Issues with the neutron synchronization are presented in Sec. B.2. Finally, the correction of partially missing signals from the DSSDs is given in Sec. B.3.

B.1 DFMA DAQ

During the second experiment (exp1582), it was observed that the PPAC detector in the focal plane of the FMA was occasionally not synchronized with Gammasphere. This was noted during the online monitoring of the experiment. The problem was traced to Router 5, a hardware clock for two digitizers, IOC10 and IOC11, which handled PPAC signals. Router 5 was replaced at the end of exp1582, resolving the problem for the rest of the experimental campaign.

During offline investigation, it was revealed that Router 5 issues started already at the very beginning of the first experiment, exp1239. The hardware failure in Router 5 led to partial corruption of timestamps in data written by IOC10 and IOC11. Focal plane data, part of Microball detectors as well as neutron detectors traces were recorded by IOC10 and IOC11 in DFMA in addition to WuDAQ. Remarkably, despite corruption, some timestamps were still recorded, allowing for potential recovery. It was especially critical for the focal plane data since proper timing coincidences are necessary for later A/Q requirements.

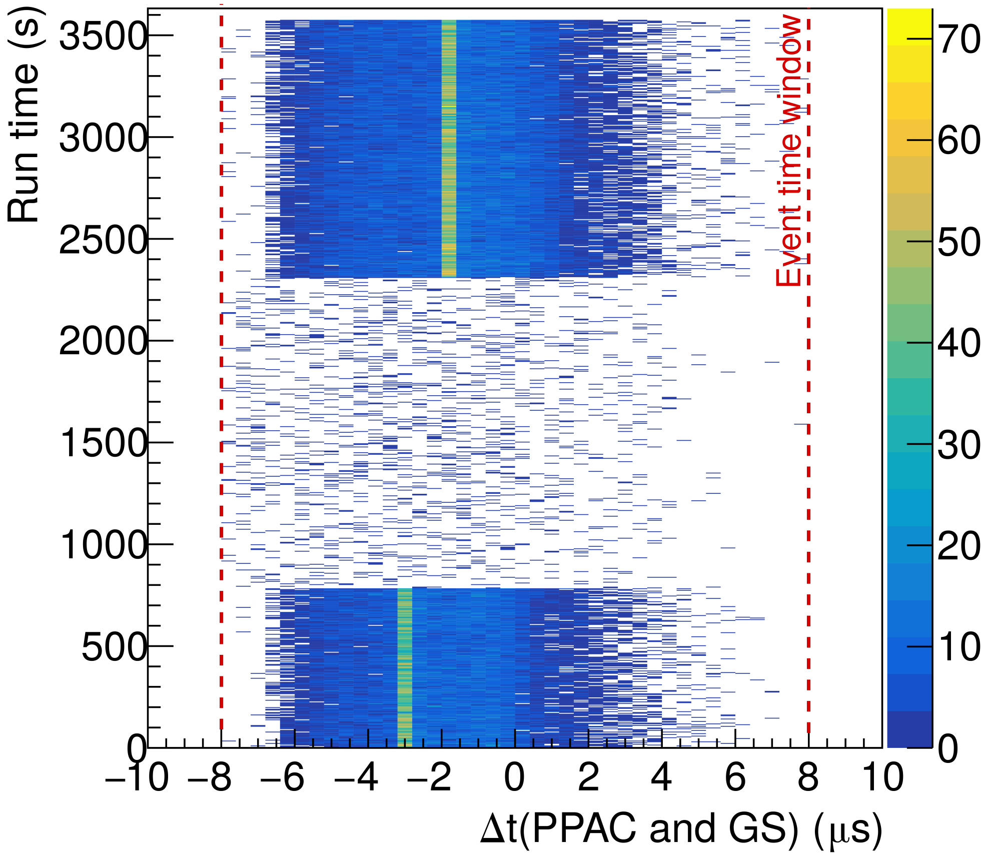

Figure B.1: Time correlation plot of the PPAC detector with Gammasphere showing a problem with corrupted timestamps. Time differences in PPAC and Gammasphere timestamps are plotted as a function of the experimental run time. The experimental event window is 8 μs. For details see text.

Before starting further data analysis, it was decided first to attempt to recover the corrupted data.

It was found that the corrupted timestamps had a bit error that occurred during timestamp reception and resulted in writing data by IOC10 and IOC11 with occasionally bitwise corrupted timing. This is visible in Fig. B.1 presenting PPAC and Gammasphere time correlations as a function of run time for one about one-hour long run from exp1239. About 14 min after the start of recording the run, Router 5 started malfunctioning. The issue was extremely hard to spot during online monitoring since data for the entire run had to be checked to notice it. Furthermore, what also made it difficult to realize is that after malfunctioning the timestamps would go back to normal as is also seen in Fig. B.1. Nevertheless, despite issues, the timestamps were still written even though lacking coincidences with Gammasphere. It was then concluded that the coincidences were missing inside the selected time window of 8 μs. Thus, the subevents recorded with IOC10 and IOC11 would fall in and out of this event window.

The event window had to be increased to find how large the shifts were. Time correlations with a new event window of 6 ms for a run in the middle of exp1582 are presented in Fig. B.2(a). Note that with a large event window, meaningful coincidences become less prominent when overwhelmed by background. Thus, Neutron Shell traces, which were also written by IOC10 and IOC11, were used for the identification of shifts for better statistics. As observed in Fig. B.2(a), the jumps in timestamps correspond to multiples of 65536, thus multiples of 2^{16}. The shifts are of the order of several ms, which makes them much larger than the original 8-μs event window. It was then realized that the shifts could be even larger than the new 6 ms window, which was important to investigate. However, it is not feasible to open the event window further due to the rising number of random coincidences. Thus, for the areas missing coincidences in the first iteration, the timestamps were shifted by 2^{20}. The result is shown in Fig. B.2(b). It is clear that additional shifts corresponding to 2^{20} and $2^{20} + 2^{18}$ have to be accounted for during the recovery of data as well.

The comment from J.T. Andersson, who is the DAQ electronics expert at the ATLAS facility, regarding the observed shift was as follows: "The observed jumps in the timestamp at multiples of 65536 are consistent with SERDES data reception issues, as this aligns with the 16-bit word boundary for timestamps transmitted from the master trigger to the router. The router's timestamp counter typically counts continuously, but it resets when the state machine monitoring the SERDES data detects synchronization and decodes a Sync command, at which point the counter adopts the timestamp received from the master trigger. Router 5 experienced significant data reception problems due to connector issues, causing the SERDES reception state machine to latch onto incorrect data if a bit error occurred during timestamp reception. In cases of severe connection instability, where the link dropped in and out at high frequencies (kHz), the external clock multiplexer (mux) chip would frequently switch between the local and external clocks. This could result in the clock stopping for brief periods, disrupting the router's operation."

It was decided to shift the corrupted bit in timestamps to the expected positions. For this, a so-called look-up table was created for each file. The table contained regions for which the timestamps need to be shifted and the respective values for shifting, i.e., 2^{16}, 2^{17}, etc. To produce the table, two iterations of analysis were used. First, data was sorted with the 8-ms window with NS and Gammasphere

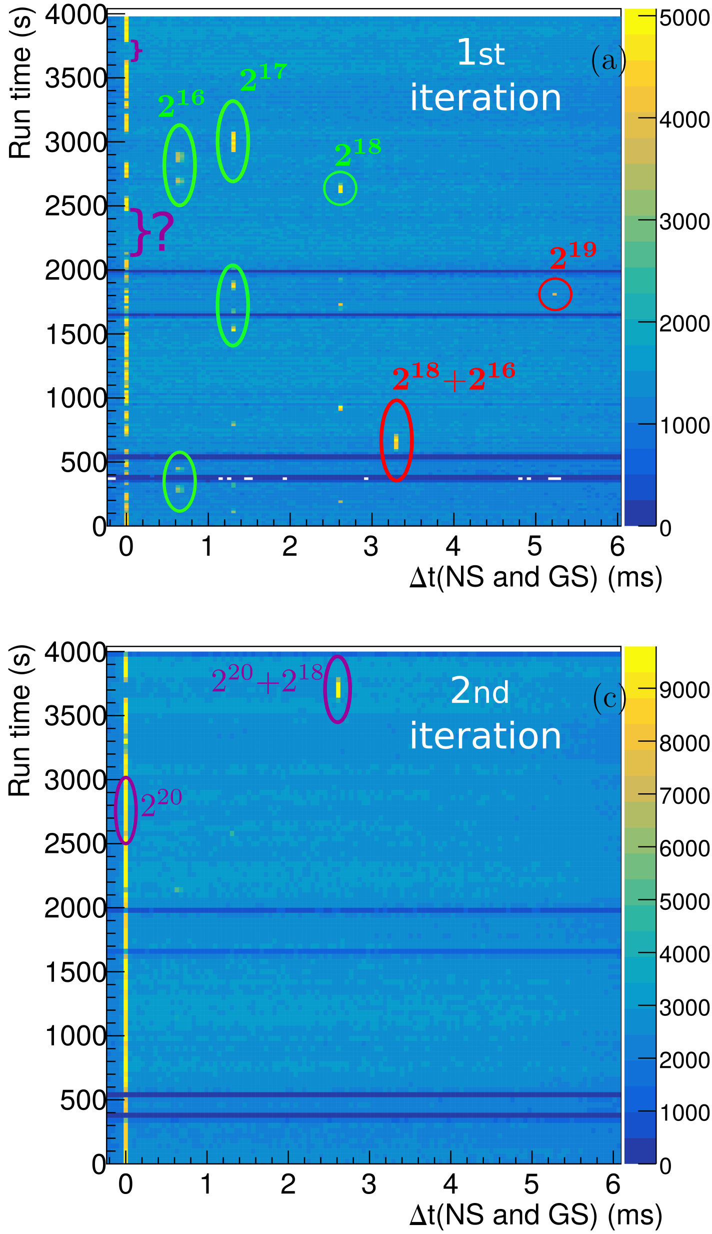

Figure B.2: Time correlation plots of Neutron Shell detectors with Gammasphere showing shifts in timestamps. Panel (a) shows the first iteration of the search for timestamp shifts with a 6 ms time window. Shifts are highlighted with different colors. The region with missing correlations in the 1st iteration is indicated with a purple question mark. Panel (b) shows the regions that were not identified in the first iteration (purple questions mark) shifted by 2^{20} (purple circles). This enables to identify even larger shifts. For details see text.

time coincidence correlations into 2D histogram. Later, Y-projections around expected shift regions were analyzed with a separate root script. If significant numbers of counts were found in a projected histogram, the region with the shift was written. The original GEBFilter [54] program was then used to modify the timestamps and shift them into the expected state. Additionally, one otherwise unused bit in the timestamps was used to indicate that the data was modified. The unpacking of data procedure in GEBSort was then also modified to read in the special timestamps and check the bit to save the information into a flag if the sub-event contains a timestamp that was modified.

Typical results of the recovery for runs from exp1239 and exp1582 are presented in Fig. B.3. Panels (a)-(d) present PPAC and Gammasphere time correlations as a function of run time for exp1239 [panels (a) and (b)] and exp1582 [panels (c) and (d)]. For runs in exp1239, the recovery would involve shifting timestamps in relatively large chunks of data as it is seen in panels (a) and (b) corresponding to before and after the modification, respectively. Panel (c) shows a run towards the end of exp1582, with quite intense change in timestamps dropping in and out of the time window. The result of the recovery is shown in panel (d). It is prominent that the issue became more severe in exp1582 with Router 5 dropping at high frequencies. The projections of the histograms are shown in panels (e) and (f) for exp1239 and 1582, respectively. The recovery process for exp1582 was significantly more complicated since the frequency of changes in timestamps could be even smaller than one second of run time. Thus for the runs toward the end of exp1582, the recovery procedure had to be adjusted and tailored towards looking towards very frequent changes.

The recovery procedure was applied systematically for all runs, starting from the end of exp1582 towards the beginning of exp1239. In exp1582, 79 runs were corrected with the improvement in PPAC-GS timing correlations from 62% to 88%. The levels of recovery were measured based on a number of bins in projection as in Fig. B.3(c) over some threshold, for example, 10 counts. In the case of exp1239, 84 runs were corrected, with the correlation level rising from 42% to 90%. This result of recovery was deemed very important as the PPAC signals were used for the mass A requirement for channel selection, especially given the independent issues with the neutron data acquisition (see next Sec. B.2). A-selection was crucial, for instance, for identifying prompt protons in ^{61}Ga.

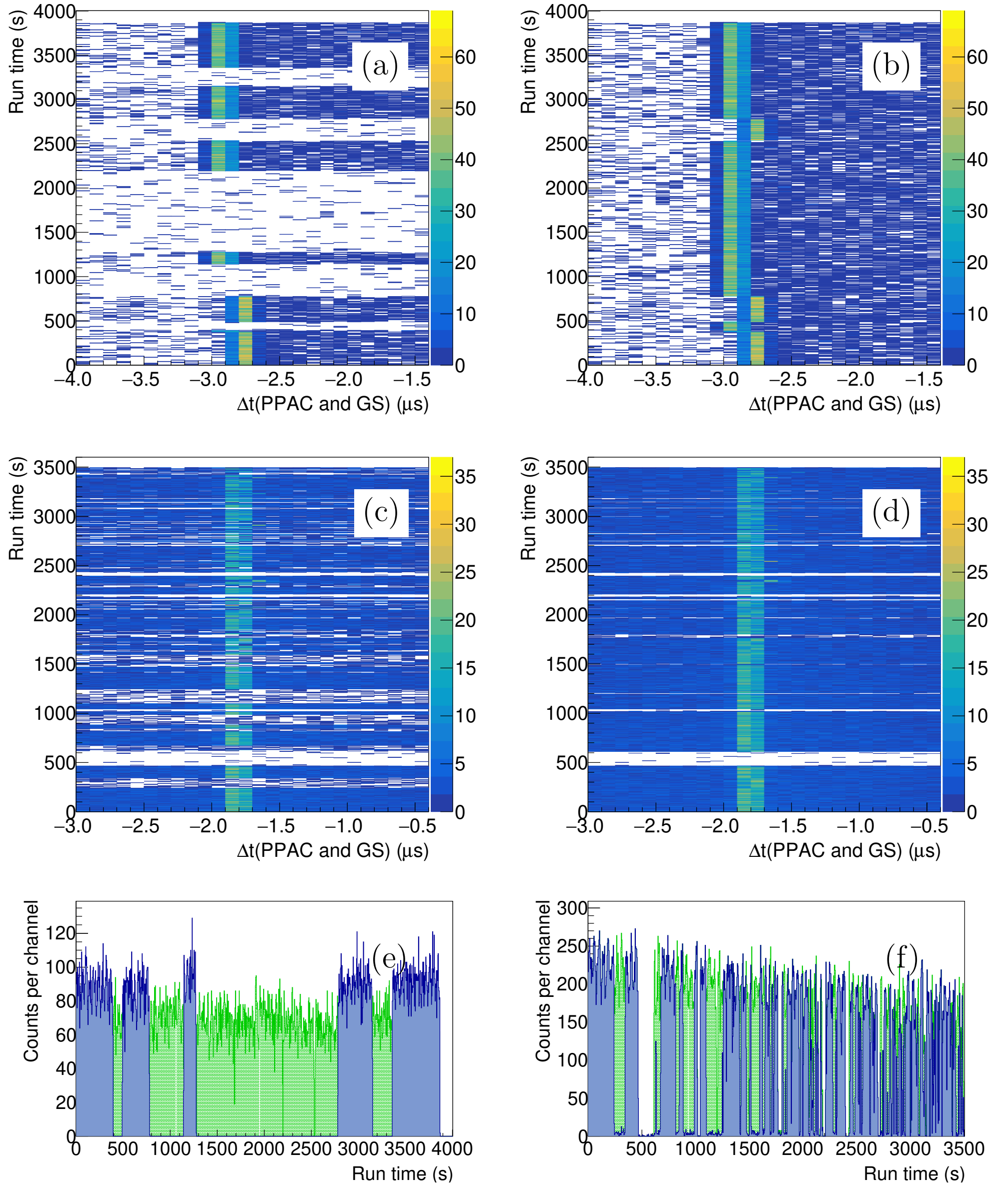

Figure B.3: PPAC-Gammasphere timing correlation plots as a function of run time showing the effect of the Router 5 data recovery procedure for runs selected from exp1239 and exp1582. The top panels show an experimental run selected from exp1239 before (a) and after (b) applying the procedure. Panels (c) and (d) are the same but for a run selected from the end of exp1582. Panels (e) and (f) show the projections of the coincidence regions for the runs from exp1239 and exp1582, respectively. Here, in blue is the projection before and additionally in green after applying the procedure. For details see text.

B.2 Neutron DAQ

Data from the Neutron Shell detectors at the beginning of the campaign was only recorded with the help of WuDAQ (Washington University DAQ). The system had a different trigger condition for fast timing as introduced in Sec. 3.2.1. Fast neutron timing is necessary for separating neutrons from low energy γ rays. Furthermore, it enables the neutron time-of-flight technique (see Sec. 3.4.1), which is used to estimate neutron energies.

During offline data analysis, after discrimination between neutrons and γ rays was completed and neutrons became available for detailed analysis, coincidences between Neutron Shell data containing neutrons and Gammasphere were investigated. It was then discovered that neutron detector statistics were way smaller than expected, i.e., only one out of eight events contained a γ sub-event and at least one neutron hit. This issue prevented the identification of γ rays from ^{62}Ge in the present dataset [48].

Under further investigation focusing on events containing neutrons, it was found that half of the recorded neutron data is not correlated with subevents from DGS hits. This means that WuDAQ was writing data unsynchronized to the main trigger system. An attempt was made to see if correlations could be restored. By plotting the time difference between uncorrelated neutron hits and previous events containing a Gammasphere hit, one can see if the data can be recovered. No correlations between those neutron hits and germanium hits were found. The reason for this was that there were two different trigger settings - neutrons require a fast trigger and thus WUDAQ was set up with three "dirty" Ge hits, while DGS and DFMA DAQs were set with "clean" germanium hit triggers, meaning that those uncorrelated neutrons events arise from the less strict trigger.

Based on some discussions during the campaign, neutron-detector signals were split and also digitized in traces in DFMA. Potential pulse-shape analysis of these Neutron Shell traces can be done to extract neutron data. However, the separation of neutrons and γ-rays might not be ideal, and the neutron time-of-flight technique would not be possible to use.

Recently, an upgrade was made at ANL, with two 16-channel digitizers containing a chip to be integrated into a homogeneous trigger system. Implementing fast-timing for neutron detectors still remains a challenge, since it requires a programmable delay to "wait" for the slower Gammasphere DAQ. Thus, synchronization remains a complicated and challenging process.

B.3 DSSD data recovery

The process of combining signals from the p- and n- sides of DSSD detectors into pixels is described in Sec. 3.3.4. At the end of exp1582, an adjustment of Si detectors electronics resulted in the partial loss of DSSD2 ring events, while sector signals were recorded regularly. To resolve this, a fourth stage of pixel creation was implemented with a special recovery for DSSD2. This is described below.

To assign ring numbers to hits in DSSD2, correlations with DSSD1 were used. The recovery was done for those events that contained information from DSSD1 and a hit in a p-side in DSSD2, but no n-side signal. If the sector hits in the system of DSSDs are correlated, i.e., correspond to a plausible particle trajectory, then a ring id in DSSD2 could be estimated based on a ring id in DSSD1. For this purpose, a mapping table was prepared, in accordance with correlations observed for a run without Si issues presented in Fig. B.4(a). It can be noted that given the geometry of the DSSD1 - DSSD2 system, DSSD2 covers the θ angle range corresponding to the first 14 rings in DSSD1. Based on the plot, ring ids in DSSD1 corresponding to each ring in DSSD1 were assigned. The result of the procedure is shown in Fig. B.4(b). Filled rings correspond to the average ring ids derived from the map and thus have a high number of counts.

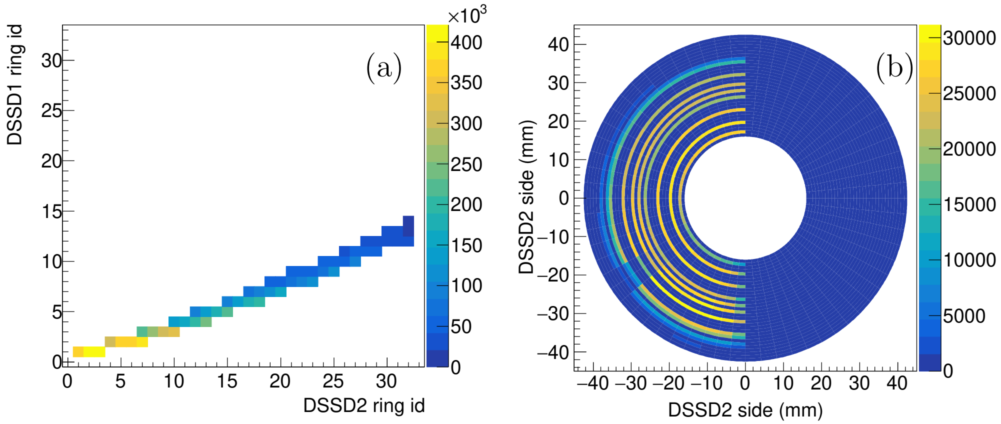

Figure B.4: (a) Correlations between rings in DSSD1 and DSSD2 detectors used for recovery of DSSD2 rings. (b) Result of the fourth-pixel creation procedure involving DSSD2 rings.

References

[1] Evaluated Nuclear Structure Data File (ENSDF), https://www.nndc.bnl.gov/ensdf/

[2] D.M. Cox, Phys. Rev. C **107**, L021301 (2023).

[3] A. Såmark-Roth, PhD thesis, Lund University, Sweden (2021).

[4] A. Såmark-Roth *et al.,* Eur. Phys. J. A **56**, 141 (2020).

[5] M.P. Carpenter *et al.,* Nucl. Instr. Meth. A **353**, 234 (1994).

[6] Ö. Skeppstedt *et al.,* Nucl. Instr. Meth. A **421**, 531 (1999).

[7] D. Rosiak *et al.,* Eur. Phys. J. A **55**, 48 (2019).

[8] Amcrys, Amcrys webpage, http://www.amcrys.com/

[9] 3M Enhanced Specular Reflector Film, Technical Data Sheet, https://www.3m.com/3M/

[10] Hamamatsu H1317U-1 series, Technical Data Sheet, https://www.hamamatsu.com/eu/en/product/optical-sensors/pmt/pmt-assembly/metal-package-type/H13175U-01

[11] Permacol RTV 615, Technical Data Sheet, https://permacol.nl/en/products/silicones/permacol-rtv-615/

[12] Fusion360, Fusion360 webpage, https://www.autodesk.com/products/fusion-360/

[13] D.M. Cox, to be submitted

[14] H. G. Essel & N. Kurz, IEEE Trans. on Nucl. Sci. 47, 337 (2000)

[15] J. Hoffmann, FEBEX3b specification (2013), https://www.gsi.de/fileadmin/EE/Module/FEBEX/febex3b

[16] I. Rusanov, User Manual: FEBEX 3 (A or B) as a Multifunctional Module, N. Kurz, private communication (2021).

[17] D. Rosiak *et al.,* Eur. Phys. J. A **55**, 48 (2019).

[18] GSI Exploder3, User Manual, https://www.gsi.de/en/work/research/experiment_electronics/data_processing/embedded_software/explodersoftware

[19] CAEN V785, User Manual, https://www.caen.it/products/v785/

[20] CAEN V775, User Manual, https://www.caen.it/products/v775/

[21] Struck SIS3302, User Manual, https://www.struck.de/sis3302.html

[22] D.M. Cox *et al.,* Phys. Rev. C **107**, L021301 (2023).

[23] MESYTEC MADC32, Technical Data Sheet, https://www.mesytec.com/products/nuclear-physics/MADC-32

[24] GSI VULOM1, User Manual, https://www.gsi.de/work/forschung/experimentelektronik/digitalelektronik/digitalelektronik/module/vme/vulom/vulom1

[25] J. Allison *et al.,* Nucl. Instr. Meth. A **186**, 835 (2016).

[26] J. Allison *et al.,* IEEE Trans. Nucl. Sci. **53**, 270 (2006).

[27] S. Agostinelli *et al.*, Nucl. Instr. Meth. A **506**, 250 (2003).

[28] L.G. Sarmiento, A Geant4 Simulation Package for the TASISpec Experimental Detector Setup, L.G. Sarmiento, private communication (2021).

[29] D. Cho, B.Sc. thesis, Lund University, Sweden (2019).

[30] J. Adamczewski-Musch *et al.,* The Go4 Analysis Framework Reference Manual v6.2 (2022).

[31] ORTEC 672 Spectroscopy Amplifier, User Manual, https://www.ortec-online.com/products/electronic-instruments/amplifiers/672

[32] ORTEC EASY-MCA 2k or 8k Channel Multichannel Analyzer, User Manual,
https://www.ortec-online.com/products/electronic-instruments/multi-channel-analyzers/basic-analog/easy-mca-2k-or-8k

[33] MAESTRO Multichannel Analyzer Emulation Software, User Manual, https://www.ortec-online.com/-/media/ametekortec/manuals/a/a65-mnl

[34] L.-L. Andersson *et al.,* Nucl. Instr. Meth. A **622**, 164 (2010).

[35] I.-Y. Lee, Nucl. Phys. **A520**, 641c (1990).

[36] D.G. Sarantites *et al.,* Nucl. Instr. Meth. A **530**, 473 (2004).

[37] C.N. Davids & J.D. Larson, Nucl. Instr. Meth. B **40-41**, 1224 (1989).

[38] D.G. Sarantites *et al.,* Nucl. Instr. Meth. A **381**, 418 (1996).

[39] C. Langer*et al.,* Phys. Rev. Lett **113**, 032502 (2014).

[40] D. Kahl *et al.,* Phys. Lett. **B797**, 134803 (2019).

[41] A. Jokinen *et al.,* Eur. Phys. J. direct A **3**, 1 (2002).

[42] E. Stiliaris *et al.,* Z. Phys. A **326**, 139 (1987).

[43] Meng Wang *et al.,* Chinese Phys. C **45**, 030003 (2021).

[44] P. Böhm, B.Sc. thesis, Lund University, Sweden (2023).

[45] L.-L. Andersson *et al.,* Phys. Rev. C **71**, 011303(R) (2005).

[46] E. Johansson, M.Sc. thesis, Lund University, Sweden (2004).

[47] D. Rudolph *et al.*, Phys. Rev. Lett. **80**, 3018 (1998).

[48] D. Farghaly, M.Sc. thesis, Lund University, Sweden (2022).

[49] K. Wimmer *et al.,* Phys. Lett. B **847**, 138249 (2023).

[50] P. Talou *et al.,* Phys. Rev. C **58**, 3280 (1998).

[51] D. Strottman *et al.,* Physica Scripta **T88**, 148 (2000).

[52] M.P. Carpenter *et al.,* Nucl. Instr. Meth. A **353**, 234 (1994).

[53] L.L. Andersson, PhD thesis, Lund University, Sweden (2008).

[54] GEBMerge and GEBSort analysis codes, ANL webpage, https://wiki.anl.gov/gsdaq/Receivers/GEBMerge/GEBsort

[55] R. Brun & F. Rademakers, Proceedings AIHENP'96 Workshop, Lausanne, (1996).

[56] R. Brun & F. Rademakers, Nucl. Instr. Meth. A **389**, 81 (1997).

[57] Aurora, Aurora Homepage, Lund University, https://www.lunarc.lu.se/systems/aurora/

[58] COSMOS, COSMOS Homepage, Lund University, https://www.lunarc.lu.se/systems/cosmos/

[59] LUNARC, LUNARC Homepage, Lund University, https://www.lunarc.lu.se/about/

[60] A. Gavron, Phys. Rev. C **21**, 230 (1980).

[61] M.B.L. Persson, B.Sc. thesis, Lund University, Sweden (2022).

[62] J.F. Ziegler *et al.,* Nucl. Instr. Meth. A **268**, 1818 (2010).

[63] E. Johansson, PhD thesis, Lund University, Sweden (2009).

[64] L.G. Sarmiento, PhD thesis, National University of Colombia, Colombia (2012).

[65] K. Zuber & B. Singh, Nucl. Data Sheets **125**, 1 (2015).

[66] L.-L. Andersson *et al.,* Eur. Phys. J. A **30**, 381 (2006).

[67] L.-L. Andersson *et al.,* Phys. Rev. C **79**, 024312 (2009).

[68] D. Rudolph *et al.,* Eur. Phys. J. A **14**, 137 (2002).

[69] S.F. Paul *et al.,* Phys. Rev. C **104**, 065803 (2021).

[70] M. Wang *et al.,* Phys. Rev. Lett. **130**, 192501 (2023).

[71] I. Ragnarsson and S.G. Nilsson, *Shapes and Shells in Nuclear Structure*, Cambridge University Press (2005).

[72] E. Browne & J.K. Tuli, Nucl. Data Sheets **114**, 1849 (2013).

[73] S.G. Kadmensky & A.A. Sonzogni, Phys. Rev. C **62**, 054601 (2000).

[74] K.S. Krane, *Introductory Nuclear Physics*, Wiley, New York (1988).

[75] M. Goeppert Mayer, Phys. Rev **78**, 16 (1950).

[76] S.G. Nilsson *et al.,* Mat. Phys. Medd. Dan Vid. Selsk **29**, no 16. (1955).

[77] C. Gustafsson *et al.,* Ark. Fys. **36**, 613 (1967).

[78] D.H. Wilkinson & F.B. Malik Am. J. Phys. **39**, 1106 (1971).

[79] J. Ekman *et al.,* Mod. Phys. Lett. A**20**, 2977 (2005).

[80] A.P. Zuker *et al.,* Phys. Rev. Lett.**89**, 142502 (2002).

[81] E. Caurier, Shell model code ANTOINE, IRES, Strasbourg 1989-2002.

[82] E. Caurier & F. Nowacki, Acta Phys. Pol. **30**, 705 (1999).

[83] S. Cohen & D. Kurath, Nucl. Phys. **73**, 1 (1965).

[84] A. Magilligan & B.A. Brown, Phys. Rev. C **101**, 064312 (2020).

[85] A. Poves *et al.,* Nucl. Phys. A **694**, 157 (2001).

[86] M. Honma *et al.,* Phys. Rev. C **65**, 061301(R) (2002).

[87] M. Honma *et al.,* Phys. Rev. C **80**, 064323 (2009).

[88] M. Horoi *et al.,* Phys. Rev. C **73**, 061305(R) (2006).

[89] B. Blank *et al.,* Nucl. Instr. Meth. A **416**, 41 (2018).

[90] S.F.D. Mc Caughley, B.Sc. thesis, Lund University, Sweden (2024).

[91] A.J. Cole, *Statistical models for nuclear decay - From evaporation to vaporization*, CRC Press, Boca Raton (2000).

[92] V. Weisskopf, Phys. Rev. **52**, 295 (1937).

[93] W. Hauser & H. Feshbach, Phys. Rev. **87**, 366 (1952).

[94] P.A. Moldauer, Phys. Rev. C **11**, 426 (1975).

[95] A.S. Iljinov *et al.,* Nucl. Phys. A **543**, 517 (1992).

[96] D. Bazin *et al.,* Nucl. Instr. Meth. A **482**, 307 (2002).

[97] O.B. Tarasov & D. Bazin, Nucl. Instr. Meth. B **266**, 4657 (2008).

[98] R. J. Charity, Phys. Rev. C **82**, 014610 (2010).

[99] A. Idini, private communication (2024).

[100] Y.Z. Wang *et al.,* Phys. Rev. C **89**, 047301 (2014).

[101] G. Pédehontaa-Hiaa *et al., Investigation of the limits of detection for specific radionuclides in soil from the European Spallation Source (ESS) using radiometric and mass spectrometric methods*, Strålsäkerhetsmyndigheten, 2023:12 (2023).

[102] GSI FAIR, GSI FAIR webpage, https://www.gsi.de/en/researchaccelerators/fair/research

[103] J.M. Gates *et al.,* Phys. Rev. Lett. **133**, in press (2024).

[104] K. Bourzac, *Heaviest element yet within reach after major breakthrough*, Nature press release, Nature (2024).

[105] E.K. Johansson *et al.,* Phys. Rev. C **77**, 064316 (2008).

[106] T. Henry, PhD thesis, University of York, United Kingdom.

[107] A. Obertelli *et al.,* Phys. Lett. **B701**, 417 (2011).

[108] P. Golubev, private communication (2024).

Scientific publications

About the author

I joined the Nuclear Structure Group at Lund University in late 2019. My research journey during these five years focused on advancements in experimental studies of exotic nuclei and rare decay modes through particle and γ-ray coincidence spectroscopy. The focus was on complementing state-of-the-art Compex Ge-detectors with anti-Compton shields and enhancing the Gammasphere setup at Argonne National Laboratory, USA, with pixelated silicon detectors. These upgrades enabled new discoveries, including a proton-emitting state in ^{61}Ga and a detailed study of deuteron evaporation from N=Z nuclei, providing valuable experimental data points for refining nuclear structure models and reaction mechanisms. This research provides the basis of my PhD thesis.

Printed by Media-Tryck, Lund 2024 NORDIC SWAN ECOLABEL 3041 0903

LUND UNIVERSITY

Faculty of Science
Department of Physics

ISBN 978-91-8104-223-8